

ABSTRACT

Title of dissertation: TIME-REVERSAL
INDOOR POSITIONING SYSTEM
AND MEDIUM ACCESS CONTROL

Zhung-Han Wu, Doctor of Philosophy, 2016

Dissertation directed by: Professor K. J. Ray Liu
Department of Electrical and Computer Engineering

With the rapid expansion of the wireless communication, there has been a rapid growth in the demand for the mobile traffic. Moreover, the wireless traffic not only expands in traffic volume but also in the diversity of applications and requirements with the rise of the Internet of Things (IoT) concept. The insatiable demand for both the traffic volume and the ever-expanding IoT applications poses a great challenge on the design of the next generation, i.e. the 5G, communication system.

Time reversal (TR) technology has been proposed as a promising candidate for the 5G system with several promising characteristics, such as easy densification, asymmetric and heterogeneous design. TR system utilizes large bandwidth and observes detailed, location-specific channel impulse responses (CIR). With the detail CIR information, the TR system designs waveforms to concentrate transmitted energy to the intended users via the unique spatial temporal focusing effect. In this dissertation, we propose a TR indoor positioning system and medium access control design based on this unique effect.

We begin by proposing the time reversal resonating strength (TRRS) to quantify the similarity between the location information embedded CIRs. The TR indoor positioning system identifies the unknown users by calculating the TRRS between the CIR of the unknown user and the CIRs in the database. We built the system prototype and are the first-ever to perform precise indoor positioning at 1 to 2 cm resolution in both line-of-sight and non-line-of-sight scenario using one pair of transmitter and receiver both equipped with a single antenna. Based on the positioning system, we propose an indoor tracking system by collecting CIRs at several regions of interest and track unknown users when they pass it. To facilitate deployment, we built a prototype to automate CIR collection and the experiments show that the system detects the users correctly with very low false alarm rate.

In the second part, we design the medium access control scheme to maximize system sum rate and guarantee quality of service to the users in a downlink scenario. The system objective and constraints are transformed into a mixed integer quadratically constraint quadratic programming and can be solved efficiently. We then investigate rate adaptation scheme via selection of optimal backoff factors in TR system. The rate adaptation scheme effectively increases the system-wise performance and the fairness among users.

TIME-REVERSAL INDOOR POSITIONING SYSTEM AND
MEDIUM ACCESS CONTROL

by

Zhung-Han Wu

Dissertation submitted to the Faculty of the Graduate School of the
University of Maryland, College Park in partial fulfillment
of the requirements for the degree of
Doctor of Philosophy
2016

Advisory Committee:
Professor K. J. Ray Liu, Chair/Advisor
Professor Min Wu
Professor Gang Qu
Dr. Zoltan Safar
Dr. Beibei Wang
Professor Lawrence C. Washington

© Copyright by
Zhung-Han Wu
2016

Dedication

To my Family —

Zhong-Sheng Wu, late Mei-Hsiu Pan

and Tsung-Mu Wu.

Acknowledgments

First and foremost, I would like to express my most esteemed gratitude to my advisor, Prof. K. J. Ray Liu for his patient guidance and continuous support during my Ph.D. study. His steadfast and relentless pursuit of excellence on both research and experiment leads me to innovative research that contributes to the advance of wireless communications. I appreciate his impact on my motivation and attitude toward work and life, and his guidance on my professional and personal development. I will always remember his advice — be confident — which is the most important thing I learned. I will bear this in mind and keep practicing it for the years to come.

I would also like to thank all members in my dissertation committee. I am especially grateful to Dr. Beibei Wang for the guidance on my research and comments on the writing, and thankful to Dr. Zoltan Safar for the enlightening discussions on research and for generously sharing with me his invaluable industry experience. I am also thankful to Prof. Min Wu for her guidance on recitation during my teaching assistant work. I also thank Prof. Gang Qu and Prof. Lawrence Washington for their time and efforts serving on my dissertation committee and reviewing my thesis.

I would like to thank all members of Signal and Information Group for their pleasant friendship, continual assistance, and thoughtful discussions. Thanks to Yan Chen and Beibei Wang for guidance on research; Matthew Stamm for his guidance on presentation; Hung-Quoc Lai for guidance on project implementation

and management; Yu-Han Yang, Xiaoyu Chu, Chunxiao Jiang, Yi Han, Hang Ma, Qinyi Xu, Chen Chen, and Feng Zhang for their support and discussion. I thank all of them for their unreserved giving that has affected and shaped me in some way or another.

I thank all my friends for being there, either by my side or across the screen. I am so thankful for their tender catch during the downfalls and their shared joy during the great times. Thanks to Prof. Ping-Cheng Yeh for encouraging me to study abroad. Special thanks to the Hsiung family for their hospitality and care during the last few years. Their unrequited support anchors me during this journey.

Most importantly, I would like to give my deepest appreciation to my parents, Zhong-Sheng Wu and Mei-Shiu Pan, and brother, Tsung-Mu Wu. I would not have been able to reach this important achievement in my graduate study without their endless love and emotional support and I would like to share this joy with them. This dissertation is dedicated to them.

Table of Contents

List of Tables	vii
List of Figures	viii
1 Introduction	1
1.1 Motivation	1
1.2 Dissertation Outline and Contributions	4
1.2.1 Time Reversal Indoor Positioning System (Chapter 2)	5
1.2.2 Virtual Checkpoint based Indoor Tracking System (Chapter 3)	6
1.2.3 Time Reversal Medium Access Control (Chapter 4)	7
1.2.4 Time Reversal Rate Adaptation (Chapter 5)	7
2 Time-Reversal Indoor Positioning System	9
2.1 Time Reversal Indoor Positioning System	13
2.1.1 Background of Time Reversal	14
2.1.2 The Proposed Time Reversal Indoor Positioning Algorithm . .	17
2.1.2.1 Offline Training Phase	17
2.1.2.2 Online Positioning Phase	19
2.2 Experiments	25
2.2.1 Experiment Setting	25
2.2.2 Evaluation of TR Properties	25
2.2.2.1 Channel Reciprocity	26
2.2.2.2 Channel Stationarity	26
2.2.2.3 Spatial Focusing	27
2.2.3 Localization Performance	29
2.2.4 Discussions	32
2.3 Summary	34
3 Virtual Checkpoint based Indoor Tracking System	35
3.1 Virtual Checkpoints	36
3.2 Virtual Checkpoint Construction	38
3.3 System Implementation	42
3.4 System Operation	43
3.5 Experiment	44
3.6 Discussion	47
3.7 Summary	49
4 Time Reversal Medium Access Control	50
4.1 System Overview	54
4.1.1 Time Reversal Division Multiple Access System	54
4.1.2 Massive MIMO system	55
4.2 Spatial Focusing Effect	56
4.3 Downlink User Selection Algorithm	59

4.3.1	TRDMA System Overview	60
4.3.2	Normalized Interference Matrix Calculation	61
4.3.3	Scheduler Objective	62
4.3.4	Mixed Integer Optimization	63
4.3.5	Positive Semidefiniteness of \mathbf{Q} and \mathbf{Q}_i	67
4.3.6	Extension to Multi-Cell Scenarios	68
4.4	Impact of Imperfect Channel Information	71
4.4.1	Golay Sequence Based Channel Estimation	72
4.4.2	Channel Estimation via Golay Sequence	73
4.4.3	Channel Estimation Error Analysis	75
4.4.4	SNR Enhancement of Golay Sequence Based Channel Estimation	75
4.4.5	Effect on the Scheduler Parameter	77
4.5	Simulation Results	79
4.5.1	Time Complexity	80
4.5.2	Scheduling Performance Comparison	80
4.5.3	Channel Estimation Error	85
4.6	Summary	88
5	Time Reversal Rate Adaptation	89
5.1	System Overview	92
5.2	Spatial Temporal Focusing Effect	94
5.2.1	Temporal Impact of Backoff Factor on Interference	99
5.2.2	Spatial Impact of Backoff Factor on Interference	100
5.3	Weighted Rate Maximization	101
5.4	Waveform Design with SINR Constraints	107
5.4.1	Uplink Downlink Duality	109
5.4.2	Power Allocation with SINR Constraint	110
5.5	Simulation Results	113
5.6	Summary	120
6	Conclusions and Future Work	122
6.1	Conclusions	122
6.2	Future Work	125
	Bibliography	127

List of Tables

2.1	Localization performance with 10-cm localization accuracy	32
4.1	Maximum absolute value of the off-diagonal components of the estimated channel estimation error correlation with different L_G	86

List of Figures

2.1	System model	13
2.2	The time reversal signal processing principle	14
2.3	Radio stations of the proposed TR system prototype.	18
2.4	(a) Floor plan of the office room that we conduct our experiments; (b) Floor plan of room A.	21
2.5	Evaluation of channel reciprocity: (a) CIR of the forward link; (b) CIR of the backward link.	22
2.6	Cross correlation between the CIR of forward link and that of the backward link. Note that the center tap is the TR resonating strength between the CIR of forward link and that of the backward link. . . .	22
2.7	TR resonating strength between CIRs of the forward link and those of the backward link.	23
2.8	Evaluation of short temporal stationarity using the TR resonating strength between any two CIRs from the 30 CIRs of the link between the TD to the AP.	23
2.9	Evaluation of long temporal stationarity using the TR resonating strength between any two CIRs from the 18 CIRs collected over a weekend between the AP and TD.	24
2.10	Evaluation of channel stationarity under minor environment change using TR resonating strength between any two CIRs collected with a person walking around.	24
2.11	Three-dimensional architecture for moving the locations of the TD. . .	28
2.12	γ of all grid points by moving the intended location within 1 m by 0.9 m area. Every dot in the figure stands for one grid point where two neighboring grids points are 10cm away from each other. The horizontal/vertical axis is the location index with 1-D representation. Each value in (i, j) represents the focusing gain at location j (location index with 1-D representation) when the intended location is i (location index with 1-D representation).	30
2.13	Geographic distribution of γ with the intended location at the center of the area of interest.	31
2.14	Fine-scale geographic distribution of γ	31
3.1	Mapping machine system.	40
3.2	Prototype of the VC measuring machine.	41
3.3	Screenshot of the VC collecting GUI.	41
3.4	Floor map showing the location of the Origin and the VC.	45
3.5	γ when hitting a VC.	46
3.6	CDF of the maximum of γ between the CIR of the unknown users and the CIRs in the VC database.	46
3.7	ROC of VC detection.	47
4.1	System diagram of a TRDMA system.	55

4.2	Demonstration of the spatial focusing effect for both TR and massive MIMO systems with different DoF.	58
4.3	An example of Golay sequence.	72
4.4	Diagram for Golay based channel estimation.	73
4.5	An example of $\Phi\Phi^H$	76
4.6	Run time comparison for different number of users.	80
4.7	Performance of the proposed scheduler compared with exhaustive search result.	82
4.8	Performance of the proposed scheduler with different physical layer implementations.	83
4.9	Performance of proposed scheduler compared with a first-come-first-serve system.	84
4.10	Performance comparison between the proposed scheduler and the pair-wise SUS scheduler.	85
4.11	Performance ratio ρ_E between perfect channel R_S and channel estimation error R_E	87
5.1	Energy distribution of TR system within the area of interest and across time. The figures are listed from the left to right first, and then top to bottom. The middle one the time instant with maximum energy focusing, which is $m = 30$. The energy are normalized such that the maximum energy received is 0dB.	97
5.2	Spatial focusing effect with $D = 4$ on the left and $D = 8$ on the right for user 1.	100
5.3	SIR of two users with $D_1 = [4, 6, 8, 10, 12]$	101
5.4	Throughput comparison with the proposed algorithm and fixed D^1 , $M = 2$, $k = 4$	115
5.5	Performance, $\rho = R_{MIQCQP}/R_{fixed}$, comparison with different k , $M = 2$	116
5.6	Fairness index $J(\mathbf{x})$ comparison between the proposed algorithm and fixed D , $k = 2$, $M = 2$	117
5.7	Performance comparison with different k with waveform design, $M = 2$	117
5.8	Fairness index $J(\mathbf{x})$ comparison between the proposed algorithm and fixed D with waveform design, $k = 2$, $M = 2$	118
5.9	Performance comparison of rate adaptation combined with and without waveform design, $M = 2$	119
5.10	Performance comparison between fixed D^1 and rate adaptation with waveform design, $M = 2$	120

Chapter 1

Introduction

1.1 Motivation

There has been a rapid increase in demand for mobile communications due to the proliferation of the versatile applications on all kinds of mobile devices in everyday life, such as streaming video when commuting, navigation while driving, etc. The ever-growing number of devices and applications requires a much larger transmission rate for fast and mobile data delivery in order to provide users with satisfactory experience. Based on a mobile data traffic forecast [1], the mobile traffic volume is expected to increase more than 8 folds by the year 2020, where most of the traffics are generated indoors. The sharp increase in the demand for the data rates poses great challenges in the design for the next generation, i.e. the 5G, communication system.

Moreover, the mobile data demand not only increases in shear volume, but also increases in the diversity of the sources that generate data. The reduced cost of hardware manufacturing and the development of new applications make universal wireless connectivity possible, and foster the Internet of Things (IoT) trend. Not only the aforementioned mobile devices are connected to the internet, but also all the

everyday appliances are connected seamlessly in the IoT era. In recent years, the IoT application has expanded from mere sensor applications to a complex ecosystem that has covered areas such as healthcare, utility, marketing, etc. Since IoT is expected to alter several aspects of everyday life and the behavior of users, organizations such as Industrial Internet Consortium, OpenFog Consortium, and IoT Acceleration Consortium, are set up to foster development, standardization and manufacturing process in both academia and industry fields.

The Time Reversal system is proposed as a promising indoor solution for the 5G communication system that addresses the aforementioned challenges in the 5G system by using a large transmission bandwidth. The TR system has been shown to possess features, such as the easy network densification, asymmetric transceiver design, and heterogeneity in bandwidth usage, which are suitable for the 5G communications and the IoT implementation. By using a large bandwidth, the TR system records detail channel impulse response (CIR) information with much more channel taps than that of a narrowband system, where only one or two channels taps are recorded. Because the observed CIR is the superposition of the reflected copies of the transmitted signal from the surrounding environment, the CIR naturally embeds information about the environment. Experiments show that the difference in the location-specific CIRs is able to distinguish two adjacent locations with only 5 cm separation, even under the non-line-of-sight setting. TR therefore utilizes the environment information embedded in the CIR to design transmission waveforms such that the environment acts as a spatial filter and the transmitted signal adds up coherently only at the intended users, which is the unique spatial temporal fo-

cusing effect in the TR system. The unique spatial temporal focusing effect of the TR system makes possible the exploration of opportunities and the development of different applications.

The CIR information can be extracted from mobile traffic packets, and therefore the location information is implicitly contained within every activity over the wireless channel. Statistics show that people spend most of the time indoor, generating most of the mobile data traffic, which makes CIRs the perfect medium for precise indoor localization. The precise localization of human via CIR has numerous applications and business opportunities, such as navigation and target marketing. Moreover, the location information extracted from CIR can assist IoT applications to incorporate mobility and navigation functions and foster applications such as the household robots. With all the opportunities and applications, the ability to use CIRs for localization is an desirable feature for the 5G communication system.

Diverse applications scenarios are expected in the IoT era, and there is a large disparity in the required quality of service (QoS) between different applications. The surveillance camera consumes much larger transmission rate for streaming compared with the simple on and off operation of the wireless switch. Satisfying the different required QoS of the diverse applications is important for the seamless IoT application integration with everyday life. Therefore, the ability to support and satisfy the different QoS requirements is highly desirable for the TR system as a proposed 5G communication solution.

The increase in the number of users of the 5G communication system and the IoT application poses great challenges in interference management and resource al-

location. The massive number of taps in CIR enables the TR system to design waveforms and harvest the unique spatial temporal focusing effect which concentrates the transmitted energy to only the intended users and reduces the interference to the unintended ones. However, with the increase of users, the interference increases, and the system is not able to maintain the QoS of the users and to maximize the system performance. To serve the massive number of users in the foreseen future, it is important for the TR system to make judicious decisions on deciding which users to transmit together.

On the other hand, resource allocation is another effective way to increase the system performance by properly distributing system resources, such as the power and resource blocks in time and frequency, among users. However, most allocation schemes concentrate on the system-wise performance but fail to consider the different transmission requirements of the users. As a result, the existing allocation cannot guarantee a minimal performance for users and fails to provide a satisfying user experience. Therefore, a novel resource allocation scheme is highly desirable to jointly consider both the system-wise performance as well as the users' requirement of the service.

1.2 Dissertation Outline and Contributions

From the previous discussions, we can see that the TR technique is a promising candidate for both 5G communications and IoT applications. However, there are many new challenges and problems to be solved to achieve a successful system

design. In this dissertation, we focus on the indoor positioning system and the medium access control for the TR technology. The first part of this dissertation focuses on the implementation and the application of the TR indoor positioning system using the location-specific CIR information. In the second part, we develop time reversal medium access control schemes to accommodate a massive number of users and to satisfy the QoS of the users in the scenario where a massive number of users present. The rest of this dissertation is organized as follows.

1.2.1 Time Reversal Indoor Positioning System (Chapter 2)

In this chapter, we show that by using a large bandwidth, the TR system records detailed location-specific CIRs and is able to distinguish two locations that are only 10 cm apart under non-line-of-sight setting with only one antenna on both the transmitter and receiver. The CIR embeds the information of the environment and the TR system can faithfully record this information for precise indoor positioning. We propose the time reversal resonating strength, TRRS, to quantify the closeness of two CIRs and use the proposed TRRS to estimate the user's precise location. By constructing a database of CIRs at the locations of interest, we can estimate the position of the unknown user by finding the location with the closest CIR with the CIR of the user.

We perform experiments to first show the important characteristics of the CIR, including the channel reciprocity and the stationarity. We then evaluate the performance of the proposed two-phase indoor positioning system by locating an

unknown user in a 1 m by 0.9 m area. Experiment results show that the proposed TR indoor positioning system is the first-ever system to achieve 1 to 2 cm accuracy under both line-of-sight and non-line-of-sight environment with only one pair of transmitter and receiver both equipped with a single antenna.

1.2.2 Virtual Checkpoint based Indoor Tracking System (Chapter 3)

Based on the experiment result in Chapter 2, we propose a Virtual Checkpoint (VC) based TRacking system (VCTR system) for indoor tracking. By collecting CIRs within a region of interest as the CIR database, and when the user passes through the region, it is very likely that the user will pass the location where the CIR is collected. Therefore, a higher TRRS value between the CIR from the user and the database indicates that the user passes through the region. We call the region of interest as VC, as it resembles the actual checkpoint deployed in all kinds of public spaces. In order to automate the CIR collection and foster the deployment of the CTR system, we construct a CIR collecting machine prototype for massive collection with user-friendly GUI. We perform experiments in an ordinary office setting to show several performance metrics to evaluate the performance of the proposed VCTR system. Experiments show that there is a significant gap in the CDF of the TRRS values between the cases when the user passes the VC or not. The ROC curve based on the CDF shows that the proposed VCTR system can perform perfect detection with very low false alarm rate.

1.2.3 Time Reversal Medium Access Control (Chapter 4)

One of the major challenges in the design of the 5G system is to accommodate the ever-increasing number of users. With the growing number of users, the 5G system needs to judiciously manage the interference between users to satisfy the QoS of the users. In this chapter, we propose a novel scheduler for the 5G system that maximizes the system performance while satisfies users' QoS requirements. The optimization objective and constraints are transformed into a mixed integer quadratically constraint quadratic programming (MIQCQP) which has linear time complexity that is suitable for a massive number of users.

To evaluate the robustness of the proposed scheduler, we investigate the channel estimation error of the TR system. The analysis reveals that the TR system has the same channel estimation error distribution as that of the massive MIMO system. Based on the simulation result, we show that the proposed scheduler is suitable for the 5G communications system with linear time complexity, versatile application and resilient to channel estimation error.

1.2.4 Time Reversal Rate Adaptation (Chapter 5)

The spatial temporal focusing effect unique to TR system concentrates the transmitted energy to the intended users. However, there is energy leakage to the unintended users and causes interference. In this chapter, we propose a novel rate adaptation algorithm that manages the mutual interference through allocating the backoff factors of the users in the TR system. The backoff factor essentially de-

termines the transmission intervals between consecutive transmission among users. The optimization objective and constraints are again transformed into an MIQCQP proposed, and the optimization can be solved efficiently.

Based on the adaptation algorithm output, we propose a waveform design algorithm that maximizes the system weighted sum rate and satisfies the QoS requirements. The waveform design algorithm further reduces the mutual interference by redesigning the waveform using the adapted rates. Simulation results show that the proposed rate adaptation algorithm is suitable to different physical layer settings, and doubles the system weighted sum rate when combined with the waveform design algorithm.

Chapter 2

Time-Reversal Indoor Positioning System

From the previous discussion, it is clear that the indoor location information is useful and crucial for different IoT applications. In the literature, many indoor positioning systems (IPS) approaches have been developed, and most of them can be classified into three categories [34]: triangulation, proximity methods, and scene analysis. In triangulation, the terminal device (TD) measures the time of arrival (TOA) [62], time difference of arrival (TDOA) [16], angle of arrival (AOA) [43], [56] of the signals sent from the access point (AP) with known positions and then uses physical principles of wave propagation to calculate the geographical location based on the measurements. Although the concept of triangulation is simple, some special requirements are needed, e.g., precise measurements of TOA and/or AOA, synchronization between the TD and the AP, and specialized apparatus for AP. However, due to the rich scattering characteristic of the indoor environment, the measurements are generally not very precise, which leads to poor indoor positioning performance of these triangulation methods.

The second category of IPS algorithms is a proximity method that can provide symbolic relative location information. This kind of algorithms relies on the dense deployment of the infrastructure. When the TD moves in the target area, the TD is

considered to be located with the antenna that detects the TD. If multiple antennas can detect the TD, then the TD is simply considered to be located with the antenna that receives the strongest signal. Most of the radio-frequency (RF) identification and the cell identification [66] positioning systems fall into this category. Since the TD will be considered to be colocated with the antenna, this kind of algorithms cannot give precise location information. Moreover, due to the dense deployment of the antennas, the implementation cost is very high.

The third category of IPS algorithms is the scene analysis method, which first collects features of the scene and then matches online measurements with the collected features to estimate the location. Most of the scene analysis-based IPS algorithms make use of the received signal strength (RSS) and/or the channel state information (CSI), while the matching method can be either deterministic or probabilistic [48]. In a deterministic method, the position is determined by finding the minimum distance between the measurements to the database. In [27], it was proposed to first use spatial filtering to reduce the number of reference APs and then use kernel functions as distance measures. A root-mean-square error of 2.71 m was reported using three APs. An RF-based tracking system named RADAR was proposed in [2]. The system uses empirically determined and theoretically computed signal strength for triangulation, and triangulation is done using the signal strength information gathered at multiple locations. A median resolution was reported to be in the range of 23 m using three APs. A linear approximation model on the RSS versus the Euclidean distance between the AP and the TD in an anonymous environment without necessary offline training was proposed in [26] and achieves a

mean estimation error of 15m. A compressive sensing scheme was proposed in [13] for localization using the sparsity characteristics in positioning problems with 1.5-m error.

On the other hand, in a probabilistic method, the estimation is based on some probabilistic criteria such as maximum a posteriori (MAP) and maximal likelihood (ML). In [60] and [61], a positioning algorithm based on WiFi RSS was proposed. The RSS information from multiple WiFi APs is collected, and the distribution of the RSS is estimated. During the online positioning phase, the MAP or ML criterion is used to determine the location and achieve a mean error of 40 cm with multiple APs. In [6], the RSS of WiFi and FM signals was used to jointly estimate the cumulative distribution function of RSS for indoor positioning. The smaller variation of FM signals in an indoor environment provides extra information and precision over WiFi-only systems and achieves better roomlevel accuracy. In addition to the RSS, the CSI has been also used in the literature for positioning. In [25], it was proposed to use the amplitude of channel impulse response (CIR) as the fingerprint for localization. The amplitude of CIR is used as an input to a nonparametric kernel regression method for location estimation. In [44] and [64], it was proposed to utilize the complex CIR as a link signature for location distinction, where the normalized minimal Euclidean distance is adopted as the distance measure. The CSI was proposed to be used in the orthogonal frequency-division multiplexing (OFDM) systems as the fingerprints in the positioning algorithm [54]. Since there are a lot of partitioned channels in an OFDM system, the CSI provides rich information for positioning. In the online phase, the CSI from the TD is matched to the stored database using a MAP

algorithm. The authors report a mean accuracy value of 65 cm in a 5 m by 8 m office using three APs.

However, most of the existing IPS algorithms cannot achieve a desired centimeter-level localization accuracy value, particularly for a single AP working in the non-line-of-sight (NLOS) condition. The main reason is that it is generally very difficult or even impossible to obtain precise measurements due to the rich scattering indoor environment. Such imprecise measures lead to ambiguity when performing positioning algorithms. To reduce ambiguity, most existing algorithms require more online measurements and/or multiple APs. Different from the existing approaches, in this chapter, we propose a single-AP indoor positioning algorithm that can achieve centimeter-level localization accuracy with single realization of online measurement by utilizing the time-reversal (TR) technique. TR technique is known to be able to focus the energy of the transmitted signal only onto the intended location, i.e., the spatial focusing effect. The foundation of spatial focusing is that the CIR in a rich scattering indoor environment is location specific and unique for each location [50], i.e., each CIR corresponds to a physical geographical location. Therefore, by utilizing such a unique location-specific CIR, the proposed TR indoor positioning system (TRIPS) is able to position the TD by matching the CIR with the geographical location. Since spatial focusing is a half-wavelength focus spot, the proposed TRIPS can achieve a centimeter-level localization accuracy value even with a single AP working in the NLOS condition.

The rest of the chapter is organized as follows. In section II, we will briefly review the TR technique and describe in details the proposed TRIPS. Then, in sec-

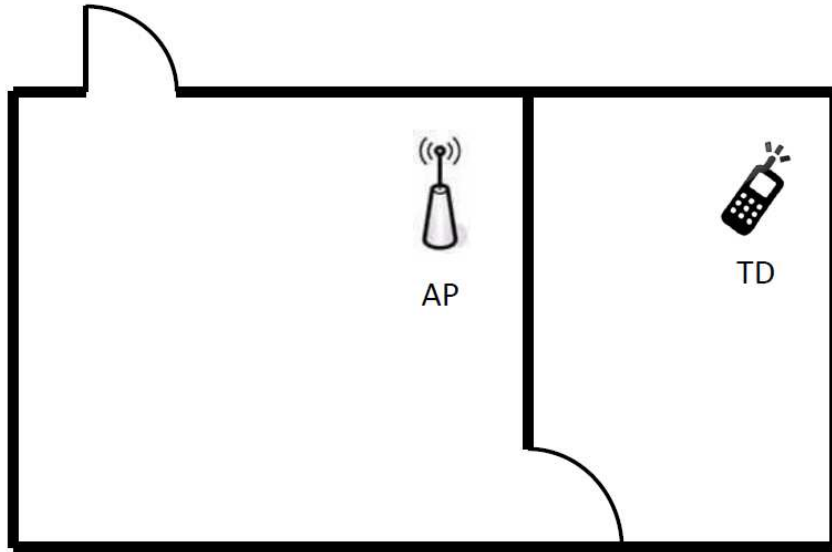


Figure 2.1: System model

tion III, we will discuss the experimental results including the properties of the TR technique and the performance of the proposed TRIPS. Finally, we draw conclusions in section IV.

2.1 Time Reversal Indoor Positioning System

As shown in Fig. 2.1, we study the indoor localization problem where there is an AP and a TD in an indoor environment. The AP is positioned in an arbitrarily known location, whereas the location of the TD is unknown. The TD transmits some known signals, e.g., fixed pseudorandom sequences, to the AP, and the AP tries to estimate the location of the TD based on the received signals. Due to the multipaths in the indoor environment, the received signal at the AP is significantly distorted [60]. In such a case, it is generally impossible to identify the location purely

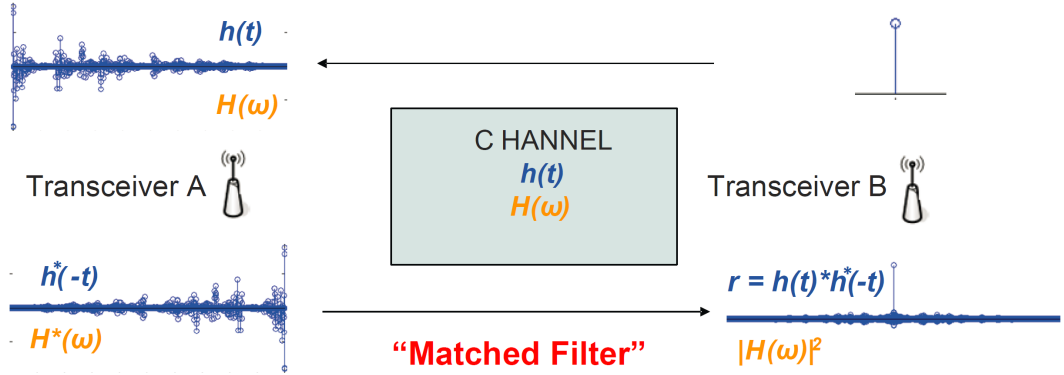


Figure 2.2: The time reversal signal processing principle

based on the received signal of a single AP, i.e., the single-AP indoor localization problem is ill posed.

To address this problem, we propose a TRIPS by decomposing the ill-posed problem into two well-defined subproblems. Specifically, in the first subproblem, we build a database offline by mapping the physical geographical locations to the logical locations in the CIR space. Then, in the second subproblem, we match the online estimated CIR of the TD to those in the database to position the TD. In the following sections, we first give a brief introduction of the TR technique and then discuss in detail the proposed TR-based indoor positioning system.

2.1.1 Background of Time Reversal

TR is a technology that can focus the power of the transmitted signal in both time and space domains. The phenomenon of TR was first observed by Zeldovich et al. in 1985 [63]. Later, the TR technique was studied and applied into signal

processing by Fink et al. in 1989 [15], followed by several theoretical and experimental works in acoustic and ultrasonic communications, verifying that the transmitted wave energy can be focused at the intended location with high spatial and temporal resolution [10,12,14]. Due to the fact that TR does not require complicated channel processing and equalization, it was also analyzed, tested, and validated in wireless communications [50], [5, 9, 19–21, 31–33, 38, 47, 58]. Moreover, with a potential of over an order of magnitude of reduction in power consumption and interference alleviation, as well as the natural capability of supporting heterogeneous TDs and providing an additional security and privacy guarantee, TR technique is shown to be a promising solution for green Internet of Things [4].

Fig. 2.2 demonstrates a simple TR communication system [50]. When transceiver A wants to transmit information to transceiver B, transceiver B first sends an impulse signal to transceiver A. This is called the channel probing phase. Then, transceiver A time-reverses (and conjugates if the signal is complex) the received waveform from transceiver B and uses the time-reversed version of waveform to transmit the information back to transceiver B. This second phase is called the TR transmission phase.

The TR technique relies on two basic assumptions, i.e., channel reciprocity and channel stationarity. Channel reciprocity requires the CIRs of the forward and backward links to be highly correlated, whereas channel stationarity requires the CIR to be stationary for at least one probing-and-transmission phase. These two assumptions generally hold in practice, as validated by experiments in [47] and [50]. In [47], an experiment was conducted in a laboratory area and showed

that the correlation of CIR between the forward and backward links is as high as 0.98, whereas in [50], it was shown that the multipath channel in a typical office environment does not vary much over time. Specifically, the CIR had a snapshot once every minute for a total of 40 min, where the first 20 snapshots correspond to a stationary environment, the 21st to 30th snapshots correspond to a moderately varying environment, and the last 10 snapshots correspond to a varying environment. The experimental results show that the correlation coefficients between different snapshots are above 0.95 for a stationary environment and above 0.8 for a varying environment.

With the property of the channel reciprocity and stationarity, the re-emitted TR signal will retrace the incoming paths and form a constructive sum of signals at the intended location, resulting in a peak in the signalpower distribution over the space, i.e., spatial focusing effect. Since TR utilizes all the multipaths as a matched filter, the transmitted signal will be focused in the time domain, which is referred as the temporal focusing effect. Moreover, by using the environment as matched filters, the transceiver design complexity can be significantly reduced. In an indoor environment, the wireless multipaths come from the surrounding reflectors. Since the received waveforms from the TD at different locations undergo different reflecting paths and delays, the multipath profile is unique for each location. By utilizing this unique location-specific multipath profile, TR can create the spatial focusing effect at the intended location, i.e., the received signals are added coherently at the intended location but incoherently at any unintended location. As will be discussed in the next section, our proposed algorithm leverages such a special feature

to solve the ill-posed single-AP indoor localization problem.

2.1.2 The Proposed Time Reversal Indoor Positioning Algorithm

Here, we will discuss in detail the proposed TR indoor positioning algorithm. With the spatial focusing effect, we know that the CIR in the TR system is location specific, which means that we can map the physical geographical locations into logical locations in the CIR space where one physical geographical location corresponds to a unique CIR in the TR system. Then, the indoor localization problem becomes a classical classification problem that identifies the class of the TD in the CIR space. Therefore, the proposed TR indoor positioning algorithm contains two phases. The first phase is an offline training phase where we build a CIR database to map the physical geographical location into the logical location in the CIR space, and the second phase is an online positioning phase where we match the estimated CIR of the TD with the CIR database to localize the TD.

2.1.2.1 Offline Training Phase

In the offline training phase, we are building a CIR database for the online positioning phase. Since the database has a direct consequence to the localization performance, how to build the database is critical to the proposed indoor positioning algorithm. Note that the CIR at different locations will be different if the distance between two locations is larger than the wavelength and may be similar if the distance is smaller than the wavelength. Moreover, the CIR at a certain location may



Figure 2.3: Radio stations of the proposed TR system prototype.

slightly vary over time due to the change of environment. With such an intuition, for each intended location, we obtain a series of CIRs at different time. Specifically, for each intended location p_i , we collect the CIRs information \mathbf{H}_i as follows:

$$\mathbf{H}_i = \{\mathbf{h}_i(t = t_0), \mathbf{h}_i(t = t_1), \dots, \mathbf{h}_i(t = t_M)\}, \quad (2.1)$$

where $\mathbf{h}_i(t = t_l)$ stands for the estimated CIR information of location p_i at time t_l .

Therefore, the database \mathbf{D} is the collection of all \mathbf{H}_i 's

$$\mathbf{D} = \{\mathbf{H}_i, \forall i\}, \quad (2.2)$$

2.1.2.2 Online Positioning Phase

In the online positioning phase, we first estimate the CIR information based on the signal received at the AP. Then, our objective is to localize the TD by matching the estimated CIR information with the database using a classification technique. Since the dimension of the information for each location in the database is very high, classification based on the raw CIR information may not work. Therefore, it is necessary to preprocess the CIR information to obtain important features for the classification.

As we have previously discussed, since the received signals undergo different reflecting paths and delays for the receiver at different locations, the CIR can be viewed as a unique location-specific signature. When convolving the time-reversed CIR with the CIR in the database, only that at the intended location will produce a peak, which is known as spatial focusing effect. For the locations other than the intended location, there is no focusing effect. Therefore, we can design a TR-based dimension reduction approach to extract the effective feature for localization. To do so, we first introduce a definition of *TR resonating strength* as follows.

Definition 1 (*Time Reversal Resonating Strength*): The TR resonating strength $\gamma(\mathbf{h}_1, \mathbf{h}_2)$, between two CIRs $\mathbf{h}_1 = [h_1[0], h_1[1], \dots, h_1[L-1]]$ and $\mathbf{h}_2 = [h_2[0], h_2[1], \dots, h_2[L-1]]$ is defined as

$$\gamma(\mathbf{h}_1, \mathbf{h}_2) = \frac{\max_i |(\mathbf{h}_1 * \mathbf{g}_2)[i]|^2}{\left(\sum_{i=0}^{L-1} |h_1[i]|^2\right) \left(\sum_{j=0}^{L-1} |g_2[j]|^2\right)}, \quad (2.3)$$

where $\mathbf{g}_2 = [g_2[0], g_2[1], \dots, g_2[L-1]]$ is defined as the time reversed and conjugated

version of \mathbf{h}_2 as follows

$$g_2[k] = h_2^*[L - 1 - k], k = 0, 1, \dots, L - 1. \quad (2.4)$$

A close look at (2.3) would reveal that the TR resonating strength is the maximal amplitude of the entries of the cross correlation between two complex CIRs, which is different from the conventional correlation coefficient between two complex CIRs where there is no max operation and the index $[i]$ in (2.3) is replaced with index $[L - 1]$. The main reason for using the TR resonating strength instead of the conventional correlation coefficient is to increase the robustness for the tolerance of channel estimation error. Note that most of the channel estimation schemes may not be able to perfectly estimate the CIR due to the synchronization error, i.e., a few taps may be added or dropped during the channel estimation process. In such a case, the conventional correlation coefficient without max operation may not reflect the true similarity between two CIRs, whereas our proposed TR resonating strength is able to capture the real similarity and, thus, increase the robustness.

With the definition of TR resonating strength, we are now ready to describe the online positioning phase. Let $\hat{\mathbf{h}}$ be the CIR that we estimate for the TD with unknown location. To match $\hat{\mathbf{h}}$ with the logical locations in the database, we first extract the feature using the TR resonating strength for each location. Specifically, for each location p_i , we compute the maximal TR resonating strength γ_i as follows:

$$\gamma_i = \max_{\mathbf{h}_i(t=t_j) \in \mathbf{H}_i} \gamma(\hat{\mathbf{h}}, \mathbf{h}_i(t = t_j)). \quad (2.5)$$

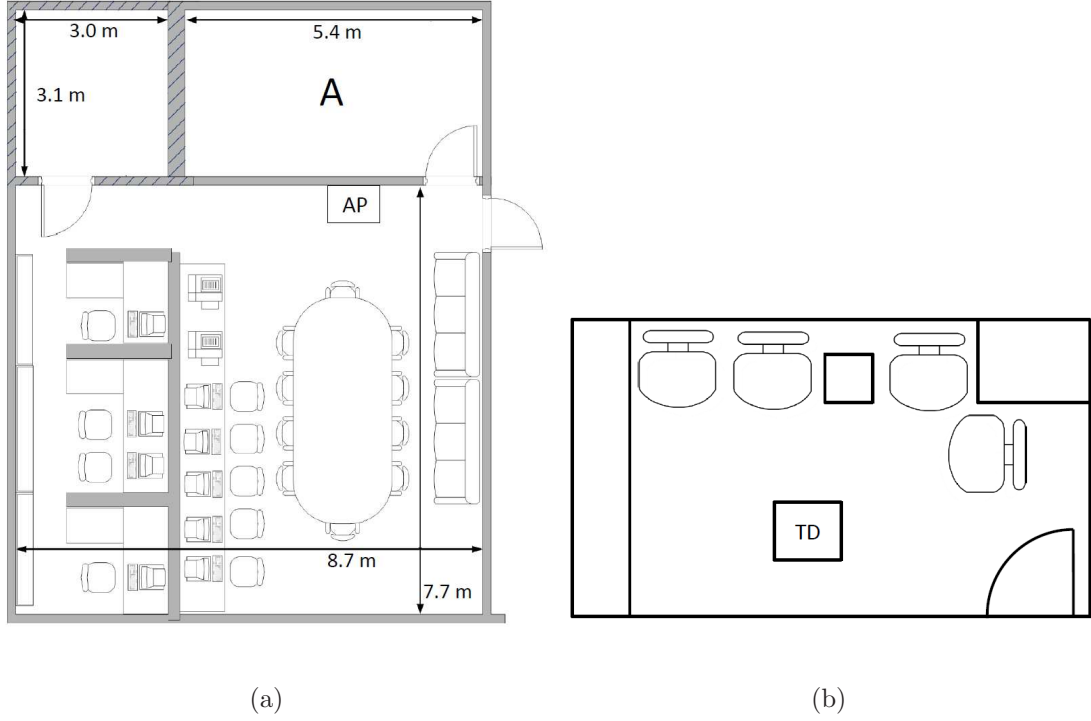


Figure 2.4: (a) Floor plan of the office room that we conduct our experiments; (b) Floor plan of room A.

By computing γ_i for all possible locations, i.e., $\mathbf{H}_i \in \mathbf{D}$, we can obtain $\gamma_1, \gamma_2, \dots, \gamma_N$. Then, the estimated location, p_i , is simply the one that can give the maximal γ_i , i.e., \hat{i} can be derived as follows

$$\hat{i} = \arg \max_i \gamma_i. \quad (2.6)$$

Although our proposed algorithm is very simple, it can achieve very good localization performance, as we will see in the experiment in the next section.

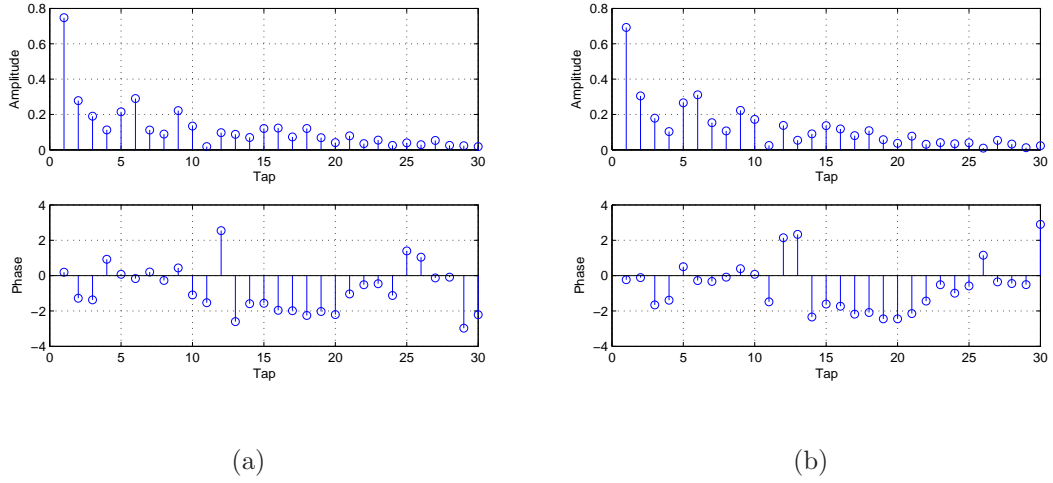


Figure 2.5: Evaluation of channel reciprocity: (a) CIR of the forward link; (b) CIR of the backward link.

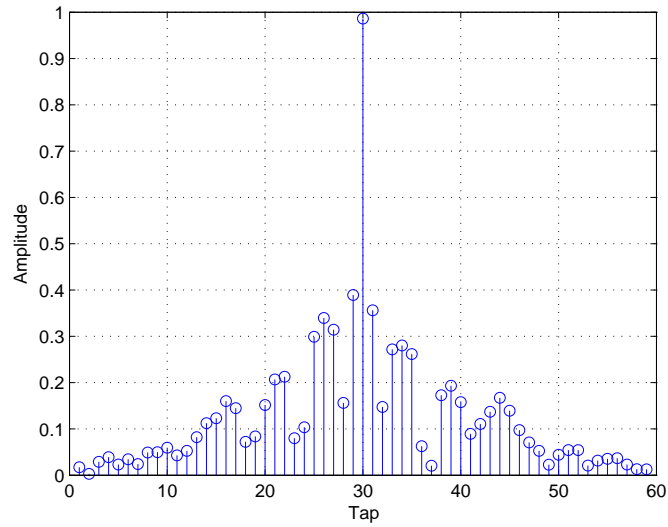


Figure 2.6: Cross correlation between the CIR of forward link and that of the backward link. Note that the center tap is the TR resonating strength between the CIR of forward link and that of the backward link.

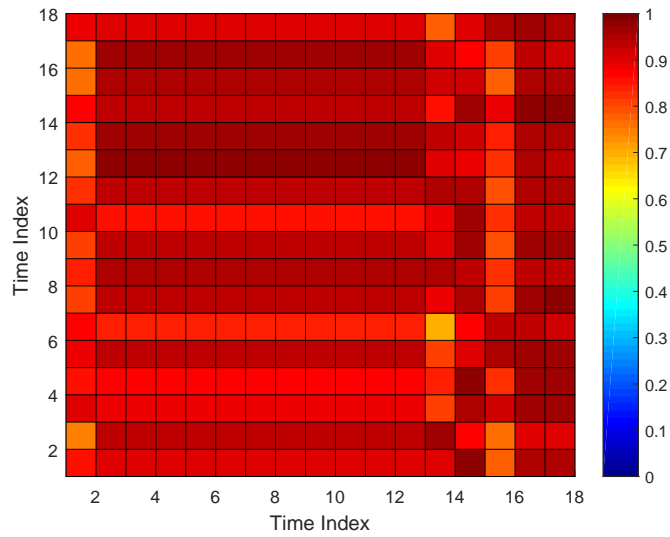


Figure 2.7: TR resonating strength between CIRs of the forward link and those of the backward link.

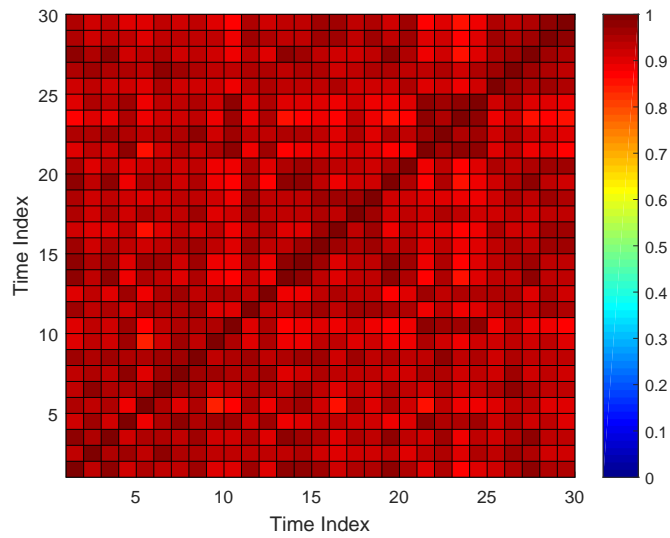


Figure 2.8: Evaluation of short temporal stationarity using the TR resonating strength between any two CIRs from the 30 CIRs of the link between the TD to the AP.

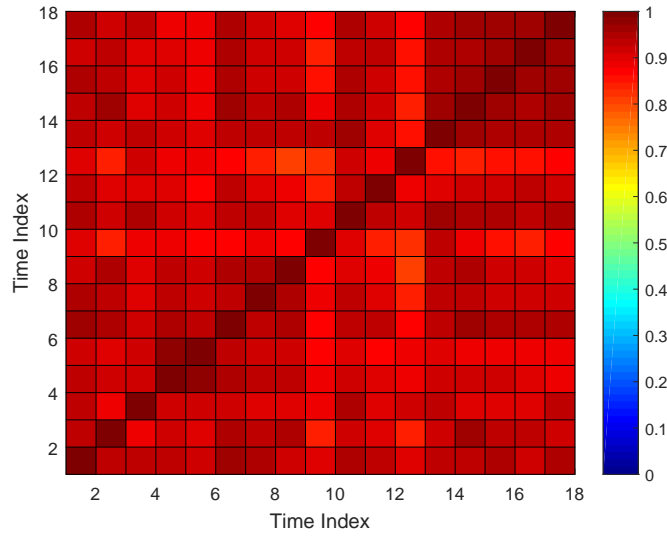


Figure 2.9: Evaluation of long temporal stationarity using the TR resonating strength between any two CIRs from the 18 CIRs collected over a weekend between the AP and TD.

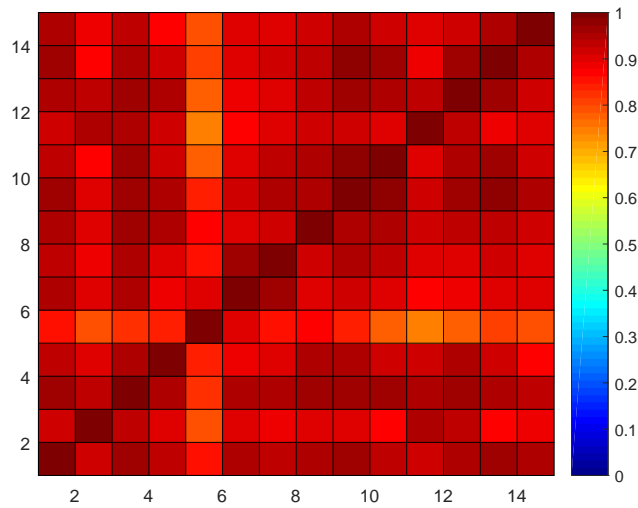


Figure 2.10: Evaluation of channel stationarity under minor environment change using TR resonating strength between any two CIRs collected with a person walking around.

2.2 Experiments

2.2.1 Experiment Setting

To evaluate the performance of our proposed algorithm, we build a TR system prototype that operates at 5.4-GHz band with a bandwidth of 125 MHz. A snapshot of the radio stations of our prototype is shown in Fig. 2.3, where the antenna is attached to a small cart with RF board and computer installed on the cart. We test the performance of our prototype in a typical office room that is located on the second floor of the Jeong H. Kim Engineering Building at the University of Maryland College Park. The layout of the floor plan of the office room is shown in Fig. 2.4 (a), where the AP is located at the place with the mark “**AP**” and the TD is located in the smaller office room marked as “**A**”. The detailed floor layout of room A is shown in Fig. 2.4 (b). Notice that with such a setting, the AP is working in the NLOS condition.

2.2.2 Evaluation of TR Properties

Here, we evaluate three important properties of the TR system, namely, channel reciprocity, temporal stationarity, and spatial focusing. Note that channel reciprocity and temporal stationarity are the two underlying assumptions of TR system, whereas spatial focusing is the key feature for the success of the proposed TRIPS.

2.2.2.1 Channel Reciprocity

We explore channel reciprocity by examining the CIR of the forward and backward links between the TD and the AP. Specifically, the TD first transmits a channel probing signal to the AP, and the AP records the CIR of the forward link. Immediately after that, the AP transmits a channel probing signal to the TD, and the TD records the CIR of the backward link. These procedures are repeated 18 times. One CIR realization of forward and backward links is shown in Fig. 2.5, where (a) shows the amplitude and phase of the forward channel and (b) shows those of the backward channel. In these figures, we can see that the forward and backward channels are very similar. By computing the correlation between the CIR of the forward link and that of the backward link, as shown in Fig. 2.6, we can see that, indeed, the forward and backward channels are highly reciprocal. Fig. 2.7 shows the TR resonating strength γ between most of the 18 forward and backward channel measurements with mean γ to be over 0.9. This result shows that the reciprocity is stationary over time.

2.2.2.2 Channel Stationarity

We then evaluate the channel stationarity of the TR system by measuring the CIR of the link from the TD to AP under three different settings: short-interval, long-interval, and dynamic environments with a person walking around. In the short-interval experiment, we measure the CIR repeatedly 30 times, and the duration between two consecutive measurements is 2 min. For the long-interval experiment,

we collect a total of 18 CIRs with 1-h interval from 9 A.M. to 5 P.M. over a weekend. Fig. 2.8 shows the TR resonating strength γ between any two CIRs from all 30 CIRs in the short-interval experiment, and Fig. 2.9 shows the TR resonating strength between any two CIRs from the 18 CIRs collected in the long interval experiment. We can see that the CIRs at different time instances are highly correlated for both the short interval and long interval, which means that the channel in an ordinary office does not vary much over time even with long duration. We then investigate the effect of human movement. We collect, every 30 s, the CIRs with a person walking randomly between the AP and the TD. Fig. 2.10 shows the TR resonating strength γ between the 15 collected CIRs. The experimental result shows that, even with a person walking around, the TR resonating strength remains high among all of the collected CIRs. Therefore, the proposed TR positioning system does not require a frequent update of the CIR information. All these results are consistent with the observations in [50], the main reason being that the multipaths come from the refractions and reflections of the indoor environment, which are quite stable, as long as there is no severe disturbance of the environment.

2.2.2.3 Spatial Focusing

As we have previously discussed, the CIR comes from the surrounding scatterers and such scatterers are generally different for different geographical locations. Therefore, the CIR is location specific and unique for each location. By utilizing such a unique location-specific CIR, TR can focus the transmitted power only to



Figure 2.11: Three-dimensional architecture for moving the locations of the TD.

the intended location, which is known as the spatial focusing effect of the TR system. We quantify such a spatial focusing effect using the maximum energy that the TD can harvest from the AP. To evaluate the spatial focusing effect, we conduct experiments by moving the locations of the TD on a 3-D architecture, as shown in Fig. 2.11, within a 1 m by 0.9 m area in room A. The grid points are 10 cm apart, which leads to 110 evaluated locations in total.

We collect the CIR of all evaluated locations and compute the focusing gain by varying the intended location. The results are shown in Fig. 2.12, where we can see that the focusing gain at the intended location is much larger than that at the unintended location, i.e., there exists a very good spatial focusing effect. In Fig. 2.12, we also observe some repetitive patterns. Such repetitive behavior is due to the representation of 2-D locations using 1-D index. To better illustrate the spatial focusing effect, we fix the intended location as the center of the test area and show

in Fig. 2.13 the spatial focusing by directly using the real geographical locations. Clearly, we can see very good spatial focusing performance. Note that similar results are observed for all other intended locations.

We further evaluate the spatial focusing effect in a finer scale with 1-cm grid spacing, and the results are shown in Fig. 2.14. We can see that there is reasonably graceful degradation in terms of the spatial focusing effect within a 5 cm by 5 cm region, which is consistent with the fact that channels are uncorrelated with a half-wavelength spacing (the wavelength is around 5 cm when the carrier frequency is 5.4 GHz). In such a case, when a user is located between grid points with 10-cm spacing, it may not be localized correctly. Nevertheless, this can be easily solved by asking the user to rotate the device, e.g., smartphone, such that the antenna can cross the 10-cm grid points.

2.2.3 Localization Performance

From the results in the previous section, we can see that the CIR acts as a signature between the AP and the TD, and it drastically changes, even if the location is only 10 cm away. Here, we will examine the performance of our proposed indoor positioning algorithm.

To evaluate the performance, we use the leave-one-out cross validation. Specifically, we pick each CIR as the test sample and leave the rest as training samples in the database. Then, we perform our proposed algorithm, i.e., the online positioning algorithm, and evaluate the corresponding performance. There are totally 3016

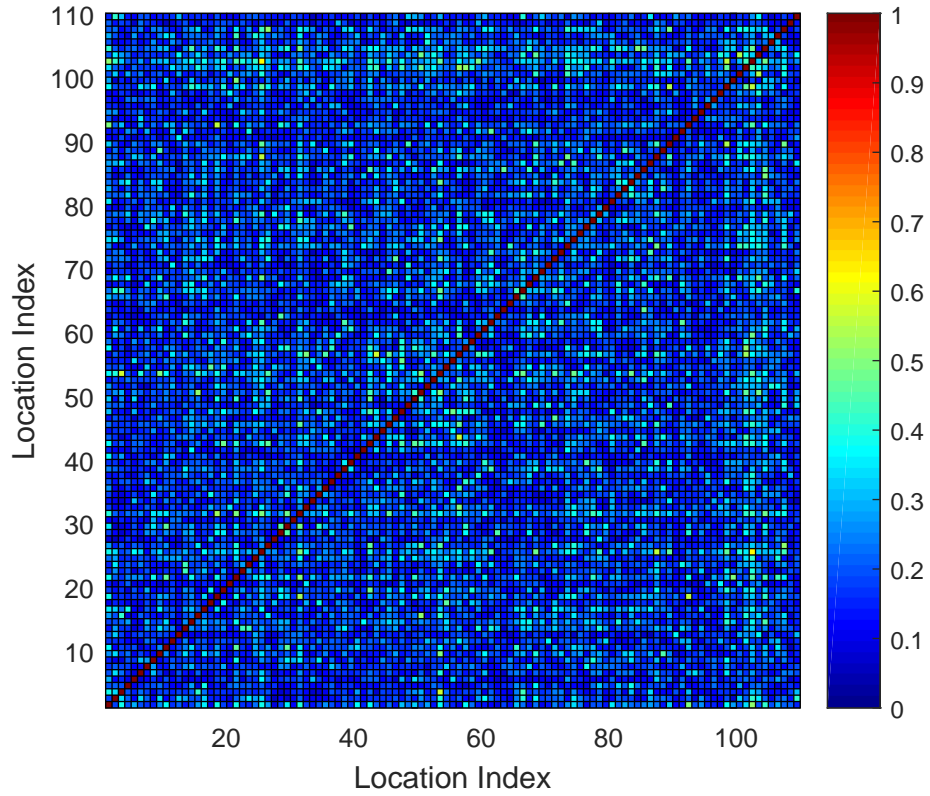


Figure 2.12: γ of all grid points by moving the intended location within 1 m by 0.9 m area. Every dot in the figure stands for one grid point where two neighboring grids points are 10cm away from each other. The horizontal/vertical axis is the location index with 1-D representation. Each value in (i, j) represents the focusing gain at location j (location index with 1-D representation) when the intended location is i (location index with 1-D representation).

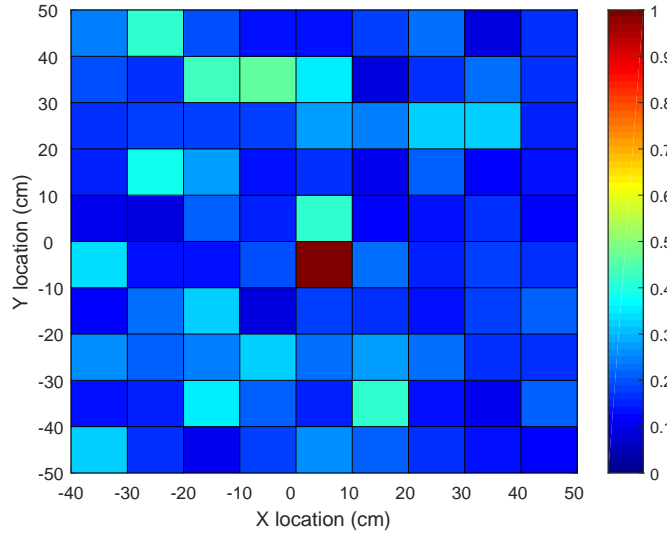


Figure 2.13: Geographic distribution of γ with the intended location at the center of the area of interest.

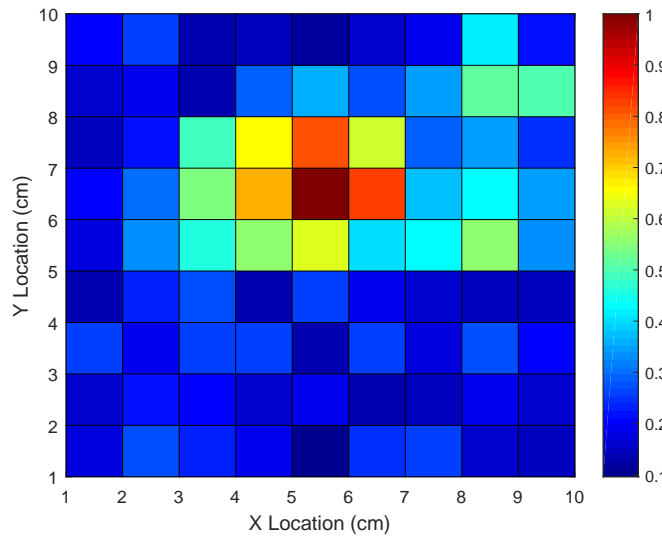


Figure 2.14: Fine-scale geographic distribution of γ .

Table 2.1: Localization performance with 10-cm localization accuracy

Number of Trials	3016
Number of Error	0
Error Rate	0%

CIRs for the 110 grid points, which leads to a total of 3016 trials. The localization performance is shown in Table 2.1, in which we can see that our proposed indoor localization algorithm gives zero error out of a total 3016 trials, which achieves 100% accuracy with no error in the 1 m by 0.9 m area of interest. Note that this result is achieved with a single AP working in the NLOS condition using one CIR.

2.2.4 Discussions

From the experimental results and discussions, we can see that the proposed TRIPS is an ideal solution to the indoor positioning problem since it can achieve very high localization accuracy with a very simple algorithm and low infrastructure cost summarized as follows.

- From the experimental results, we can see that, with a single AP working in the 5.4-GHz band under the NLOS condition, the proposed TRIPS can achieve perfect centimeter localization accuracy. Such localization accuracy is much better than that of existing state-of-the-art IPSs under the NLOS condition, which typically achieve meter-level localization accuracy. Moreover, the accuracy can be improved if we increase the resolution of the database,

which, however, will increase the size of the database and, thus, the complexity of the online positioning algorithm.

- Based on the TR technique, the matching algorithm in our TRIPS is very simple, which just computes the TR resonating strength between the estimated CIR and that in the database. Compared with existing approaches, our method does not require complicated calibrations and matchings.
- Although the localization performance can be further improved with multiple APs, our method only uses a single AP and has already achieved very high localization accuracy under the NLOS condition. Moreover, no special apparatus is needed for the AP. Therefore, the infrastructure cost of our TRIPS is very low.
- The size of the database is determined by three factors, i.e., the room size, the resolution of the grid point, and the number of realizations at each grid point. For a typical room such as room “A” shown in Fig. 2.4 (a), the size is 5.4 m by 3.1 m. Considering a resolution with 10-cm spacing between two neighboring grid points, there are a total of 1760 grid points. Suppose 20 CIR realizations are collected at each grid point, where the length of the channel L is 30 and where each tap of CIR is represented with 4 bytes (2 bytes for the real part and 2 bytes for the imaginary part). Then, the size of the database is $1760 \times 20 \times 30 \times 4 = 4\,224\,000$ bytes (4.2 MB). Such a database is reasonably small, which can be easily stored with an off-the-shelf storage device. Moreover, all system configurations, including the grid size, the number of realizations,

and the channel length L , are all adjustable to fit a specific environment at a desired localization performance.

- The proposed TRIPS is not limited to the 5.4-GHz band. It can be also applied to the ultrawide band with a larger bandwidth, where we expect to achieve much higher localization accuracy.

2.3 Summary

In this chapter, we have proposed a TRIPS by exploiting the unique location-specific characteristic of CIR. Specifically, we have addressed the ill-posed single-AP localization problem by decomposing it into two well-defined subproblems. One subproblem is calibration by building a database that maps the physical geographical locations to the logical locations in the CIR space, and the other subproblem is matching the estimated CIR with those in the database. We built a real prototype to evaluate the proposed scheme. Experimental results show that, even only with a single AP under the NLOS condition and a single realization of online measurements, the proposed scheme can still achieve 100% localization accuracy at the scale of 10 cm within a 0.9 m by 1 m area of interest. Furthermore, the finer grid experiment also shows the system's capability to provide 1 to 2 cm precision performance in the indoor positioning scenario.

Chapter 3

Virtual Checkpoint based Indoor Tracking System

As discussed in the Chapter 2, the detail, location-specific CIR information can be used for precise indoor positioning. TR system uses wide bandwidth for detail sampling of the CIR, and preserves the information of the surrounding environment embedded in the CIR. Once the CIRs of the intended locations are recorded in the database \mathbf{D} , the TRIPS can identify the location of the user with simple algorithm by calculating the time reversal resonating strength between the CIR from the unknown user and the CIRs in the database.

Based on the experiment result in Chapter 2, the CIR information is precise for localization and the TRIPS correctly identifies the location with in a 1 m by 0.9 m area. Such precision indicates that the area can be viewed as a checkpoint because the system can detect the user's location whenever the user passes. The collection of CIRs acts like a normal checkpoint just like a checkpoint installed at the entrance of building. We therefore define this area as a virtual checkpoint (VC), within which the system stores the complete CIR information. We name the indoor tracking system as virtual checkpoint based tracking system, or the VCTR system.

The VCTR system detects the presence of the user by calculating the γ between the received CIR of the user with the CIR information of the VC in the

database. Moreover, multiple VCs can be deployed in the VCTR system to keep track of the movement of the target from one VC to another. In the following Sections, we describe in detail the implementation and discussion of the VCTR system.

3.1 Virtual Checkpoints

The idea of the VC in the VCTR system stems in the fact that the CIR from the unknown user produces high γ values with the CIRs recorded in the database. Therefore the construction of the VC needs to ensure that whenever the target passes through VC, the collected CIR can be matched to the CIRs in the database. There are several points and parameters in VC construction that need special consideration for the proper operation of VCTR system and we discuss these detail of the VC construction in the following.

- CIR Density d : The density of the CIR in the VC depends on how γ decreases with the displacement from the measured location to the user's actual location. Since we do not know whether the user hits the exact location where the CIRs are collected or not, the rate of the decrease in γ is an important factor on how dense the CIR distribution in the VC shall be. The faster the decrease in γ with the displacement, the denser the CIR distribution the VC shall be. The density needs to be high enough such that we can ensure that the CIR collected from the unknown user still shows high γ with the CIRs in database even not passing through the exact location. According to our experiment, the area with high γ around the exact location is about 2 cm in radius. In our

VC construction, we proposed that using a 1 cm separation between CIRs is a suitable balance between performance and computation complexity. Based on this density, the VCTR locates the user with very low false alarm in our experiment.

- Frequency of CIR Probing f : The frequency of probing affects the construction of the VC. The frequency needs to be high enough such that whenever the target passes through the VC, the VCTR receives at least one CIR probing signal within the VC. The higher the frequency, the smaller distance the target moves between consecutive CIR probings at VCTR, and therefore the smaller the thickness the VC needs to be. The frequency of CIR probing is restricted by the underlying communication protocol and platform the time reversal technique is applied upon. Moreover, some protocols may allow uniform probing of the CIRs, such as a round robin probing in a centralized network, while others may suffer from contention between other targets in the VCTR system or from the interference of other transmitting systems occupying the same frequency band.
- Speed of the Target v : Since the VCTR system needs to receive at least one CIR probing signal when the target passes the VC, the speed of the target affects the construction of VCs. When the target moves faster, the VC needs to be thicker to assure that at least one CIR is collected when the target passes VC.
- VC i dimension (x_i, y_i, h_i) : The (x_i, y_i, h_i) denotes the width, the depth and the

height of the VC respectively. The target application dictates the dimension of the VC, such as the user’s speed, the CIR collection platform, and the actual environment, etc. The depth y_i grows large when the target speed is faster. The width x_i is affected how big the hall way or the target area is, while the height h_i is affected by the possible range where the TR device will be put during the tracking.

These four parameters are the main factors that affects the construction of the VC in terms of size and the CIR density. Other elements that affect the VCTR performance, but not the VC construction are discussed in 3.6.

3.2 Virtual Checkpoint Construction

A schematic diagram of the prototype of the VC constructing machine is depicted in Fig. 3.1, where the proposed prototype contains two modules. The upper half is the CIR collection module, and the lower half is the motor controlling module. The CIR collecting module can be implemented using any platform that collects CSI information at satisfactory frequency. In this prototype system, we use the Galileo board equipped with Atheros WiFi card to collect CIR information, where the Galileo board acts as a small computer controlling the transmission of the WiFi card. Although the bandwidth of the WiFi system are only 20 MHz or 40 MHz, the spacial temporal focusing effect is still observable when we concatenate the CIR information from different antenna pairs to form the virtual bandwidth as proposed in [3]. In this VCTR prototype, the WiFi RF interface has 3 antennas at

both the transmitter and receiver which gives in total 9 links with 40 MHz for each link.

The upper part of Fig. 3.1 shows the CIR collection module with a pair of AP and TD pair. The AP receives commands and ask for CIR information from the TD. This pair is used for continual collection of the CIR information while the motor controlling module moves the structure on the VC constructing machine where the TD is mounted. The lower part of Fig. 3.1 shows the motor controlling module that is composed of a central PC, a Galileo board running the controlling program, and a remote control PC. The central PC hosts the controlling graphic user interface (GUI) and maintains connection with the CIR collecting module and the motor controlling program. Fig. 3.3 shows a screenshot of the GUI we develop and the user can adjust the parameters of the VC. The central PC has two network interface, the first one is connected to the AP via Ethernet, and the other one is connected to the controlling program on the Galileo. A mobile remote control PC is set up to control the GUI at the central PC and the user can start and stop the CIR collection from afar. Detail information of the prototype is described as follows:

- The Central PC: Host to the GUI and the post processing algorithm of the collected CSI. GUI sends commands to the AP via Ethernet and send commands to the motor controlling module via a closed WLAN network. A light weight mobile PC mirrors the desktop of the Central PC via the closed WLAN network.
- The Motor Control: Galileo runs Linux and is connected to the Central PC.

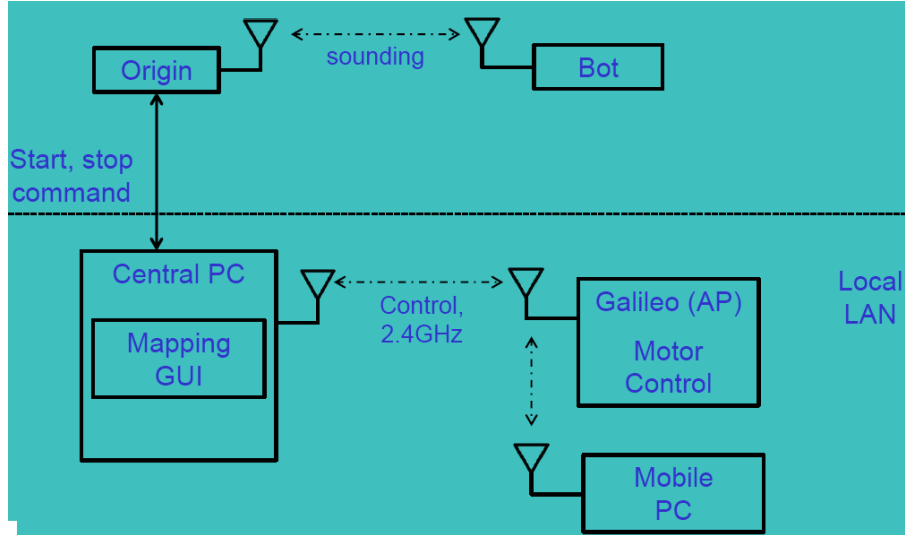


Figure 3.1: Mapping machine system.

The Galileo connects to two motor shields that control the two step motors and a DC motor. The Galileo also acts as an access point (AP) at 2.4 GHz that provides WLAN network for the Central PC and the Mobile PC to establish remote desktop connection.

- AP and TD pair: The AP connects to the Central PC via Ethernet and send command to TD for CSI collection.
- Movement Structure: The structure provides movement in the width, depth, and height directions (x, y, h) . The width is controlled by the DC motor while the other two dimensions are controlled by step motors for precise distance control. The precision of y and h axis are currently set at 1 cm. Fig. 3.2 shows a picture of the prototype of VC collecting machine. The dimensions of x , y , and h is the shown in Fig. .

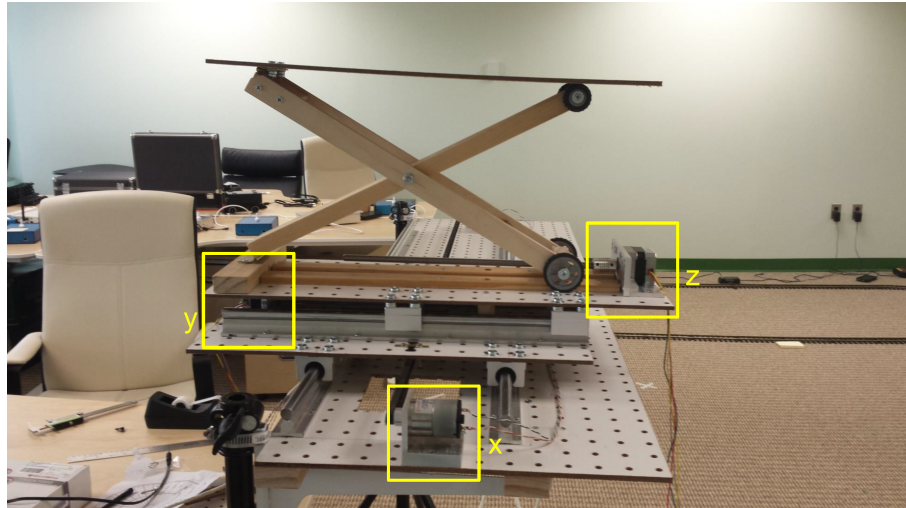


Figure 3.2: Prototype of the VC measuring machine.

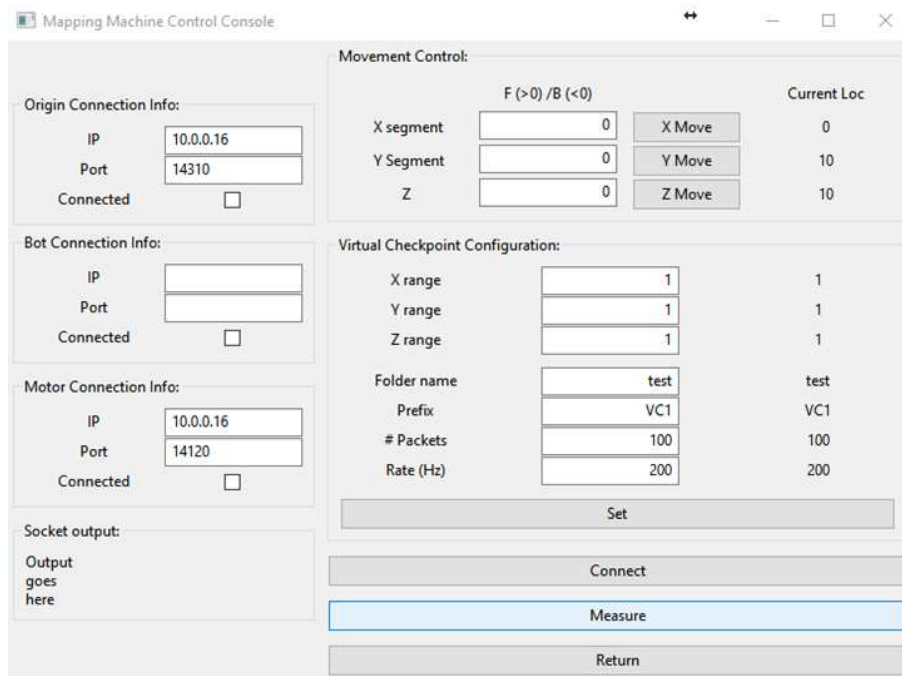


Figure 3.3: Screenshot of the VC collecting GUI.

3.3 System Implementation

Here, we list out some implementation details of the mapping system. Majority of the system is written in Python 2.7, and the GUI implementation is based on the wxPython package. Some calculation intensive modules are written in C++ to reduce the time for CIR post processing. The mraa package is used in the motor controlling module for communication between the Galileo and the motor shield via the I2C interface.

- Multi-thread: Python GUI is the main thread and the CSI collection is performed in a separate thread. Main thread controls the motor movement in the x direction while the other thread performs the CIR collection. The collected CIR is saved directly into the target folder and no interprocess communication is needed. The two threads will synchronize before the next CIR measurement.
- MVC model: View and Control modules are implemented together and is responsible of the visual content and the control flow of the GUI events. Model module is implemented as a class, which performs sanity check on the range of the location variables.
- Motor Control: The direction of the movement in the x , y and h are coded in the motor controlling module. When the executable of the central PC is ported to other devices, no change needs to be made at the GUI side. Redefinition of functions of the motor controlling module running on the Galileo board changes the direction of the movement.

- CIR Parser: Implemented in $C++$ for fast parsing of the data and calculating γ . The output CIR information from the AP is in raw bits and the CIR parser parse it into appropriate CIR data structure. The calculation of the γ is also implemented using $C++$ to speed up the intensive calculation load.

3.4 System Operation

There are two phases in the VCTR system operation: the VC collecting phase and the online detection phase.

- VC collecting phase: The VC Constructing machine is placed at the location where VCs locate. Multiple pairs of APs and TDs can perform CIR collection simultaneously to speed up the total collection time. The collected CIR information is stored in the database \mathbf{D} . Specifically, for VC i , we collect $\mathbf{H}_i = \{\mathbf{h}_i(x, y, h) | (x, y, h) \in (x_i, y_i, h_i)\}$. The database is simply the collection of all the VC, i.e. $\mathbf{D} = \{\mathbf{H}_i, \forall i\}$.
- Online detection phase: The user keeps transmitting CIR probing signal. The VCTR system calculates the γ of the received CIR $\hat{\mathbf{h}}$ from the unknown user with the CIRs $\{\mathbf{h}, \mathbf{h} \in \mathbf{H}_i\}$ in the database. When the calculated γ is higher than a threshold T , the VCTR system detects that the user is in one of the VCs. The estimated location of the user is the VC that gives the largest γ , that is $\hat{i} = \arg \max_{i, \gamma_i > T} \gamma_i$.

3.5 Experiment

To evaluate the performance of the proposed VCTR system, we perform the following experiment. Fig.3.4 shows an example of VCTR system operation. In this example, the AP is placed at the corner of the floor while the user walks a straight line and passes one VC along the way. To first validate that the proposed VCTR system detects the user's passing through, we plot out the maximum γ of the system when the user walks through the VC. Fig.3.5 shows the max γ calculated between the received CIR probing and the CIRs in the database. The system observes a prominent peak in maximum of γ across the time, which clearly indicates that the user is detected at the VC.

After validating the concept of the VC, we perform experiments to gather the statistics of the maximum γ in two cases: when the user actually passes through the VC and when the user wonder around the VC. We repeat the experiment 100 times and calculate the CDF of the maximum γ value of the two cases. Fig.3.6(a) shows the CDF of the maximum γ when the user passes VC, while Fig.3.6(b) shows the CDF of γ when the user does not passes VC. We can see that there is a clear gap between the CDF of γ of the two cases and a properly chosen threshold can perform perfect detection with very low probability of false alarm. Fig.3.7 shows the ROC curve obtained by the two CDF curves, which shows that the VC based detection achieves perfect detection with very low false alarm probability.

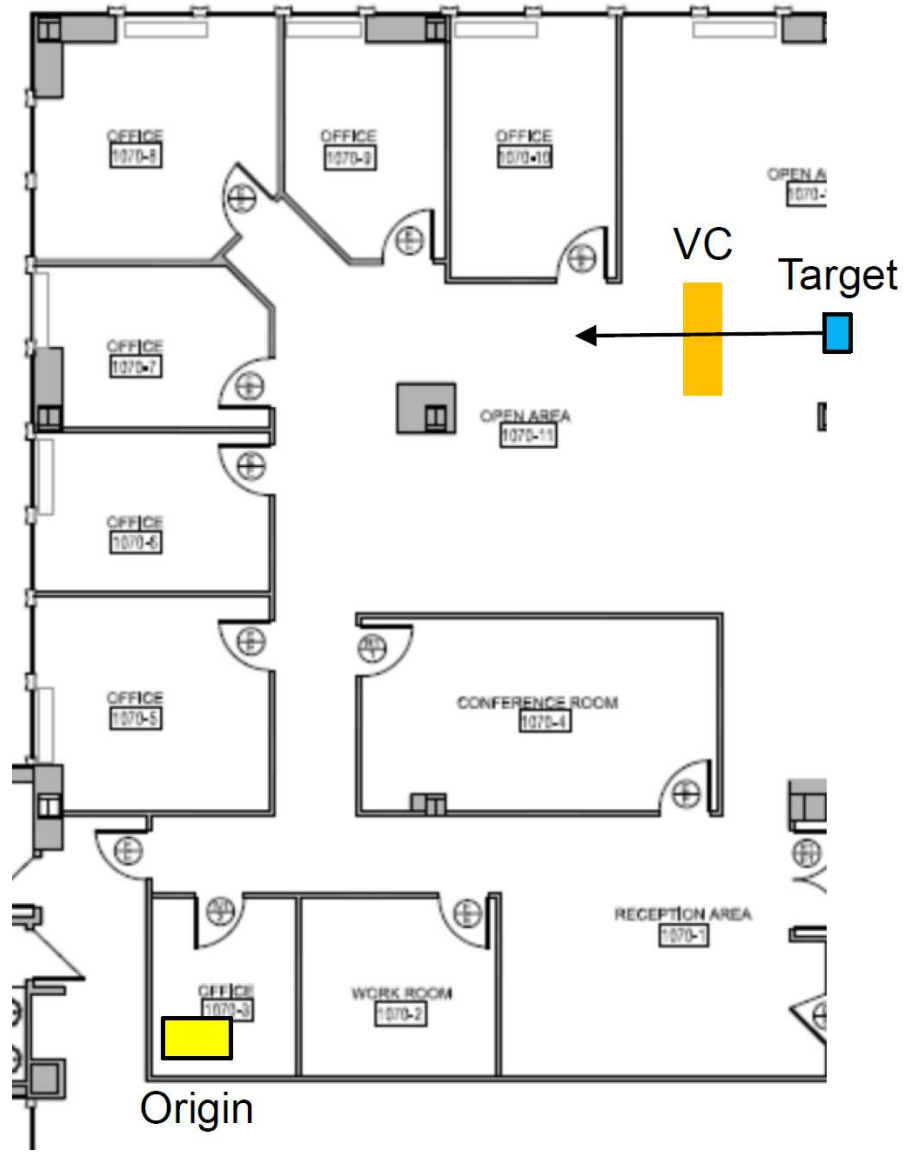


Figure 3.4: Floor map showing the location of the Origin and the VC.

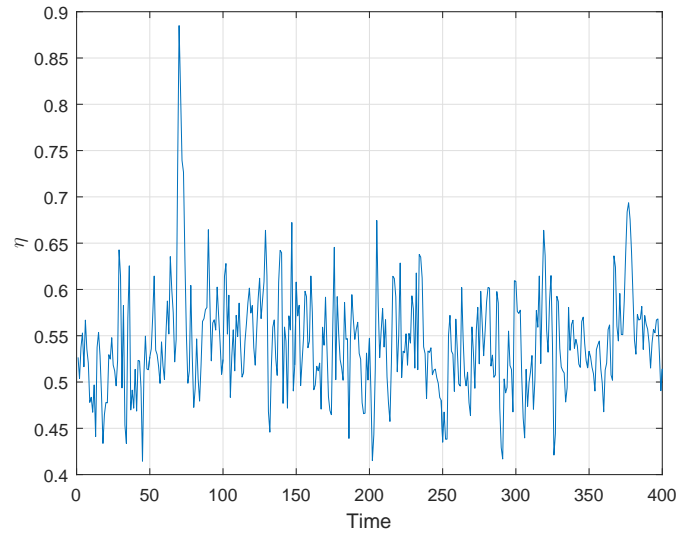
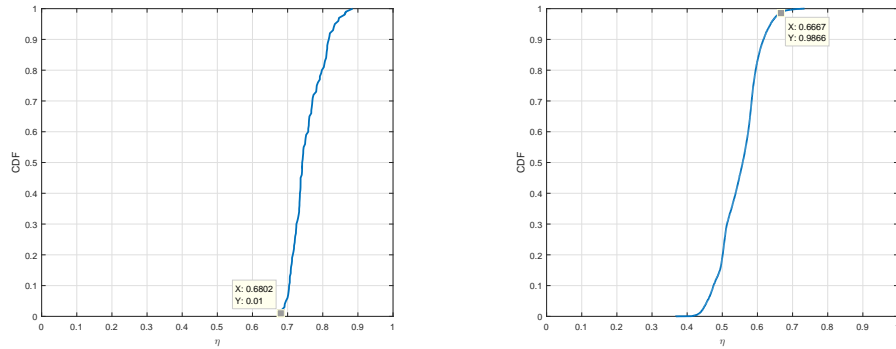


Figure 3.5: γ when hitting a VC.



(a) CDF of γ when the user passes VC. (b) CDF of γ when the users does not pass VC.

Figure 3.6: CDF of the maximum of γ between the CIR of the unknown users and the CIRs in the VC database.

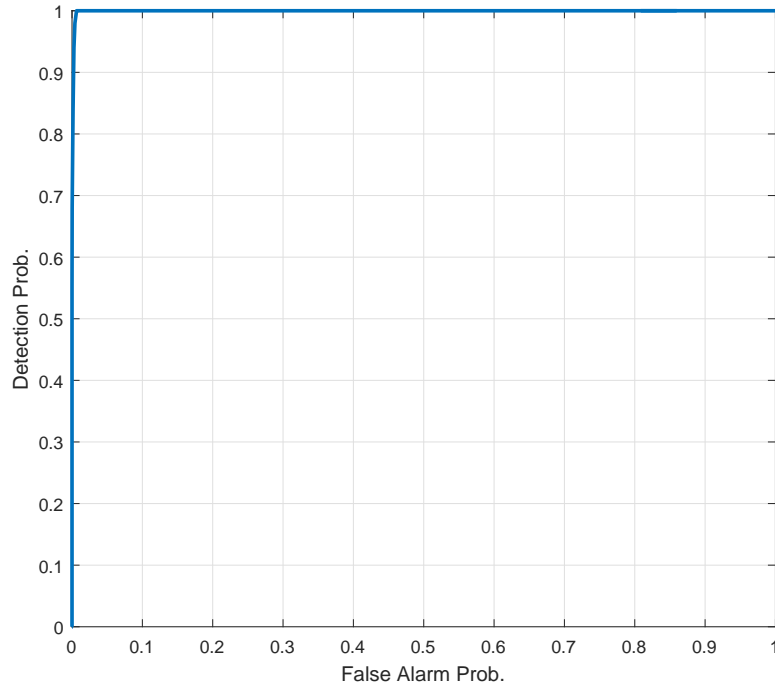


Figure 3.7: ROC of VC detection.

3.6 Discussion

We discuss some issues concerning to the implementation of VC in this Section.

- The γ Waterlevel: The TRIPS declares the unknown user to be at the VC when the γ of the received CIR and the CIR from the VC is larger than a threshold. This simple detection algorithm produces false alarm when the target passes through locations with higher γ is calculated using the CIRs around the VC, which we call the γ waterlevel. The γ waterlevel is different for each of the VC and the waterlevel is affected by the environment, such as the LOS, NLOS setting, the room layouts, etc. A uniform threshold for all the VCs raises the false alarm and gives the wrong location estimate which causes

trouble for following tracking algorithms. Therefore, an optimal threshold of γ for each VC shall be found considering the statistical behavior of γ around the virtual checkpoint.

- **Hardware Consistency:** The RF component used for VC CIR collection and the RF component used by the user are not the same one in general cases. Therefore, the hardware inconsistency between each RF interface shall be considered when the system is implemented. The inconsistency causes a lowered γ even if the target is in the VC, which results in a higher false alarm rate. Experiments show that the hardware consistency can be accountable for a 0.3 drop in γ in some cases.
- **Database Size:** The database size is related to size of the VC. In order for the user to transmit at least one CIR probing signal when passing through the VC, the CIR has to be dense enough. Also, the user's speed and the transmitting frequency also constraints the thickness of the VC, which also affects the size of the final VC database. When we factor in multiple VCs in the system, the computation load may be intense and parallelization is needed. For the current VC, we have 6 cm in the depth, 6 cm in height, and about 75 cm in width, with 1 cm resolution at all dimensions, and each CIR realization is 2816 bytes. Therefore, the database size for one VC is about 7.6 MB.
- **Side Information:** The location detection via VC only detects user at the VC, where the exact location of the user between VCs is not clear. In order to get the estimate of the user between checkpoints, side information from other

sensors can provide an estimation between VCs. Also, the estimated location can also narrow the set of VCs that the VCTR system has to calculate the γ using the received CIR.

3.7 Summary

In this chapter, we propose a novel indoor tracking system that track the target via virtual checkpoint. The essence of the construction of virtual checkpoint stems at the spatial temporal focusing effect of the TR system as shown in Chapter 2, where location identification is possible using the location-specific CIR information. We built a prototype machine for collecting CIR information which operates automatically. We then verify the virtual checkpoint concept via a simple path and a virtual checkpoint. The experiment data shows that the proposed virtual checkpoint captures the activity of the user and gives estimation of the target's location.

Chapter 4

Time Reversal Medium Access Control

In previous chapters, we have developed and verified the performance of the TR indoor positioning system based on the unique spatial temporal focusing effect. The location-specific CIR, on the other hand, also benefits the TR system with the spatial temporal focusing effect [55] that focuses the transmitted energy to the intended user. By selecting the waveforming signature as the time-reversed and conjugated version of the intended receiver's CIR, the transmitted waveform adds up constructively at the exact location of the intended receiver, while the waveform adds up randomly at all other locations. The receiver receives maximum signal energy with small energy leakage to surrounding users. The energy focusing due to location-specific CIR information separates TR users operating on the same frequency band and allows simultaneous access, leading to the design of time reversal division multiple access (TRDMA) system that provides service to a large amount of users [20].

The other 5G candidate, the massive MIMO system, achieves the energy focusing by using a large number of antennas [29]. The massive MIMO system concentrates the transmitted energy at the intended user by adjusting the weight vector of the antennas, which is known as beamforming. With the increase of the number

of antennas, the massive MIMO system directs the energy to more intended users with small energy leakage to the unintended users, and therefore the system is able to supports lots of users.

However, with the ever-increasing number of users in the foreseeable IoT future, the 5G systems cannot indefinitely support all users simultaneously due to the fixed usable bandwidth and/or the fixed number of antennas. Interference among the users will increase and the energy focusing effect can no longer support the massive users with satisfactory quality of service (QoS). As a result, a system scheduler that dictates when and whom to access the system simultaneously and maximizes the system performance is desirable. The scheduler also requires a reasonable complexity in order to operate in real time with strict scheduling deadlines.

Many existing systems already have schedulers deployed, however, none can be implemented directly on the TR and the massive MIMO system. There are two main reasons. The first is the fundamental differences in the physical layer design. In existing and widely deployed OFDMA systems, such as the LTE system, the scheduler allocates the resource blocks (RBs) that are mutually orthogonal in time and frequency to users. The RBs are allocated based on system requirements such as the QoS awareness of the users [28, 46, 52] or the weighted sum rate of the overall system [23]. However, in the case of TR system, the transmission resource is not mutually orthogonal and all the users are using the same transmission band. Therefore a new scheduler design is needed to select a subset of users for transmission while managing the in-band interference. On the other hand, although OFDMA can be an element for massive MIMO system, the interference between users still

exists for the users on the same frequency band and interference management is still desirable.

The second reason is that with the massive number of users in the system, it is possible that the system cannot accommodate the users simultaneously via power control. In a typical power control scheme, the system adjusts the transmit power to different users in order to control the interference introduced to unintended users [24, 39, 59]. However, when a massive number of users are present in the system, all the proposed power allocation based algorithm might not be feasible due to minimum transmitted power requirements of the users. The system therefore needs to efficiently select a subset of users for transmission that not only maximizes the system objective but also meets the individual QoS requirements.

In a scheduler design, it is usually assumed perfect channel information, whereas the channel information is imperfect in reality. Several factors contribute to the imperfect channel information including the aging of the channel, the received noise during channel estimation, the pilot contamination between users, and so on. The imperfect channel information not only degrades the performance of the physical layer, but also deteriorates the scheduler performance. Robustness against imperfect channel information in scheduler design is therefore highly desirable to sustain the system performance when the channel information is inaccurate.

In order to address the above issues, we propose a novel medium access control (MAC) layer scheduler design by taking into consideration of the unique focusing effect for both the TR and massive MIMO system. In the first part of the chapter, we focus on the scheduler algorithm that selects a subset of users and maximizes the

system weighted sum rate. The optimization problem is transformed and formulated as a mixed integer quadratically constrained quadratic program (MIQCQP) [53] where the optimization problem is solved using an optimization solver. In the second part, we focus on the impact of imperfect channel information on the scheduler performance. We analyze a channel estimation scheme for TR system proposed in [36] and identify similar channel estimation error distribution as in the massive MIMO case. We evaluate the robustness of the proposed scheduler against imperfect channel information provided by the channel estimation scheme.

The main summary of this chapter is as follows:

1. We propose an efficient scheduler algorithm for 5G system that maximizes the weighted sum rate by selecting a subset of users for transmission. The system objective and QoS constraints are transformed into a MIQCQP with empirical linear time complexity.
2. We analyze the channel estimation error distribution of the TR system. Analysis shows that the TR channel estimation scheme reduces the channel estimation error power and reveals a similar estimation error distribution as in the massive MIMO case.
3. We evaluate the proposed scheduler under imperfect channel information. Experiment results show that the proposed scheduler is robust against imperfect channel information with small performance degradation.

The chapter is organized as follows. System description for both the TR and massive MIMO system is given in Sec.4.1. The energy focusing effect of both TR

and massive MIMO systems is illustrated via simulation in Sec.4.2. The scheduler objective and user requirements are described in Sec.4.3 and the MIQCQP formulation is developed. In Sec.4.4, we investigate the impact of the imperfect channel information on the performance of the scheduler. Simulation results are presented in Sec.4.5 where the performance of the scheduler is evaluated under various settings. Finally, a conclusion is given in Sec.4.6.

4.1 System Overview

We give brief overviews of the TRDMA downlink system and the massive MIMO downlink system and introduce the spatial focusing effect of both systems.

4.1.1 Time Reversal Division Multiple Access System

A schematic view of a TRDMA downlink system is depicted in Fig.4.1, where N users/terminal devices (TD) are served. The access point (AP) first upsamples the symbol stream for user i by the backoff factor D_i . The upsampled symbols are encoded using the corresponding waveforms \mathbf{g}_i which are assigned to the users. The AP transmits the summed signal with a single antenna and the transmitted signal passes through individual users' channels \mathbf{h}_i . The users adjust the power using one tap gain, downsample the received signal and then perform detection to estimate and recover the transmitted symbols.

Using the time reversed and conjugated CIR \mathbf{h}_i between the AP and user i as the waveform \mathbf{g}_i , user i obtains the maximum signal power. However, the interuser

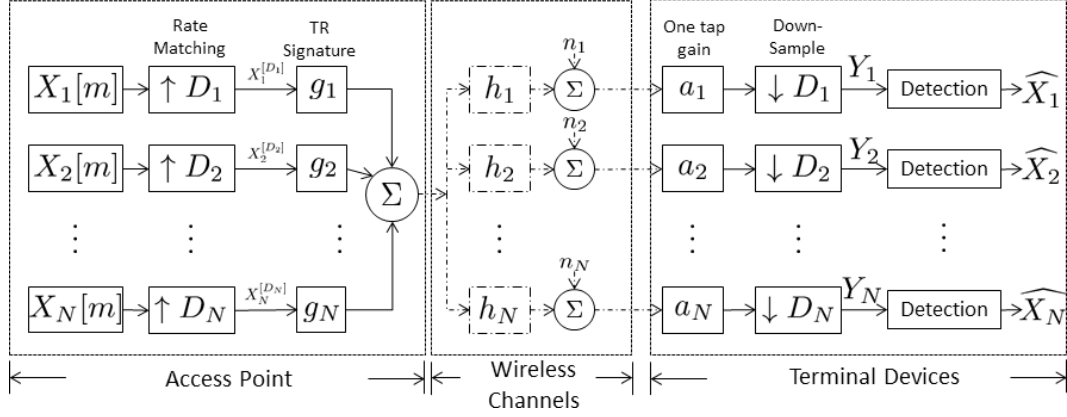


Figure 4.1: System diagram of a TRDMA system.

interference (IUI) and intersymbol interference (ISI) reduce the SINR of users and therefore the TR waveform \mathbf{g}_i can be specifically and jointly designed for the system to meet system requirements. Several waveforming algorithms have been proposed in [58] and [57] to alleviate IUI and ISI and to increase the SINR.

4.1.2 Massive MIMO system

Suppose that there are M antennas in the base station serving K one-antenna terminal devices. The channel \mathbf{h}_i^M from the base station to the user i is an M by 1 vector where the j th element is the channel from the j th antenna to the i th user. We assume a narrowband massive MIMO system which observes one tap channel due to the limited subcarrier granularity. Proper beamforming vectors \mathbf{g}_i^M can be designed to steer the energy to the intended user i , such as the maximum-ratio transmission and zero forcing beamforming in [42].

The TR system utilizes the time-reversed and conjugated CIR as precoding waveform to transmit the energy to the specific users. Because the CIR are

location-specific [55], the energy only concentrates at the intended users with small energy leakage to the surroundings, which is called the spatial focusing effect. The large bandwidth enables the TR system to resolve more taps from location-specific channels and focuses the energy more sharply to the intended user. On the other hand, the massive MIMO system focuses the energy to the intended users using the maximum-ratio-combining beamforming weights. By installing more and more antennas, the massive MIMO system concentrates the energy more sharply at the intended users as the TR system does with a larger bandwidth. The spatial focusing effect resulting from either larger bandwidth or more antennas enables the 5G system to pinpoint the energy to the exact users, to reduce the interference leakage, and therefore to accommodate more users than that in existing systems. In order to illustrate the spatial focusing phenomenon, we conduct a simulation in both TR and massive MIMO systems to reveal how the focusing effect becomes prominent with the increase in either bandwidth or the number of antennas.

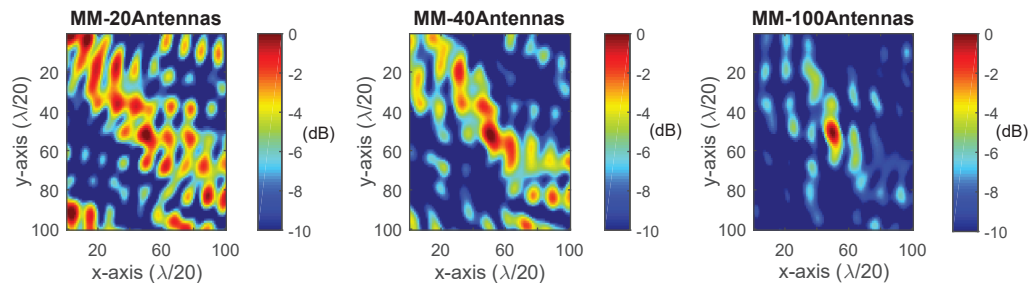
4.2 Spatial Focusing Effect

With proper waveform design \mathbf{g}_i and beamform weight design \mathbf{g}_i^M , both the systems focus energy only at the intended users. The ability of the energy transmission targeting at specific users is affected by the degree of freedom (DoF) of the design, which is the number of variables in \mathbf{g}_i or \mathbf{g}_i^M . The TR system increases the DoF by using a large bandwidth which results in a massive number of observed CIR taps, while the massive MIMO system increases the DoF by installing a massive

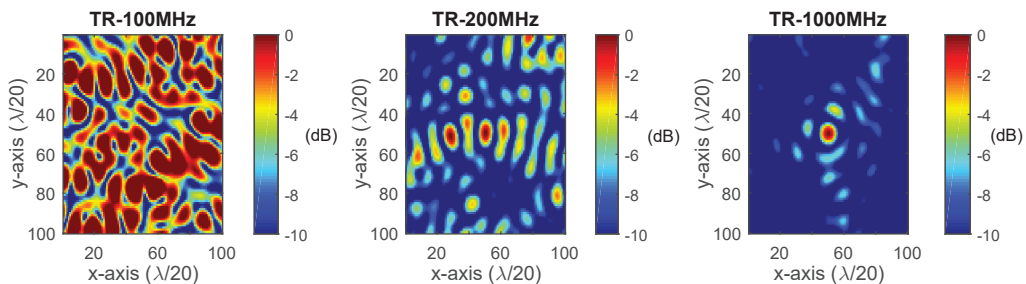
number of antennas. The larger the bandwidth and the number of antennas, the larger DoF, and therefore the better spatial energy focusing at the locations of the intended users.

To illustrate the spatial focusing effect of both systems with different DoF, we conduct a simulation based on ray-tracing techniques in a discrete scattering environment. 400 scatterers are distributed randomly in a $200\lambda \times 200\lambda$ area, where λ is the wavelength corresponding to the carrier frequency of the system. The wireless channel is simulated by calculating the sum of the multipaths using the ray-tracing method given the locations of the scatterers. Without loss of generality, we use a single-bounce ray-tracing method to calculate the channels for both the TR system and the massive MIMO system on the 5GHz ISM band. We select the reflection coefficients of the scatterers to be i.i.d. complex random variables with uniform distribution in amplitude $[0, 1]$ and phase $[0, 2\pi]$. For the massive MIMO system, the linear array is configured with the line facing the scattering area and the interval between two adjacent antennas is $\lambda/2$. The distance from the transmitter and the intended location is chosen to be 500λ for both systems.

To show the effect of system DoF on the spatial focusing effect, we adjust the transmitting bandwidth of the TR system and the number of antennas in the massive MIMO system. The transmitter of the TR system transmits with bandwidths ranging from 100 MHz to 1GHz with one antenna, where a wider bandwidth observes more CIR taps and increases the system DoF. The number of antennas in the massive MIMO system is selected from 20 to 100 with bandwidth fixed at 1MHz in the simulation. We select the matched filter waveform and beamforming weights



(a) Normalized field strength in a $5\lambda \times 5\lambda$ area centered around the receiver of a massive MIMO system.



(b) Normalized field strength in a $5\lambda \times 5\lambda$ area centered around the receiver of a TR system.

Figure 4.2: Demonstration of the spatial focusing effect for both TR and massive MIMO systems with different DoF.

in the TR system and the massive MIMO system, respectively.

We consider the received energy strength in a $5\lambda \times 5\lambda$ area around the location of the intended user. Fig. 4.2 shows the simulation results for both systems with a single channel and scatterer realization, and we normalize the maximum received energy to 0dB. We can see that the energy focusing effect becomes more obvious at the intended location with the increase in the bandwidth and the number of antenna, which is the result of larger DoF to concentrate the energy at only the intended users.

However, a closer look at the energy field in Fig. 4.2 reveals that even with large transmitting bandwidth and massive number of antennas, energy leakage still occurs at the surrounding of the intended users. The energy leakage causes the IUI and the interference level increases when the number of users grows. Scheduler design is therefore desirable to perform interference management by selecting a subset of users for transmission. In essence, the user selection is to choose a subset of users such that the energy leakage has small interference to any of the other selected users in order to reduce the IUI and to increase the total transmission rate.

4.3 Downlink User Selection Algorithm

In this section, we detail the algorithm for maximizing the weighted sum rate in the downlink system. To be specific, the scheduler receives the normalized interference matrix and the allocated transmission power for each of the users from the physical layer and the minimum required transmission rate for the user from the ap-

plication layer. The scheduler maintains weights for the users to adjust the fairness and to avoid starving due to poor channel condition and shadowing. Based on the information, the scheduler selects a subset of users to transmit simultaneously and maximizes the weighted sum rate while satisfying the minimum SINR requirement for the selected users.

4.3.1 TRDMA System Overview

First let us characterize the received signal of the users in a TRDMA downlink system. Suppose that there are N users in the system and all users use the same backoff factor D . $X_i[m]$ is the transmitted symbols to user i , which is assumed to be i.i.d. with unit power. Based on the system structure in Fig. 4.1, the transmit signal of the AP can be expressed as

$$s[m] = \sum_i \sum_l \sqrt{p_i} \mathbf{g}_i[m-l] X_i^{[D]}[l], \quad (4.1)$$

where $X_i^{[D]}$ represents the upsampled version of the symbols to user i by D , p_i is the allocated transmit power and \mathbf{g}_i denotes the designed transmitting waveform with unit power for user i . User i receives the signal and downsamples the signal for detection, and the downsampled signal can be expressed as

$$\begin{aligned}
Y_i[m] &= \sum_{j=1}^N \sum_l \sqrt{G_j p_j} X_j[l](\mathbf{h}_i * \mathbf{g}_j)[mD - lD] + n_i[m] \\
&= \sqrt{G_i p_i} X_i[m](\mathbf{h}_i * \mathbf{g}_i)[L - 1] + \sqrt{G_i p_i} \sum_{l=0, l \neq \frac{L-1}{D}}^{\frac{2L-2}{D}} X_i[m - l](\mathbf{h}_i * \mathbf{g}_i)[Dl] \quad (4.2) \\
&\quad + \sum_{j \neq i} \sqrt{G_i p_j} \sum_{l=0}^{\frac{2L-2}{D}} X_j[m - l](\mathbf{h}_i * \mathbf{g}_j)[Dl] + n_i[m],
\end{aligned}$$

where \mathbf{h}_i is the channel from AP to user i with unit power. L is the length of \mathbf{h}_i , which depends on the delay spread of the environment and the utilized bandwidth of the system. With our measurement using TR system prototype with 125 MHz bandwidth, we observe about 10 significant CIR taps and the total channel length L is about 30. For notation brevity, we assume that $L - 1$ is an integer multiple of the backoff factor D . G_i is the path gain from the AP to user i . Note that the \mathbf{h}_i is unit power and the channel power is absorbed into G_i . n_i is the receiving noise of user i and is assumed to be an i.i.d. complex Gaussian r.v. with power σ_i^2 . In (4.2), the first term represents the intended signal for user i ; the second term is the ISI; the third term is the IUI and the last term is the receiving noise.

4.3.2 Normalized Interference Matrix Calculation

Let us characterize the interference between the users based on the unit power channel \mathbf{h}_i and the waveforms \mathbf{g}_i . The $(i, j)^{th}$ entry $\mathbf{Z}_{i,j}$ of the normalized interference matrix \mathbf{Z} refers to the interference from user j to user i . Therefore, $\mathbf{Z}_{i,j}$ is determined by the channel \mathbf{h}_i from the AP to the user i and the waveform \mathbf{g}_j used to transmit to user j . $\mathbf{Z}_{i,j}$ is calculated using unit power \mathbf{h}_i and unit power \mathbf{g}_j , and

therefore the name normalized interference matrix. We separate p_j in the calculation of $\mathbf{Z}_{i,j}$ because the power allocation and the waveforms are not necessarily designed together and the separation expands the occasions where the scheme is applicable. Based on (4.2), the normalized interference between users can therefore be represented as

$$\mathbf{Z}_{i,j} = \sum_{l=0}^{\frac{2L-2}{D}} |(\mathbf{h}_i * \mathbf{g}_j)[Dl]|^2, \quad (4.3)$$

$$\mathbf{Z}_{i,i} = \sum_{\substack{l=0 \\ l \neq \frac{L-1}{D}}}^{\frac{2L-2}{D}} |(\mathbf{h}_i * \mathbf{g}_i)[Dl]|^2, \quad (4.4)$$

where (4.3) and (4.4) are the IUI and ISI for user i , respectively. On the other hand, the IUI for the massive MIMO system can be calculated as

$$\mathbf{Z}_{i,j} = |(\mathbf{h}_i^M)^T \mathbf{g}_j^M|^2, \quad (4.5)$$

there is no ISI in the massive MIMO system due to the assumption of limited subcarrier granularity and a single tap channel is observed.

4.3.3 Scheduler Objective

Let us first formulate the scheduler objective and the constraints. Suppose that the physical layer provides the scheduler with the normalized interference matrix \mathbf{Z} between users, the allocated power \mathbf{p} and the path gain G_i between the AP and user i . The scheduler gathers the transmission rate requirements R_i from the application layer for proper operation if user i is selected to transmit. For a specific transmission

rate requirements R_i , we can obtain the corresponding minimum SINR requirement γ_i by the one to one mapping between rate and SINR. The scheduler maintains a set of weights w_i to indicate the relative importance of each user. Based on the collected information and requirement, the scheduler objective that maximizes the system weighted sum rate is formulated as

$$\begin{aligned}
& \underset{\mathbf{x}}{\text{maximize}} \quad \sum_i w_i x_i \log_2 \left(\frac{G_i p_i}{G_i \sum_j p_j \mathbf{Z}_{i,j} x_j + \sigma_i^2} + 1 \right) \\
& \text{subject to } x_i \in \{0, 1\}, \quad \sum_i p_i x_i \leq P_{max}, \\
& \quad \quad \quad \frac{G_i p_i x_i}{G_i \sum_j p_j \mathbf{Z}_{i,j} x_j + \sigma_i^2} \geq \gamma_i x_i, \forall i.
\end{aligned} \tag{4.6}$$

The first constraint requires the decision variables x_i to be binary, and $x_i = 1$ represents user i is selected to transmit. The second constraint requires that the sum of the transmitting power of the selected users to be no more than the maximum AP transmitting power. The third set of constraints correspond to the minimum SINR requirements γ_i that the selected users must meet, and therefore the selected users meet the minimum transmission rate requirement R_i .

4.3.4 Mixed Integer Optimization

Let us describe the optimization transformation here. By enumerating all possible \mathbf{x} vectors, we can find the optimal decision vector \mathbf{x}_{opt} that maximized the objective and meet all the SINR constraints. However, the complexity for complete enumeration grows exponentially with the number of users N and therefore enumeration is not feasible when the number of users grows big. In this section, we propose

a simple yet effective problem formulation that transforms the objective and the constraints into a MIQCQP problem.

One property for binary decision variables that is used in the optimization formulation is as follows,

$$x_i^2 = x_i, \quad \forall i. \quad (4.7)$$

This relationship helps convert some of the quadratic terms into linear terms in the system objective and the constraints.

We consider that the scheduler operates at the high SNR region where we omit the noise term σ_i^2 at the receiver and the plus 1 term in the logarithm function. Also, the path gain G_i cancels each other and the optimization objective becomes

$$\begin{aligned} & \underset{\mathbf{x}}{\text{maximize}} \quad \sum_i w_i x_i \log_2 \left(\frac{p_i}{\sum_j p_j \mathbf{Z}_{i,j} x_j} \right) \\ & \text{subject to } x_i \in \{0, 1\}, \quad \sum_i p_i x_i \leq P_{max} \\ & \frac{p_i x_i}{\sum_j p_j \mathbf{Z}_{i,j} x_j + \sigma_i^2 / G_i} \geq \gamma_i x_i, \forall i \end{aligned} \quad (4.8)$$

We decompose the objective function into two terms using characteristics of the logarithm function as the following

$$\begin{aligned} & \underset{\mathbf{x}}{\text{maximize}} \quad \sum_i w_i x_i \log_2 \left(\frac{p_i}{\sum_j p_j \mathbf{Z}_{i,j} x_j} \right) \\ & \equiv \underset{\mathbf{x}}{\text{maximize}} \quad \sum_i w_i x_i \ln p_i - \sum_i x_i w_i \ln \left(\sum_j p_j \mathbf{Z}_{i,j} x_j \right). \end{aligned} \quad (4.9)$$

Next, we linearize the second logarithm term using the Taylor expansion of logarithm at $x_0 = 1$ and use the constant term and the first order term. Note that the

Taylor expansion for logarithm function to the linear term is a global overestimator of the logarithm function.

Let \mathbf{p} , \mathbf{w} be the power and weight vector of length N of the users respectively.

The second term in (4.9) can be simplified as

$$\begin{aligned} \sum_i w_i x_i \ln \left(\sum_j p_j \mathbf{Z}_{i,j} x_j \right) &\leq \sum_i w_i x_i \left(\sum_j p_j \mathbf{Z}_{i,j} x_j \right) - \mathbf{w}^T \mathbf{x} \\ &= \mathbf{x}^T (\text{diag}(\mathbf{w}) \mathbf{Z} \text{diag}(\mathbf{p})) \mathbf{x} - \mathbf{w}^T \mathbf{x}, \end{aligned} \quad (4.10)$$

where $\text{diag}(\cdot)$ operation generates a diagonal matrix using the elements in the vector. The inequality comes from the upper bound of Taylor expansion of the natural logarithm to the linear term. Define $\mathbf{A} = \text{diag}(\mathbf{w}) \mathbf{Z} \text{diag}(\mathbf{p})$ and \circ as the Hadamard product of two vectors. The objective function can be represented as

$$\sum_i w_i x_i \ln \left(\frac{p_i}{\sum_j p_j \mathbf{Z}_{i,j} x_j} \right) \geq (\ln(\mathbf{p}) \circ \mathbf{w})^T \mathbf{x} - \mathbf{x}^T \mathbf{A} \mathbf{x} + \mathbf{w}^T \mathbf{x} \quad (4.11a)$$

$$= (\ln(\mathbf{p}) \circ \mathbf{w} + \mathbf{w})^T \mathbf{x} - \frac{1}{2} \mathbf{x}^T (\mathbf{A} + \mathbf{A}^T) \mathbf{x}, \quad (4.11b)$$

where (4.11a) follows the property of Taylor expansion. The original objective function is transformed into (4.11b). However, it is not guaranteed that the optimal vector \mathbf{x}_{opt} for (4.9) and (4.11b) are the same.

Define \mathbf{I}_N as an identity matrix of size N and $\mathbf{1}$ be an all 1 vector of corresponding size, we add $\frac{c}{2} \mathbf{x}^T \mathbf{I}_N \mathbf{x}$ and subtract $\frac{c}{2} \mathbf{1}^T \mathbf{x}$ which have the same value by the property in (4.7), where c is a constant larger than the smallest eigenvalue of $\mathbf{A} + \mathbf{A}^T$. Since the same value is added and subtracted in the objective, it does

not change the objective value nor the feasible set. The reason for this redundancy will be discussed in Sec.4.3.5. Define $\mathbf{Q} = \mathbf{A} + \mathbf{A}^T + c\mathbf{I}_N$, we arrive at the final formulation as

$$\begin{aligned}
& \underset{\mathbf{x}}{\text{maximize}} (\ln(\mathbf{p}) \circ \mathbf{w} + \mathbf{w})^T \mathbf{x} - \frac{1}{2} \mathbf{x}^T (\mathbf{A} + \mathbf{A}^T) \mathbf{x} \\
& \equiv \underset{\mathbf{x}}{\text{minimize}} \frac{1}{2} \mathbf{x}^T (\mathbf{A} + \mathbf{A}^T + c\mathbf{I}_N) \mathbf{x} - (\ln(\mathbf{p}) \circ \mathbf{w} + \mathbf{w} + \frac{c}{2} \mathbf{1})^T \mathbf{x} \quad (4.12) \\
& \equiv \underset{\mathbf{x}}{\text{minimize}} \frac{1}{2} \mathbf{x}^T \mathbf{Q} \mathbf{x} - (\ln(\mathbf{p}) \circ \mathbf{w} + \mathbf{w} + \frac{c}{2} \mathbf{1})^T \mathbf{x}.
\end{aligned}$$

The second constraint can be written as

$$\mathbf{p}^T \mathbf{x} \leq P_{max} \quad (4.13)$$

For the third constraint, we have the minimum SINR constraint for user i as,

$$\frac{p_i x_i}{\sum_j p_j \mathbf{Z}_{i,j} x_j + \sigma_i^2 / G_i} \geq \gamma_i x_i \quad (4.14a)$$

$$\equiv x_i \sum_j p_j \mathbf{Z}_{i,j} x_j + \left(\frac{\sigma_i^2}{G_i} - \frac{p_i}{\gamma_i} \right) x_i \leq 0, \quad (4.14b)$$

Let $\mathbf{0}_{n,m}$ be a n by m all zero matrix. Define B_i as an all zero matrix with i th row to be the Hadamard product of \mathbf{z}_i , the i th row of \mathbf{Z} , and the transpose of the power allocation vector \mathbf{p} as follows

$$B_i = \begin{bmatrix} \mathbf{0}_{i-1,N} \\ \mathbf{z}_i \circ \mathbf{p}^T \\ \mathbf{0}_{N-i,N} \end{bmatrix}. \quad (4.15)$$

Define \mathbf{q}_i as an all zero vector of length N , except for the i th component being $\sigma^2/G_i - p_i/\gamma_i$,

$$\mathbf{q}_i = \begin{bmatrix} \mathbf{0}_{i-1,1} \\ \frac{\sigma^2}{G_i} - \frac{p_i}{\gamma_i} \\ \mathbf{0}_{N-i,1} \end{bmatrix}. \quad (4.16)$$

Then the constraint can be represented as

$$\begin{aligned} & \mathbf{x}^T \mathbf{B}_i \mathbf{x} + \mathbf{q}_i^T \mathbf{x} \leq 0, \quad \forall i \\ & \equiv \frac{1}{2} \mathbf{x}^T (\mathbf{B}_i + \mathbf{B}_i^T + c_i \mathbf{I}_N) \mathbf{x} + (\mathbf{q}_i^T - \frac{c_i}{2} \mathbf{1}) \mathbf{x} \leq 0, \quad \forall i, \\ & \equiv \frac{1}{2} \mathbf{x}^T \mathbf{Q}_i \mathbf{x} + (\mathbf{q}_i^T - \frac{c_i}{2} \mathbf{1}) \mathbf{x} \leq 0, \quad \forall i \end{aligned} \quad (4.17)$$

where $\mathbf{Q}_i = \mathbf{B}_i + \mathbf{B}_i^T + c_i \mathbf{I}_N$. c_i is a constant that is larger than the minimum eigenvalue of $\mathbf{B}_i + \mathbf{B}_i^T$.

Based on the above transformation, the whole optimization problem is formulated as

$$\begin{aligned} & \underset{\mathbf{x}}{\text{minimize}} \quad \frac{1}{2} \mathbf{x}^T \mathbf{Q} \mathbf{x} - (\ln(\mathbf{p}) \circ \mathbf{w} + \mathbf{w} + \frac{c}{2} \mathbf{1})^T \mathbf{x} \\ & \text{subject to } x_i \in \{0, 1\}, \quad \mathbf{p}^T \mathbf{x} \leq P_{max} \end{aligned} \quad (4.18)$$

$$\frac{1}{2} \mathbf{x}^T \mathbf{Q}_i \mathbf{x} + (\mathbf{q}_i^T - \frac{c_i}{2} \mathbf{1}) \mathbf{x} \leq 0, \quad \forall i,$$

which is an MIQCQP problem if and only if \mathbf{Q} and \mathbf{Q}_i s are positive semidefinite.

4.3.5 Positive Semidefiniteness of \mathbf{Q} and \mathbf{Q}_i

To ensure the transformed optimization problem to be an MIQCQP problem, we need to ensure \mathbf{Q} and \mathbf{Q}_i are all positive semidefinite. We first introduce the Weyl theorem [22] which states as follows.

Theorem 1 *Let \mathbf{U} , \mathbf{V} be Hermitian matrices of size N and let the eigenvalues $\lambda_i(\mathbf{U})$, $\lambda_i(\mathbf{V})$, and $\lambda_i(\mathbf{U}+\mathbf{V})$ be arranged in non-decreasing order. For $k = 1, 2, \dots, N$, we have*

$$\lambda_k(\mathbf{U}) + \lambda_1(\mathbf{V}) \leq \lambda_k(\mathbf{U} + \mathbf{V}) \leq \lambda_k(\mathbf{U}) + \lambda_n(\mathbf{V}) \quad (4.19)$$

Take \mathbf{U} as $\mathbf{A} + \mathbf{A}^T$ and \mathbf{V} as $c\mathbf{I}_N$. It is clear that if $c \geq \lambda_1(\mathbf{A} + \mathbf{A}^T)$ then \mathbf{Q} will be positive semidefinite. The same also applies to \mathbf{Q}_i and the constants c_i for the constraints.

The calculation for the eigenvalue for both the objective function and each of the constraints might seem time consuming. Nevertheless, we can simply use a predefined constant rather than calculating the eigenvalue for each optimization problem. In our simulation, simply choosing $c = c_i = 1$ is sufficient to ensure a valid MIQCQP formulation.

4.3.6 Extension to Multi-Cell Scenarios

We propose an scheduler based on the MIQCQP formulation in a downlink, single-cell setting in previous sections. The same formulation methodology can be applied to downlink cooperative multipoint (CoMP) scenarios with changes in the definition of variables and in the derivation of the normalized interference matrix \mathbf{Z} . Let us consider a downlink scheduler in a multi-cell network with C full frequency-reusing and synchronized cells. Suppose that N_k users are in cell $k, k = 1, \dots, C$, and there is inter-cell interference (ICI) due to full frequency reuse among cells.

To distinguish the users in different cells, we use superscript to indicate the index of the cell, and use subscript to indicate the user in a specific cell. Define $\mathbf{h}_i^{k,l}$ as the normalized CIR from cell l to user i in cell k and define \mathbf{g}_j^l as the transmitting waveform assigned to user j in cell l . Define $G_i^{k,l}$ as the path gain from cell l to the user i in cell k . Suppose all users in all cells use the same backoff factor D , then the downsampled received signal for user i in cell k can be expressed as

$$\begin{aligned}
Y_i^k[s] &= \sum_{c=1}^C \sum_{u=1}^{N_c} \sum_t \sqrt{G_i^{k,c} p_u^c} X_u^c[t] (h_i^{k,c} * g_u^c)[sD - tD] + n_i^k[s] \\
&= \sqrt{G_i^{k,k} p_i^k} X_i^k[s] (h_i^{k,k} * g_i^k)[L-1] + \sqrt{G_i^{k,k} p_i^k} \sum_{t=0, t \neq \frac{L-1}{D}}^{\frac{2L-2}{D}} X_i^k[s-t] (h_i^{k,k} * g_i^k)[Dt] \\
&\quad + \sum_{j \neq i} \sqrt{G_i^{k,k} p_j^k} \sum_{t=0}^{\frac{2L-2}{D}} X_j^k[s-t] (h_i^{k,k} * g_j^k)[Dt] \\
&\quad + \sum_{c=1, c \neq k}^C \sum_j \sqrt{G_i^{k,c} p_j^c} \sum_{t=0}^{\frac{2L-2}{D}} X_j^c[s-t] (h_i^{k,c} * g_j^c)[Dt] + n_i^k[s],
\end{aligned} \tag{4.20}$$

where the first term is the received signal, the second term the ISI, the third term the IUI, the fourth term is the ICI, and the last term is the receiving noise.

Let $\mathbf{Z}^{k,k}$ denote the N_k by N_k normalized interference matrix within cell k as defined in Sec.4.3.2. Let $\mathbf{Z}^{k,l}$ be the N_k by N_l ICI matrix. $\mathbf{Z}_{i,j}^{k,l}$, the $(i, j)^{th}$ term of $\mathbf{Z}^{k,l}$, represents the ICI to the user i in cell k due to the transmitted signal to user j in cell l . $\mathbf{z}_{i,j}^{k,l}$ is defined as

$$\mathbf{z}_{i,j}^{k,l} = \sum_{t=0}^{\frac{2L-2}{D}} \frac{G_i^{k,l}}{G_i^{k,k}} \left| (\mathbf{h}_i^{k,l} * \mathbf{g}_j^l)[Dt] \right|^2, \tag{4.21}$$

where $G_i^{k,k}$ in the denominator is to cancel the same term later in the formulation.

We can define the normalized interference matrix $\tilde{\mathbf{Z}}$ in the multi-cell scenario as

$$\tilde{\mathbf{Z}} = \begin{bmatrix} \mathbf{Z}^{1,1} & \mathbf{Z}^{1,2} & \dots & \mathbf{Z}^{1,C} \\ \mathbf{Z}^{2,1} & \mathbf{Z}^{2,2} & \dots & \mathbf{Z}^{2,C} \\ \vdots & \vdots & \ddots & \vdots \\ \mathbf{Z}^{C,1} & \mathbf{Z}^{C,2} & \dots & \mathbf{Z}^{C,C} \end{bmatrix}. \quad (4.22)$$

Let $\tilde{N} = \sum_{k=1}^C N_k$ be the total number of users in all cells, and we define the new decision variable vector of length \tilde{N} as $\tilde{\mathbf{x}} = [\mathbf{x}_1^T \quad \mathbf{x}_2^T \quad \dots \quad \mathbf{x}_C^T]^T$, and the new power vector of length \tilde{N} as $\tilde{\mathbf{p}} = [\mathbf{p}_1^T \quad \mathbf{p}_2^T \quad \dots \quad \mathbf{p}_C^T]^T$. The total interference \mathcal{I}_i^k including ISI, IUI and ICI to user i in cell k is $\left(G_i^{k,k} \tilde{\mathbf{Z}} \text{diag}(\tilde{\mathbf{p}}) \tilde{\mathbf{x}} \right) [\sum_{c=1}^{k-1} N_c + i]$, where the term in (\cdot) is a vector of length \tilde{N} , and the operator $[\cdot]$ takes out the corresponding element in the vector.

The weighted sum rate maximization in (4.6) can be reformulated using the newly defined variables and interference matrix as

$$\begin{aligned} & \underset{\tilde{\mathbf{x}}}{\text{maximize}} \quad \sum_k \sum_i w_i^k x_i^k \log_2 \left(\frac{G_i^{k,k} p_i^k}{\left(G_i^{k,k} \tilde{\mathbf{Z}} \text{diag}(\tilde{\mathbf{p}}) \tilde{\mathbf{x}} \right) [\sum_{c=1}^{k-1} N_c + i] + (\sigma_i^k)^2} + 1 \right) \\ & \text{subject to } x_i^k \in \{0, 1\}, \forall i, k, \quad \sum_i p_i^k x_i^k \leq P_{max}^k, \forall k, \\ & \quad \frac{G_i^{k,k} p_i^k x_i^k}{\left(G_i^{k,k} \tilde{\mathbf{Z}} \text{diag}(\tilde{\mathbf{p}}) \tilde{\mathbf{x}} \right) [\sum_{c=1}^{k-1} N_c + i] + (\sigma_i^k)^2} \geq \gamma_i^k x_i^k, \quad \forall i, k, \end{aligned} \quad (4.23)$$

where user i in cell k has its own corresponding weight w_i^k , SINR requirements γ_i^k , and receiving noise $(\sigma_i^k)^2$. The same procedure follows to transform the optimization

problem into the MIQCQP formulation. In the CoMP setting, it is assumed that the scheduler has the full knowledge of the path gain, channels and waveforms of the system. If the full knowledge of the system is too expensive to obtain, some of the components can be approximated and the MIQCQP formulation still applies.

4.4 Impact of Imperfect Channel Information

In the previous Section, we assume that the CIR information provided by the physical layer to be perfect. However, the CIR information provided by the physical layer is subject to receiving noise. Mismatch between the true and the estimated channel causes worse energy focusing in the 5G system, which results in a lower SINR in communication. Moreover, the mismatch also degrades the scheduler performance by noisy physical layer parameter inputs.

To investigate the impact of imperfect channel information, we start from analyzing the channel estimation error of the physical layer. There are existing literature on the distribution of the channel estimation error for the massive MIMO system [40], but there is no existing analysis or models on the channel estimation error on the TR system. Therefore, we first analyze a Golay sequence based channel estimation scheme for TR system proposed in [36] and analyze its impact on the accuracy of scheduler parameter inputs.

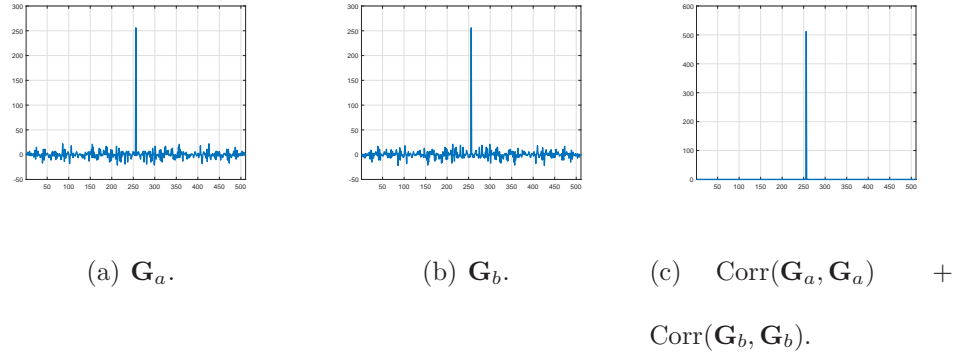


Figure 4.3: An example of Golay sequence.

4.4.1 Golay Sequence Based Channel Estimation

The Golay complementary sequence is first proposed in [17], which suggested a set of complementary sequence pairs \mathbf{G}_a and \mathbf{G}_b of the same length L_G . The correlation of \mathbf{G}_a with itself, i.e. $\text{Corr}(\mathbf{G}_a, \mathbf{G}_a)$ has a prominent peak but noisy sidelobes. However, $\text{Corr}(\mathbf{G}_a, \mathbf{G}_a) + \text{Corr}(\mathbf{G}_b, \mathbf{G}_b)$ produces a single maximum peak with no sidelobes. This prominent peak is useful in channel estimation because a clean copy of channel estimation can be obtained at the peak without the interference from the sidelobes.

Generation of \mathbf{G}_a and \mathbf{G}_b is based on two different sequences D_n and W_n of length n , and the length of the generated Golay sequence is $L_G = 2^n$. Fig. 4.3 shows an example of \mathbf{G}_a and \mathbf{G}_b pair using randomly generated D_n and W_n with $L_G = 256$, and $\text{Corr}(\mathbf{G}_a, \mathbf{G}_a) + \text{Corr}(\mathbf{G}_b, \mathbf{G}_b)$ shows a clear peak with no sidelobes. Please note that the amplitude of the peak is $2L_G$ and the length of the zero at the two sides of the peak is $L_G - 1$.

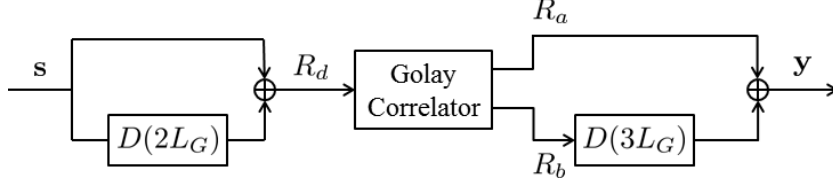


Figure 4.4: Diagram for Golay based channel estimation.

4.4.2 Channel Estimation via Golay Sequence

A channel estimation scheme using a $8L_G$ by 1 probing sequence ϕ is proposed in [36], which is composed of the corresponding pair of Golay sequences $\mathbf{G}_a, \mathbf{G}_b$ as

$$\phi = [\mathbf{G}_a^T \quad \mathbf{G}_b^T \quad -\mathbf{G}_a^T \quad \mathbf{G}_b^T \quad \mathbf{G}_a^T \quad -\mathbf{G}_b^T \quad \mathbf{G}_a^T \quad \mathbf{G}_b^T]^T. \quad (4.24)$$

Fig. 4.4 shows the block diagram of the channel estimation. The transmitter transmits the channel estimation sequence ϕ and the receiver receives the $L+8L_G-1$ by 1 signal $\mathbf{s} = \phi * \mathbf{h} + \mathbf{n}$, where L is the length of \mathbf{h} . We assume \mathbf{n} is AWGN with zero mean and variance σ^2 .

The received signal \mathbf{s} is divided into two branches. One branch goes through a delay of $2L_G$ and is summed with the other branch as \mathbf{R}_d .

$$\mathbf{R}_d = \left(\begin{bmatrix} \mathbf{I}_L \\ \mathbf{0}_{2L_G, L} \end{bmatrix} + \begin{bmatrix} \mathbf{0}_{2L_G, L} \\ \mathbf{I}_L \end{bmatrix} \right) \mathbf{s}. \quad (4.25)$$

We calculate the correlation of \mathbf{R}_d with \mathbf{G}_a and \mathbf{G}_b using the Golay correlator block, which produces two branches \mathbf{R}_a and \mathbf{R}_b , respectively. Define C_a and C_b as the $L+3L_G-1$ by $L+2L_G$ convolution matrix constructed by the time reversed version of \mathbf{G}_a and \mathbf{G}_b , and the outputs of the Golay correlator can be expressed as

$\mathbf{R}_a = C_a \mathbf{R}_d$ and $\mathbf{R}_b = C_b \mathbf{R}_d$. \mathbf{R}_b is delayed by $3L_G$ to summed with \mathbf{R}_a in order to produce the final channel estimation result. Therefore, the whole estimation block can be expressed as

$$\begin{aligned} \mathbf{y} &= \begin{bmatrix} \mathbf{I}_{L+3L_G-1} \\ \mathbf{0}_{2L_G, L+3L_G-1} \end{bmatrix} C_a \mathbf{R}_d + \begin{bmatrix} \mathbf{0}_{2L_G, L+3L_G-1} \\ \mathbf{I}_{L+2L_G-1} \end{bmatrix} C_b \mathbf{R}_d \\ &= T(\phi * \mathbf{h} + \mathbf{n}) = \begin{bmatrix} T_1 \\ \Phi \\ T_2 \end{bmatrix} (\phi * \mathbf{h} + \mathbf{n}). \end{aligned} \quad (4.26)$$

The matrix T is the total transfer function from the estimation block input \mathbf{s} to the block output, and it is separated into three parts T_1 , Φ , and T_2 by the rows. T_1 and T_2 represent the noisy part of the channel estimation scheme which is the sidelobes of the correlation of G_a and G_b , and these two parts are of no interest in channel estimation. Φ is the $7L_G$ -th to the $8L_G$ -th rows that correspond to the clean peak of the correlation of the Golay sequences without sidelobes, as shown in Fig. 4.3(c). Φ is a matrix that is determined by the Golay sequence pair, and each row of Φ has exact $4L_G$ none zeros entries with amplitude 1.

The channel estimation $\hat{\mathbf{h}}$ of length $L_G + 1$ can therefore be represented as

$$\hat{\mathbf{h}} = \Phi(\phi * \mathbf{h} + \mathbf{n}) = 4L_G \mathbf{h}' + \Phi \mathbf{n} = 4L_G \mathbf{h}' + \mathbf{n}_e, \quad (4.27)$$

where \mathbf{h}' is of length $L_G + 1$ which is formed by zero-padding \mathbf{h} to match the matrix dimension, and \mathbf{n}_e is the channel estimation error due to the received noise \mathbf{n} at the receiver.

4.4.3 Channel Estimation Error Analysis

We investigate the mean and variance of \mathbf{n}_e to show the effect of \mathbf{n} and L_G on the quality of channel estimation. By the assumption that \mathbf{n} is AWGN with zero mean and variance σ^2 , the mean of estimation error \mathbf{n}_e is also zero. The covariance of the channel estimation error \mathbf{n}_e is $\Phi\text{Cov}(\mathbf{n})\Phi^H$. It is assumed that \mathbf{n} is i.i.d. AWGN with variance σ^2 , and therefore the covariance of \mathbf{n}_e is $\sigma^2\Phi\Phi^H$.

To give an example of the correlation of \mathbf{n}_e , we randomly generate a Golay sequence pair with $L_G = 256$. Fig. 4.5 is the correlation of \mathbf{n}_e with \mathbf{n} to be i.i.d. Gaussian with unit σ^2 , namely $\Phi\Phi^H$. The prominent diagonal components have value $4L_G$ and each element of the diagonal is the noise variance σ_e^2 of \mathbf{n}_e . The off-diagonal components have extremely low value, which shows that different components of \mathbf{n}_e are almost uncorrelated. Therefore, the channel estimation errors \mathbf{n}_e on each tap of the estimated channel \mathbf{h}' are nearly uncorrelated, which is nearly independent due to the assumption that \mathbf{n} is i.i.d. AWGN.

4.4.4 SNR Enhancement of Golay Sequence Based Channel Estimation

The Golay sequence based channel estimation scheme increases the SNR of the channel estimation. Suppose that the SNR at the receiver is P/σ^2 where P and σ^2 are the power of the received signal \mathbf{s} and the noise \mathbf{n} , respectively. The channel estimation output has a peak with amplitude $4L_G$, by which the power of the channel estimation is $16L_G^2P$. Each row of Φ consists of exactly $4L_G$ none zero

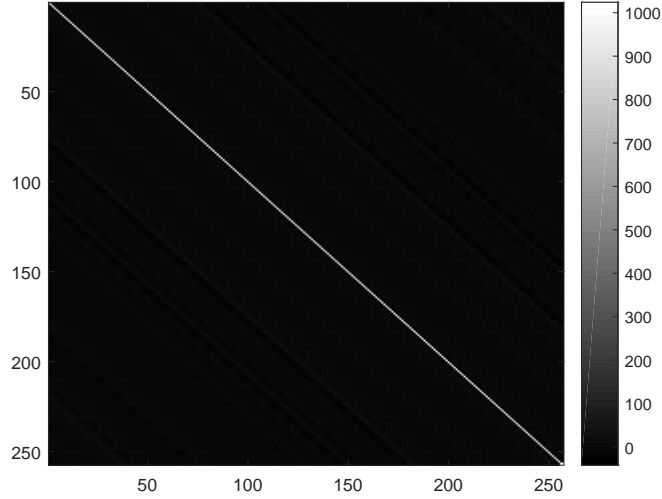


Figure 4.5: An example of $\Phi\Phi^H$.

elements with amplitude 1, therefore σ_e^2 is $4L_G\sigma^2$. As a result, the SNR at the channel estimation output is boosted for $4L_G$ times.

The channel estimate using the proposed Golay channel estimation scheme is contaminated with noise which has zero mean and variance $4L_G\sigma^2$. Therefore, the length of the Golay sequence affects the SNR boost at the estimation output, and the TR system can adapt the Golay sequence length L_G based on the system requirement on channel estimation. More importantly, \mathbf{n}_e on each tap of the channel estimation are nearly independent, which is the result from the structure of the transfer function Φ of the Golay channel estimation scheme.

The channel estimation error for the massive MIMO system is investigated in [40]. The channel estimation errors on the links from the base station to a user are i.i.d. complex Gaussian with zero mean and same variance which is determined by the shadowing effect of the user. The channel estimation error of the TR system

and the massive MIMO system share similarity in that the estimation error of the channel are i.i.d variables with zero mean and the same variance. This similarity in channel estimation error therefore extends the discussion and simulation results on the scheduler performance degradation to massive MIMO counterparts.

4.4.5 Effect on the Scheduler Parameter

The proposed scheduler algorithm generates the transmission profile for the users based on the estimated channel and the assigned power from the physical layer. Inaccurate channel estimation deteriorates the efficiency of the scheduling in the MAC layer, and it is desirable to investigate how the channel estimation error affects the input parameter of the proposed scheduler.

Based on the previous investigation of the channel estimation error, we model the estimated channel $\hat{\mathbf{h}}$ as

$$\hat{\mathbf{h}} = \mathbf{h} + \mathbf{n}_e, \quad (4.28)$$

where we assume that \mathbf{n}_e is i.i.d. complex Gaussian noise with zero mean and variance σ_e^2 . According to the optimization formulation of the scheduler in (4.6), channel estimation error \mathbf{n}_e affects the scheduler performance by affecting the calculation of the normalized interference matrix \mathbf{Z} . Define $\hat{\mathbf{Z}}$ as the normalized interference matrix obtained using the channel estimation $\hat{\mathbf{h}}$, and we calculate the expectation of $\hat{\mathbf{Z}}$ to show the impact of channel estimation error on the normalized interference matrix \mathbf{Z} .

$$\begin{aligned}
\mathbb{E} \left[\hat{\mathbf{Z}}_{i,j} \right] &= \mathbb{E} \left[\sum_{l=0}^{\frac{2L-2}{D}} \left| (\hat{\mathbf{h}}_i * \mathbf{g}_j)[Dl] \right|^2 \right] = \mathbb{E} \left[\sum_{l=0}^{\frac{2L-2}{D}} \left| ((\mathbf{h}_i + \mathbf{n}_e) * \mathbf{g}_j)[Dl] \right|^2 \right] \\
&= \begin{cases} \mathbf{Z}_{i,j} + \frac{\sigma^2}{4L_G} \left(\frac{L-1}{D} - 1 \right) + \frac{\sigma^2}{4L_G} \sum_{l=0}^{\frac{L-1}{D}} \left| \mathbf{g}_j[Dl] \right|^2 & , \text{if } i = j \\ \mathbf{Z}_{i,j} + \frac{\sigma^2}{4L_G} \left(\frac{L-1}{D} \right) + \frac{\sigma^2}{4L_G} \sum_{l=0}^{\frac{L-1}{D}} \left| \mathbf{g}_j[Dl] \right|^2 & , \text{if } i \neq j \end{cases} \quad (4.29) \\
&< \begin{cases} \mathbf{Z}_{i,j} + \frac{\sigma^2}{4L_G} \left(\frac{L-1}{D} \right) & , \text{if } i = j \\ \mathbf{Z}_{i,j} + \frac{\sigma^2}{4L_G} \left(\frac{L-1}{D} + 1 \right) & , \text{if } i \neq j \end{cases}
\end{aligned}$$

where the last inequality results from the normalized waveform \mathbf{g}_j and serves as an upper bound for $\mathbb{E} \left[\hat{\mathbf{Z}} \right]$.

The formula suggests that the error in the normalized interference matrix $\Delta \mathbf{Z} = \mathbb{E} \left[\hat{\mathbf{Z}}_{i,j} \right] - \mathbf{Z}_{i,j}$ relates to three factors, the backoff factor D , the channel length L , and the length of the Golay sequence L_G . A larger backoff factor not only reduces the IUI and ISI but also reduces the impact of the channel estimation error on the normalized interference matrix. The longer the channel length, the larger the IUI and ISI, thus the bigger $\Delta \mathbf{Z}$. The last factor is the Golay sequence length L_G , which affects the additive noise power at the channel estimation. The dependence of n_e on L_G gives the system the flexibility to adapt the length of Golay sequence to the users' SNR conditions.

4.5 Simulation Results

In this section, we evaluate the performance of the proposed scheduler algorithm from several aspects. First, we compare the time complexity of the proposed scheduler algorithm with that using enumeration. We also evaluate the scheduler performance under different physical layer structures. Then we investigate the impact of channel estimation error. We use the following model and system parameters. We generate \mathbf{h} of the TR system based on the channel model proposed in [20], and waveform \mathbf{g} is the time reversed and conjugated version of \mathbf{h} . For TR system, users are distributed randomly within a 20 meter by 20 meter area with the transmitter located at the center to simulate an indoor environment. For massive MIMO system, users are distributed randomly within a 300 meter by 300 meter area to simulate an outdoor environment. The transmitter is located at the center of the area in both cases. The path loss exponent is 3.5. The rate requirements for the users R_i are generated uniformly from the range of 1 Mbps to 2 Mbps. The weight vector \mathbf{w} is generated uniformly from 0 to 1. The power vector is generated from a uniform distribution from 0.1 to 0.3 for each user and P_{max} is set to 1. The SNR is 0 dB for each of the users, unless mentioned otherwise. The system bandwidth of the TR system is 125 MHz in the simulation. The simulation is repeated for 2000 channel realizations for each of the settings. Lastly, we select the Gurobi solver to solve the MIQCQP problem [18].

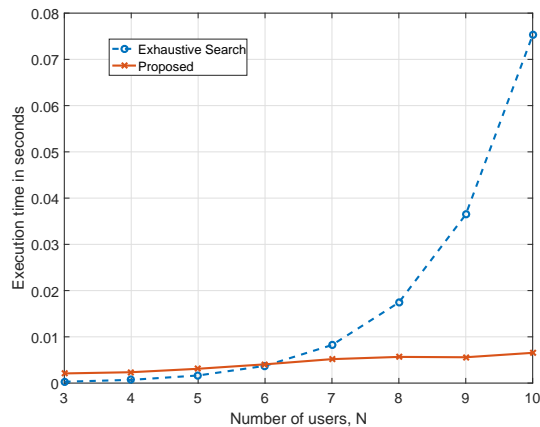


Figure 4.6: Run time comparison for different number of users.

4.5.1 Time Complexity

Time complexity is an important performance indication for scheduler that performs in real time with strict deadline. Moreover, the importance grows with the foreseeable sharp increase in the number of users in the system. Fig. 4.6 shows the comparison of the running time with number of users N ranging from 3 to 10 and $D = 4$. The proposed scheduler consumes more time than that of exhaustive search when the number of users are small due to the model setup, and shows an empirical $\mathcal{O}(N)$ complexity. Result shows $\mathcal{O}(2^N)$ complexity for exhaustive search and the execution time outpaces the proposed scheduler. The $\mathcal{O}(N)$ complexity makes the proposed scheduler suitable for application with strict deadline.

4.5.2 Scheduling Performance Comparison

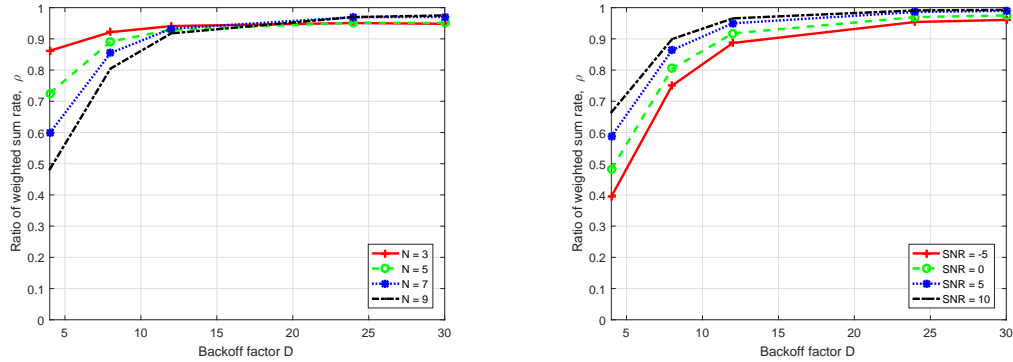
To evaluate the performance of the proposed scheduler, we compare the weighted sum rate of the proposed scheduler R_S with the weighted sum rate obtained by ex-

haustive search R_{opt} by calculating the average of the ratio $\rho = R_S/R_{opt}$. We chose the backoff factor $D = [4, 8, 12, 24, 30]$ and number of users $N = [3, 5, 7, 9]$. Fig. 4.7(a) shows the ρ with different N and D . For a small D , the deviation from optimality with large N comes from the errors at the linearization of the logarithm term around 1, because the actual sum is far from 1. However, when D increases, the entries of \mathbf{Z} becomes smaller and the error due to expansion at 1 gets smaller. For larger N , which is the targeted use case for the next generation system, ρ increases rapidly to above 0.9 in all cases where D is larger than 8.

To evaluate the performance of the proposed scheduler under different SNR conditions, we perform simulations where all users have the same SNR selected from $[-5, 0, 5, 10]$ dB. We simulate with different backoff factors $D = [4, 8, 12, 24, 30]$ and $N = 9$, and the result is presented in Fig. 4.7(b). In the low SNR region, the approximation in (4.8) is not as accurate and there is a gap between the performance of the proposed scheduler and that of exhaustive search. However, ρ increases over 0.9 when D is larger than 8 in most SNR cases.

The proposed scheduler separates the physical layer implementation, and the separation makes the scheduler suitable for different waveform design and power allocation algorithms. Fig. 4.8(a) shows ρ with a downlink system using the waveform design and power allocation proposed in [57]. The original uplink max-min SINR algorithm in [57] is modified using the uplink-downlink duality for downlink purpose. The figure shows a similar ρ as in Fig. 4.7(a), which shows that the proposed scheduler algorithm is versatile for different physical layer implementation.

We also evaluate the scheduler performance on the massive MIMO system.

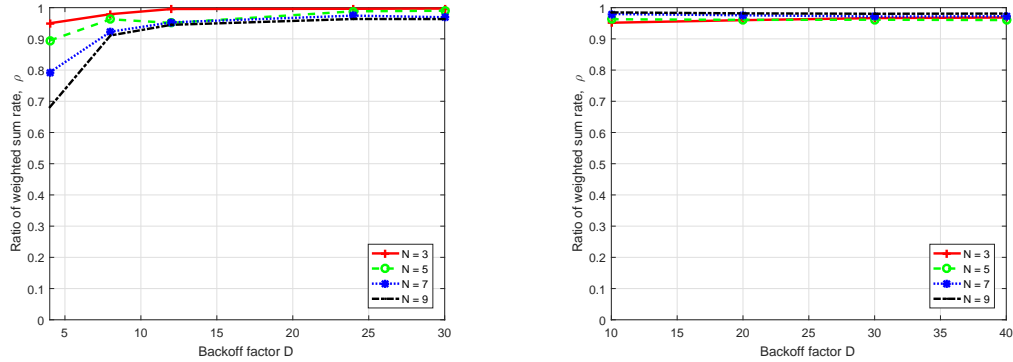


(a) Performance with different number of users. (b) Performance under different SNR conditions.

Figure 4.7: Performance of the proposed scheduler compared with exhaustive search result.

We assume flat fading channels, i.e. one tap channel, on each links of the massive MIMO system. Each link is modeled as a complex Gaussian random variable with zero mean and unit power as $CN(0, 1)$. The beamforming vector \mathbf{g}_i is selected as the maximum ratio combining (MRC) scheme, where \mathbf{g}_i is simply the complex conjugate of the channel link \mathbf{h}_i^* . We set the number of users $N = [3, 7, 10, 13]$ and the number of antennas $M = [10, 20, 30, 40]$ and simulate 2000 channel realizations. Fig. 4.8(b) shows ρ of the proposed scheduler and it is obvious that ρ approaches to 1 in all cases we simulated.

To evaluate the performance of the scheduler with a large number of users, we evaluate the scheduler performance with the number of users $N = [15, 20, 25, 30]$ and $D = [16, 20, 25]$. We compare the average weighted sum rate of the scheduler output with a first-come-first-serve system that tries to accommodate as much as users as possible given the users' requirements are satisfied. We simulate 4000



(a) Performance using waveform design algorithm proposed in [57]. (b) Performance on massive MIMO system.

Figure 4.8: Performance of the proposed scheduler with different physical layer implementations.

channel realizations for each set of N and D and Fig. 4.9 shows the results of the two schedulers. The result shows that the proposed scheduler outperforms the first-come-first-serve system in every setting by a large margin, showing the effectiveness of the scheduler with a large N . With a fixed D , the weighted sum rate increases with N and saturate when N is large. The SINR requirements of the users limits the achievable regions of the system and results in the weighted sum rate saturation at larger N . With a fixed N , the system weighted sum rate decrease with larger D because of less frequent transmission.

To evaluate the scheduler performance with existing schedulers, we compare the performance with the massive MIMO scheduler proposed in [11]. The authors proposed a pair-wise semi-orthogonal user selection (pair-wise SUS) scheduler that selects transmitting users with mutual channel correlations lower than a cut-off value

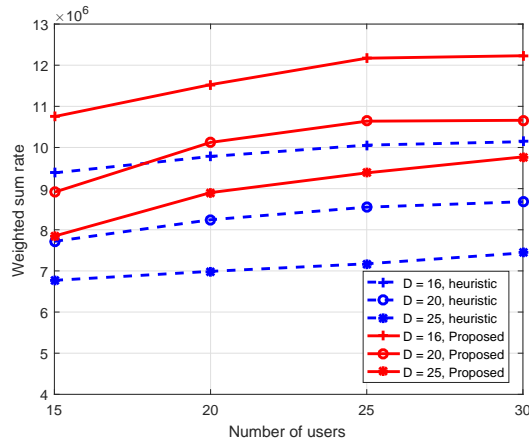
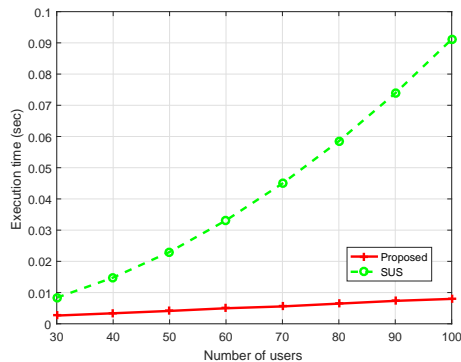


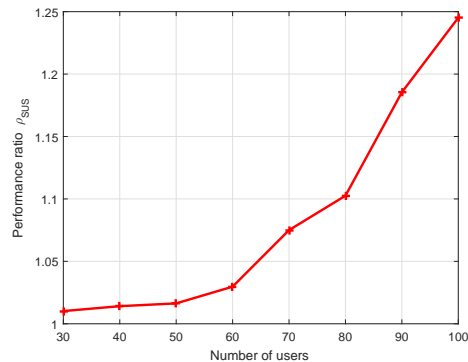
Figure 4.9: Performance of proposed scheduler compared with a first-come-first-serve system.

β_{min} . We select β_{min} to be 0.45 which shows the best performance across different number of antennas at the transmitter in [11]. We impose the rate constraints on the users selected by pair-wise SUS scheduler and remove users one by one until all users' rate constraints are satisfied. We simulate 150 antennas at the transmitter, and 30 to 100 users in the system. We assume that each user has the same weight and simulate 2000 channel realizations. The performance metric is measured by the complexity and the average ratio $\rho_{SUS} = R_S/R_{SUS}$ of the system sum rates between the proposed scheduler (R_S) and the pair-wise SUS scheduler (R_{SUS}).

Fig. 4.10(a) shows the mean execution time of the pair-wise SUS scheduler and the proposed scheduler. Simulation result shows that the proposed scheduler has $\mathcal{O}(N)$ complexity, while pair-wise SUS scheduler has $\mathcal{O}(N^2)$ complexity, where N is the number of users. The $\mathcal{O}(N^2)$ complexity of the pair-wise SUS scheduler is the result of the need to search through all pairs of users' channels to find the high correlated pairs and to remove one of them in the selected user set.



(a) Time complexity comparison.



(b) Performance ratio ρ_{SUS} .

Figure 4.10: Performance comparison between the proposed scheduler and the pair-wise SUS scheduler.

Fig. 4.10(b) shows the ρ_{SUS} of the pair-wise SUS scheduler and the proposed scheduler. Simulation shows that the proposed scheduler outperforms the pair-wise SUS scheduler in all cases, and ρ increases with the increase of users. The pair-wise SUS scheduler removes users with high channel correlation one-by-one, and therefore the selection process of the scheduler may reach a local optimum. On the other hand, the proposed scheduler selects users together, and therefore the global optimal value of the MIQCQP formulation can be reached.

4.5.3 Channel Estimation Error

To investigate the distribution of the channel estimation error, we simulate the estimation error of the Golay channel estimation block output as follows. We generate i.i.d. AWGN \mathbf{n} with zero mean and unit variance at the receiver input. We randomly generate 100 pairs of Golay sequence with length $L_G = [16, 32, 64, 128, 256]$.

L_G	16	32	64	128	256
$r_{i,j}$	0.187	0.145	0.0118	0.093	0.081

Table 4.1: Maximum absolute value of the off-diagonal components of the estimated channel estimation error correlation with different L_G .

For each pair of the Golay sequences, we generate 10000 realizations of \mathbf{n} and estimate the correlation coefficient of the channel estimation error at the output, i.e. the correlation of \mathbf{n}_e .

Table. 4.1 shows the maximum absolute value of the off-diagonal element of the estimated correlation $r_{i,j}, i \neq j$ of \mathbf{n}_e over all the 100 random realizations of the Golay sequence. With the increase of L_G , $\max(r_{i,j}), i \neq j$ decreases to less than 0.1 which indicates that the channel estimation error has low correlation value. This justifies our previous assumption that the channel estimation error on each tap of channel estimation at the output of the Golay based estimation block can be modeled as independent. Also, the Golay sequence in the simulation is generated via random realizations of D_n and W_n , and exhaustive search on D_n and W_n can further reduce $r_{i,j}$ if desirable.

We evaluate the effect of channel estimation error on the stability of the scheduler performance as the following. We assume the SNR at the receiver is 0dB and calculate the corresponding channel estimation noise power with different Golay sequence length L_G . Then we calculate \mathbf{Z} with the estimated channel $\hat{\mathbf{h}}_i$ and \mathbf{g}_j being the time-reversed and conjugated CIR. Then we calculate the ratio ρ_E between the

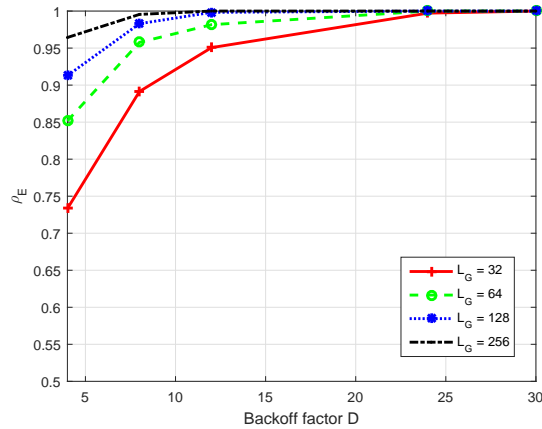


Figure 4.11: Performance ratio ρ_E between perfect channel R_S and channel estimation error R_E .

scheduler output with channel estimation error R_E and the scheduler output with perfect channel information R_S . We perform 2000 realizations and calculate the mean of ρ_E in all cases.

Fig. 4.11 shows the ratio ρ_E with $N = 9$, where the y axis runs from 0.5 to 1. A small L_G does affect the scheduler performance, but the performance reduction reduces with a larger L_G . Moreover, for the range where $D > 8$ which is a preferable operating point for $N = 9$, the reduction in performance is marginal. The result shows that the proposed scheduler is robust against channel estimation error and the system can adjust the Golay sequence length according to the SNR of the received signal.

4.6 Summary

In this chapter, we propose a novel scheduler for the 5G downlink system. The scheduler objective of maximizing system weighted throughput and the SINR constraints of the users are transformed into an MIQCQP problem. The proposed scheduler has a linear complexity compared to the exponential complexity of exhaustive search with slight performance reduction. Secondly, we investigate the impact of imperfect channel information and analyze a channel estimation scheme of TR system using Golay sequence pairs. The Golay sequence based channel estimation error has similar distribution as the channel estimation error of the MIMO system. The proposed scheduler is shown to be robust against channel estimation error and is versatile for different physical layer structures. The robustness, versatility, and the low time complexity make the proposed scheduler suitable for deployment in systems with a massive number of users and strict scheduling deadlines.

Chapter 5

Time Reversal Rate Adaptation

In previous chapter, we have developed scheduler for 5G communication systems by selecting a subset of users to transmit simultaneously. A proper selection of user decreases the interference and increases the system rate. Other than simply selects users for transmission, proper allocation of resources between users increases the system performance by proper allocation of mutual interference in the literature. For example, judicious allocation of transmitting powers and waveforms reduces the interuser interference (IUI) and increases the system performance. Power allocation has been proposed such as in [41, 51, 65] to manage the interference between users. Waveform design and beamforming take another approach by optimally designing the transmission waveform and/or the weights of the antennas to focus energy to the intended users with small energy leakage to the unintended ones [8, 24, 30, 35, 37, 45].

The power allocation scheme does not guarantee all the users in the system with a minimum power to maintain QoS. In the case when each of the user needs a minimum transmission energy to guarantee performance, it is possible that there is no solution to the power allocation scheme. On the other hand, the performance of waveform design cannot guarantee QoS for users when the number of users is large, and the performance is constrained by the actual physical environment, CIR

and/or number of antennas. To avoid the infeasibility and to mitigate the lowered performance in power allocation and waveform design, an algorithm that both selects a subset of users for transmission and judiciously allocates resource to the users to improve the overall system performance is greatly desirable.

The backoff factor D is the parameter in TR system that dictates the interval between consecutive transmissions and affects the total amount of transmitted information within a specific time span. The smaller the D is, the smaller the interval between the symbols in time and the higher transmission rate. However, a smaller D also results in larger interference from two different aspects. First, the smaller transmitting interval makes the concentrated energy by the spatial temporal focusing effect to overlap more on the time axis, which causes larger ISI. Second, the smaller transmitting interval causes larger IUI due to more energy leakage to unintended users via more frequent transmission. Backoff factor D has the double effect on the amount of interference and therefore it is beneficial to allocate D judiciously to users and maximize the TR system performance.

We propose a medium access control (MAC) backoff factor adaptation algorithm for the downlink time reversal division multiple access (TRDMA) system. The algorithm maximizes the system throughput by allocating the optimal D for a selected subset of users for transmission, and satisfies the QoS requirements of the selected users. The proposed backoff factor adaptation algorithm transforms the system objective and the QoS requirements of the users into an MIQCQP which can be solved efficiently. Next, since the set of allocated power and the waveforms provided by the physical layer is not optimal with the set of selected users and the

allocated backoff factors, we propose a joint power allocation and waveform design algorithm that ensures the minimum SINR constraints to be met for the selected users and the allocated backoff factors. With the two-step rate adaptation and waveform design, the system meets the minimum QoS requirement and increases system-wise performance.

We summarize this chapter as follows:

- We investigate the spatial temporal focusing effect of the TR system and illustrate how the backoff factor D affects the interference among users.
- We develop a rate adaptation algorithm that selects a subset of users and allocates optimal backoff factors for transmission. The optimization problem is transformed into a mixed integer quadratically constraint quadratic programming.
- We propose a joint power allocation and waveform design guaranteeing the minimum SINR requirement of the selected users. The proposed algorithm maintains the QoS requirement of the users and increases the system performance.

The chapter is organized as follows. A downlink TRDMA system is given in Sec.5.1. Then we give a simple illustration of the spatial temporal focusing effect, and how the IUI and ISI is affected by the backoff rate in Sec.5.2. The throughput maximization algorithm is formulated in Sec.5.3. Waveform design is detailed in Sec.5.4 and simulation results are given in Sec.5.5. Finally the conclusion is given in Sec.5.6.

5.1 System Overview

First we describe a downlink time reversal division multiple access (TRDMA) system as depicted in Fig.4.1, where we consider N users, or terminal devices (TD), are served. The access point (AP) first upsamples symbols $X_i[m]$ for user i using the corresponding backoff factors D_i . The upsampled symbols are encoded using the assigned waveforms \mathbf{g}_i for user i , and the AP transmits the summed signal using a single antenna. Users receive the signal and adjust the power using one tap gain, downsample the received signal with the corresponding backoff factor D_i and perform detection to estimate and recover the transmitted symbols.

Based on the system structure, the transmit signal of the AP can be expressed as

$$s[m] = \sum_i \sum_l \sqrt{p_i} g_i[m-l] X_i^{[D_i]}[l], \quad (5.1)$$

where $X_i^{[D_i]}$ represents the upsampled version of $X_i^{[D_i]}$ by D_i , p_i is the allocated transmit power and g_i denotes the designed transmitting waveform with unit power to user i . User i receives the signal and downsamples the signal for detection, and the downsampled signal can be expressed as

$$\begin{aligned}
Y_i[m] &= \sum_{j=1}^N \sum_l \sqrt{G_j p_j} X_j[l] (h_i * g_j)[mD_i - lD_j] + n_i[m] \\
&= \sqrt{G_i p_i} X_i[m] (h_i * g_i)[0] \\
&\quad + \sqrt{G_i p_i} \sum_{l=-\lfloor \frac{L-1}{D_i} \rfloor}^{\lfloor \frac{L-1}{D_i} \rfloor} X_i[m-l] (h_i * g_i)[D_i l] \\
&\quad + \sum_{j \neq i} \sqrt{G_j p_j} \sum_{l=-\lfloor \frac{L-1}{D_j} \rfloor}^{\lfloor \frac{L-1}{D_j} \rfloor} X_j[m-l] (h_i * g_j)[D_j l] + n_i[m],
\end{aligned} \tag{5.2}$$

where h_i and G_i are the channel impulse response (CIR) with unit power and the path gain from the AP to user i , respectively. Note that the CIR power is absorbed into the path gain variable. In (5.2), the first term represents the intended signal for TD i at time m ; the second term is the ISI; the third term is the IUI and the last term is the noise term.

Several resources can be optimally allocated and designed to increase the SINR in observing (5.2), such as the transmitting waveform \mathbf{g}_i , the power allocated to users p_i and the backoff factor D_i . For example, joint power and waveform design can increase the system performance by reducing the IUI and ISI in the TR system [58], [57]. (5.2) also suggests that the allocated backoff factors also affect the system performance by affecting the amount of interference in ISI and IUI. To see in detail how D_i s affect the interference, we introduce the energy focusing of the special spatial temporal focusing effect in TR system. Then we illustrate how the backoff factor affects the energy focusing distribution in time and space, and eventually the amount of IUI and ISI.

5.2 Spatial Temporal Focusing Effect

Wireless communication system transports energy and information from the transmitter to the receiver by utilizing the physical phenomenon of electromagnetic wave propagation. Channel statistics and characteristics of the communication system, such as the channel delay spread and the coherence distance, are obliged to the law of physics [49] and are determined by the bandwidth, the carrier frequency of the system, and the surrounding environment, etc. For example, the channel delay spread is defined as the span of time within which the observed channel contains significant energy. When the environment is more complex with compartments and occluding objects or when the transmitter and receiver are non-line-of-sight, the channel delay spread is generally longer because some of the electromagnetic waves arrives at the receiver later due to multiple reflections from the objects. The channel information in the channel delay spread records the arrival time of the reflected waves, providing detail information about the environment.

The coherence distance, another crucial channel statistics, is defined as the distance in which the observed channels do not significantly change and are considered to be highly correlated. Due to the high correlation, the transmitter can use the estimated channel for transmission and the receiver can still receive the signal power as long as the receiver is within the volume spanned by the coherence distance. Physic model shows that the coherence distance is determined by the half wavelength of the carrier frequency of the system. As a result, the larger the carrier frequency, the smaller the coherence distance, the smaller the ball within

which channel estimation can be reused, and the more frequently the system has to estimate the channel for communication.

Both the channel delay spread and coherence distance are important elements for the spatial temporal focusing effect in the TR system. Given a fixed channel delay spread, TR system utilizes a much larger bandwidth for transmission, and samples the CIRs more frequently compared to narrowband systems. In narrowband system, due to insufficient bandwidth, only two to three CIR taps can be observed, in which most of the information about the surrounding environment is lost. TR system observes massive number of CIR taps by sampling more frequently and preserves the information embedded in the CIR. In our measurement with TR prototype with 125 MHz bandwidth, we observe about 10 significant channel taps that contain most of the channel energy, and the total CIR length is 30.

With the large bandwidth and the detailed CIR information, TR system designs special transmitting waveforms such that the environment acts as a matched filter and all the transmitted signal adds up at the intended user coherently. The transmitted signal adds up randomly at unintended locations due to CIR mismatch with the environment. In narrowband system, we cannot observe the focusing effect because the environment information is smeared and therefore the transmitted signal cannot match with the environment to focus the energy. Moreover, the concentration of the energy is not only in temporal domain, but also in the spatial domain. The environment acts like the matched filter to concentrate the energy at the intended location, therefore the energy also concentrates at the vicinity within the coherent distance. The transmitted energy not only concentrates at the intended

user but also within the *volume* spanned by the coherent distance around the user.

In short, we can view the energy focusing of the TR system in two ways, either in the temporal or spatial domain. First, the large bandwidth enables the system to finely sample the location-specific CIRs, resulting in a massive number of channel taps. The finely sampled, massive number of channel taps match with the complex environment, such that the signal energy is maximized at the instant of sampling. We call this temporal focusing effect. Secondly, the location-specific CIRs concentrates the energy in the volume spanned by the coherent distance, and we call it spatial focusing effect.

To show the granularity of the spatial temporal focusing effect of the TR system, we collect CIRs in a 5cm by 5cm area of interest and evaluate the energy focusing within the area and across time. We use the TR prototype with 125 MHz bandwidth and carrier frequency at 5.4 GHz. we collect 300 CIRs with channel length $L = 30$ at each of the 5 millimeter grid points, which we collect a total of 121 grid points. The point of interest is at the center of the area, and we use the time-reversed and conjugated CIR as the transmit waveform \mathbf{g} . We calculate the received energy of $\mathbf{g} * \mathbf{h}[m]$, where \mathbf{h} is the CIRs collected at all the grid points in the area, and the maximum energy is normalized to 0 dB. Fig.5.1 shows the energy distribution near the location of interest at different time. We plot $m = 23, \dots, 37$, which is 7 samples before and after the energy focusing peak at $m = 30$, where each sample are 8 nanoseconds apart due to the 125 MHz bandwidth. The 15 figures are listed from left to right first, and then from top to bottom, which correspond to $m = 23, \dots, 37$ respectively.

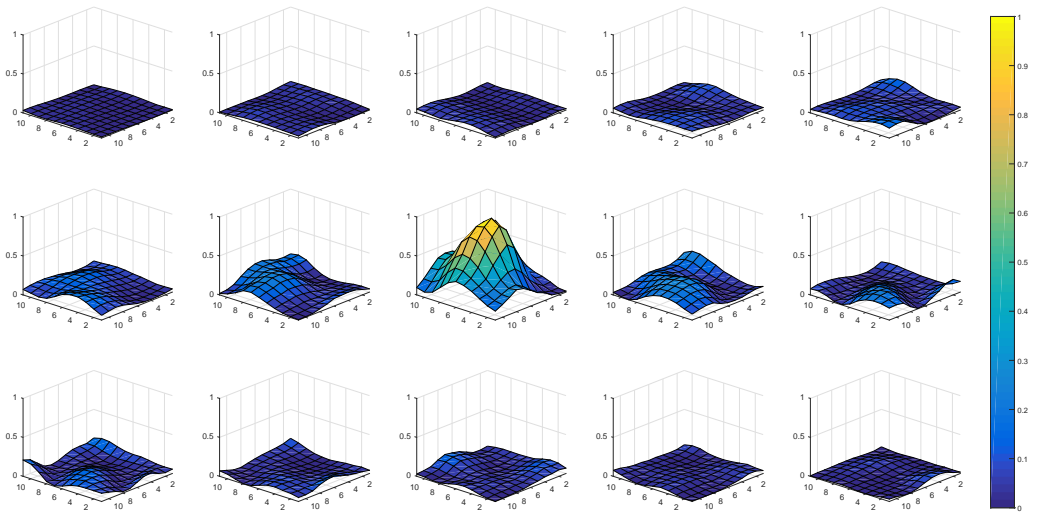


Figure 5.1: Energy distribution of TR system within the area of interest and across time. The figures are listed from the left to right first, and then top to bottom. The middle one the time instant with maximum energy focusing, which is $m = 30$. The energy are normalized such that the maximum energy received is 0dB.

We observe the energy distribution temporally from the sequence of figures. In the series of figures across time, the received energy is maximized at the sampling instant, i.e. at $m = 30$. There are also some ripples around $m = 30$, and this spread of transmitted energy around the focusing time is dictated by the indoor channel delay spread and the frequency of sampling. The indoor channel delay spread is about 30 to 50 nanoseconds at the 5.4GHz, which results in about 5 to 6 significant CIR taps in the 125 MHz TR prototype. The spread of energy is consistent with the focusing shown in the figure.

Secondly, at the center figure where $m = 30$, we can see energy concentrates at the vicinity of the point of interest. The energy concentration is the result of coherent distance and it is affected by the carrier frequency of the system. The channel correlation between two locations drops significantly if the separation of the locations are larger than half the carrier wavelength. The carrier frequency of the TR system is at 5.4 GHz with half wavelength to be about 2.7 centimeters, and we can see that the received energy is much less at the edge of the area of interest.

From the observation in both spatial and temporal domain, the spatial temporal focusing effect of the TR system is an energy ball that occurs within a certain volume and a certain time span. The energy ball's diameter on the spatial and temporal domains are determined by the surrounding environment and the system parameters. With each transmission, there is an energy ball forming and dissipating at the spatial temporal area of interest. It is to be noted that this spatial temporal energy ball exists in all the communication systems; however, only with the large bandwidth can the system observe distinctive CIRs with fine granularity and harvest

the energy concentration in both spatial and temporal domain.

The backoff factor D in TR system controls the interval between consecutive transmissions, and therefore determines how the energy balls overlap in time. With a larger D , a longer interval, the energy balls are farther apart in the temporal domain, which causes less ISI to following symbols. On the other hand, the larger D , the transmitter transmits less frequently to the intended user, and therefore less leaked interference to the unintended users farther than the coherent distance of the system. We show the effect of different D on both ISI and IUI in the following with simple examples.

5.2.1 Temporal Impact of Backoff Factor on Interference

Let us illustrate the effect of D via an example with only two users in the downlink TRDMA system. Suppose that there are two users in the TRDMA system and the transmitter transmits to both users with the same power. User 1 is located at the center of the interested area as in Fig. 5.1. User 2 is located outside of the interested area of user 1. We suppose that there is no noise at the receiver and focus on the signal to interference ratio (SIR). We plot out the SIR in Fig. 5.2 of user 1 with $D_2 = 8$ and $D_1 = [4, 8]$. The figure shows that by increasing D of user 1, its SIR increases and has a more prominent peak across the area. The SIR increase is the result from the less overlapped energy ball along the time axis at the same location, which reduces the ISI of user 1.

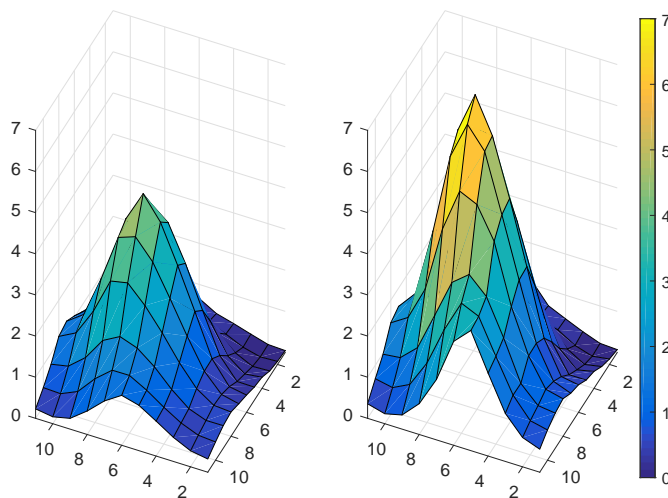


Figure 5.2: Spatial focusing effect with $D = 4$ on the left and $D = 8$ on the right for user 1.

5.2.2 Spatial Impact of Backoff Factor on Interference

Next, let us illustrate the effect of D in the spatial domain. Suppose again a two user TRDMA system with same transmit power allocated for the two users. User 1's backoff factor is chosen from $D_1 = [4, 6, 8, 10, 12]$ and user 2's backoff factor $D_2 = 4$. We again suppose that there is no noise at receiver and focus on the signal to interference ratio (SIR). Fig. 5.3 shows the SIR of the two users with different D_1 s. When D_1 increases, the SIR of user 2 increases. With a larger D_1 and a fixed channel delay spread, the transmitted symbols of user 1 are farther apart, and less energy is leaked to user 2.

The two simplified examples show that using a larger backoff rate $D'_i > D_i$ has two effects. First, the SIR of user i increases due to the decrease of ISI, which is the result of larger intervals between the energy focusing balls in the time domain.

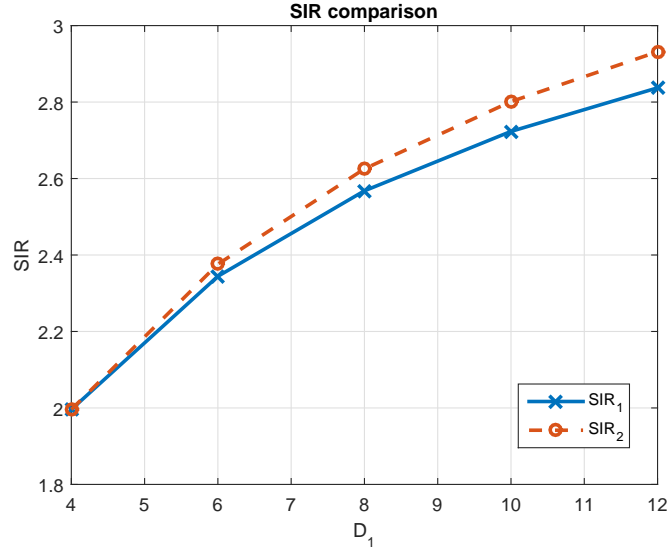


Figure 5.3: SIR of two users with $D_1 = [4, 6, 8, 10, 12]$.

Secondly, the SIRs of the other users also increase due to the decrease of the IUI, which is the result of the less energy leakage outside of the ball in the space. Both the increase of SIRs, either by decreasing IUI or ISI, comes at the cost of the reduced transmission rate. Simply put, with a larger D_i , user i increases the SIR of everyone in the system, at the cost of a lower transmission rate.

5.3 Weighted Rate Maximization

Since backoff factor plays an important role in the interference, we propose a weighted throughput maximization algorithm for the downlink TRDMA system by adjusting the backoff factors D_i to manage the interference. Let us first formulate the system objectives and the QoS constraints of the users. Suppose that there are N users in the system and each user's backoff factor D_i is chosen from a set $\{D^1, D^2, \dots, D^M\}$, where M is the number of available backoff factor settings to

the users. We assume that the application layer tolerates transmission delay, but not transmission error caused by bit/packet error that requires retransmission. In order to reduce the transmission error, each user has a minimum SINR constraint γ_i and can only transmit when SINR is larger than Γ_i . Given the Γ_i , the transmission rate is denoted as $W \log_2(1 + \Gamma_i)/D_i$, where W is the bandwidth of the TR system, and D_i is the adapted backoff factor. The weight α_i is assigned to each of the users to reflect the relative importance between the users. Denote the allocated power assigned by physical layer and the path gain for user i as p_i and G_i , respectively. Denote the maximum system power as P_{max} . Based on this setup, the rate maximization by optimizing backoff factor adaptation and user selection can be formulated as

$$\begin{aligned}
& \underset{x_i, D_i}{\text{maximize}} \quad W \sum_i \frac{\alpha_i x_i \log_2(1 + \Gamma_i)}{D_i} \\
& \text{subject to } x_i \in \{0, 1\}, \forall i, \quad \sum_{i=1}^N p_i x_i \leq P_{max} \\
& \quad \quad \quad \frac{p_i G_i x_i}{G_i Z_i + \sigma_i^2} \geq \Gamma_i x_i, \forall i,
\end{aligned} \tag{5.3}$$

where x_i is the decision variable and $x_i = 1$ denotes that user i is selected for transmission. The term Z_i is the total interference to user i , which is a function of the decision variables x_i , the power allocated p_i , the backoff factors D_i , the channel \mathbf{h}_i and the waveform \mathbf{g}_i of all the users in the network. The objective function is not convex and the decision variables appear on both the numerator and denominator of the objective function, so it is difficult to obtain the optimal solution by solving the problem directly without transformation. To tackle this challenge, we convert the problem to an MIQCQP that can be solved with much lower complexity as the following.

First, for the brevity of notation and analysis, we assume that the backoff factor satisfies $D^{m+1} = kD^m$, where k is the ratio between successive backoff factors. We assume $R_i = W \log_2(1 + \Gamma_i)/D^1$ and the rate using D^m is R_i/k^{m-1} due to the fixed ratio between the backoff factors.

Each user i has a binary decision vector \mathbf{x}_i of size M , defined as

$$\mathbf{x}_i = [x_i^1 \quad x_i^2 \quad \cdots \quad x_i^M]^T. \quad (5.4)$$

When user i is adapted with backoff rate D^m , $x_i^1 = x_i^2 = \cdots = x_i^m = 1$ and other entries in \mathbf{x}_i are 0. The decision vector \mathbf{x}_i is constructed in such a way that we can optimally allocate the backoff factor and select a subset of users for transmission simultaneously. By the requirement of the decision vector, $x_i^1 = 1$ when user i is selected for transmission, no matter which backoff factor is adapted. We define the decision vector \mathbf{x} to be the concatenation of the decision vector of all users as

$$\mathbf{x} = [\mathbf{x}_1^T \quad \mathbf{x}_2^T \quad \cdots \quad \mathbf{x}_N^T]^T. \quad (5.5)$$

Define the rate vector \mathbf{r}_i as a vector of size M as

$$\mathbf{r}_i = \left[\alpha_i R_i \quad -\alpha_i \frac{k-1}{k} R_i \quad -\alpha_i \frac{k-1}{k^2} R_i \cdots \quad -\alpha_i \frac{k-1}{k^{M-1}} R_i \right]^T. \quad (5.6)$$

Therefore, $\mathbf{r}_i^T \mathbf{x}_i$ is the transmission rate of user i with the adapted backoff factor. Let \mathbf{r} be a vector of size NM with entries

$$\mathbf{r} = [\mathbf{r}_1^T \quad \mathbf{r}_2^T \cdots \quad \mathbf{r}_N^T]^T, \quad (5.7)$$

and the system throughput is a linear function that can be expressed as $\mathbf{r}^T \mathbf{x}$.

The constraints of the optimization formulation is listed as follows. First, the decision variables are binary,

$$x_i^m \in \{0, 1\}, \quad i = 1, \dots, N, \quad m = 1, \dots, M. \quad (5.8)$$

If user i selects to use backoff factor D^m , then $x_i^1 = x_i^2 = \dots = x_i^m = 1$ and other entries be 0. This translates to another set of constraints on the decision variable as

$$x_i^{m+1} \leq x_i^m, \quad \forall i, \quad m = 1, \dots, M - 1. \quad (5.9)$$

The third constraint is that the sum of allocated power cannot exceed the maximum transmitting power of the AP. Let \mathbf{p} be an all zero vector of size NM , except that $\mathbf{p}((i - 1)M + 1) = p_i, i = 1, \dots, N$. The constraint on the total power consumption becomes

$$\mathbf{p}^T \mathbf{x} \leq P_{max}, \quad (5.10)$$

where $\mathbf{p}((i - 1)M + 1)$ is multiplied with x_i^1 which is 1 whenever user i is selected to transmit.

In order to convert the constraint on each user's SINR, we need to calculate the normalized interference with unit power channel \mathbf{h}_i and unit power waveform \mathbf{g}_i . The actual interference can be calculated by multiplying the transmit power p_i and the channel gain G_i with the corresponding normalized interference terms. To characterize the normalized IUI and ISI for user i under the adapted backoff factors, we first define several terms. Let $I_i^m, m = 1, 2, \dots, M$ be defined as

$$I_i^1 = \sum_{\substack{l=-\frac{L-1}{D^1} \\ l \neq 0}}^{\frac{L-1}{D^1}} |(h_i * g_i)[D^1 l]|^2, \quad (5.11)$$

and for $m > 1$,

$$I_i^m = \sum_{\substack{l=-\frac{L-1}{D^m} \\ l \neq 0 \\ \frac{D^{m-1}l}{D^m} \neq \text{integer}}}^{\frac{L-1}{D^m}} |(h_i * g_i)[D^m l]|^2. \quad (5.12)$$

Let $I_{ij}^m, m = 1, 2, \dots, M$ be defined as

$$I_{ij}^1 = \sum_{l=-\frac{L-1}{D^1}}^{\frac{L-1}{D^1}} |(h_i * g_j)[D^1 l]|^2, \quad (5.13)$$

for $m > 1$,

$$I_{ij}^m = \sum_{\substack{l=-\frac{L-1}{D^m} \\ \frac{D^{m-1}l}{D^m} \neq \text{integer}}}^{\frac{L-1}{D^m}} |(h_i * g_j)[D^m l]|^2. \quad (5.14)$$

Denote \mathbf{I}_i to be the normalized ISI row vector of user i as

$$\mathbf{I}_i = [I_i^1 \quad - I_i^2 \quad \dots \quad - I_i^M], \quad (5.15)$$

and denote \mathbf{I}_{ij} to be the normalized IUI row vector caused by user j to user i as

$$\mathbf{I}_{ij} = [I_{ij}^1 \quad - I_{ij}^2 \quad \dots \quad - I_{ij}^M]. \quad (5.16)$$

By the construction of \mathbf{I}_i and the relation that $x_i^1 = x_i^2 = \dots = x_i^m = 1$ if user i choose D^m , $\mathbf{I}_i \mathbf{x}_i$ is the normalized ISI of user i using backoff factor D^m . By the same token, $\mathbf{I}_{ij} \mathbf{x}_j$ is the normalized IUI of user j to user i with the adapted backoff factor.

Let the interference row vector \mathbf{z}_i of user i be defined as

$$\mathbf{z}_i = [p_1 \mathbf{I}_{i1} \quad p_2 \mathbf{I}_{i2} \quad \dots \quad p_i \mathbf{I}_i \quad \dots \quad p_N \mathbf{I}_{iN}], \quad (5.17)$$

where we multiply the allocated power p_i of the users to the normalized interference.

With the defined interference vector \mathbf{z}_i , the total interference to user i due to IUI and ISI is $\mathbf{z}_i\mathbf{x}$, then the minimum SINR requirement can be expressed as

$$\frac{p_i G_i x_i^1}{G_i \mathbf{z}_i \mathbf{x} + \sigma_i^2} \geq \Gamma_i x_i^1 \quad (5.18)$$

We define \mathbf{Z}_i to be an NM by NM all zero matrix, except that $[(i-1)M+1]$ -th row being \mathbf{z}_i and \mathbf{q}_i as an all zero vector of size NM except the $\mathbf{q}_i((i-1)M+1) = \sigma_i^2/G_i - p_i/\Gamma_i$. The SINR requirement constraint is converted as

$$\begin{aligned} & \frac{p_i G_i x_i^1}{G_i \mathbf{z}_i \mathbf{x} + \sigma_i^2} \geq \Gamma_i x_i^1 \\ \equiv & \frac{p_i}{\Gamma_i} x_i^1 \geq x_i^1 \mathbf{z}_i \mathbf{x} + \frac{\sigma_i^2}{G_i} x_i^1 \\ \equiv & \mathbf{x}^T \mathbf{Z}_i \mathbf{x} + \mathbf{q}_i^T \mathbf{x} \leq 0 \end{aligned} \quad (5.19)$$

Denote $\lambda_j(\mathbf{Z}_i + \mathbf{Z}_i^T)$, $j = 1, \dots, NM$ to be the eigenvalues of $\mathbf{Z}_i + \mathbf{Z}_i^T$ in non-decreasing order. By the Weyl's inequality [22], any constant $d_i \geq \lambda_1(\mathbf{Z}_i + \mathbf{Z}_i^T)$ will make $\mathbf{Q}_i = \mathbf{Z}_i + \mathbf{Z}_i^T + d_i \mathbf{I}_{NM}$ a positive semidefinite matrix, where \mathbf{I}_N denotes an identity matrix with size N . Define $\mathbf{1}$ as the all one vector with corresponding dimension. Use the Weyl's inequality with the property $x_i^2 = x_i$ of the binary variables and the SINR constraint for user i is

$$\begin{aligned} & \frac{1}{2} \mathbf{x}^T (\mathbf{Z}_i + \mathbf{Z}_i^T + d_i \mathbf{I}_{NM}) \mathbf{x} + \\ & \quad \left(\mathbf{q}_i^T - \frac{d_i}{2} \mathbf{1}_{NM} \right) \mathbf{x} \leq 0, \quad \forall i \\ \equiv & \frac{1}{2} \mathbf{x}^T \mathbf{Q}_i \mathbf{x} + \left(\mathbf{q}_i^T - \frac{d_i}{2} \mathbf{1}_{NM} \right) \mathbf{x} \leq 0, \quad \forall i. \end{aligned} \quad (5.20)$$

To sum up, the optimization problem is converted to an MIQCQP as follows

$$\begin{aligned}
& \underset{\mathbf{x}}{\text{maximize}} \quad \mathbf{r}^T \mathbf{x} \\
& \text{subject to} \quad x_i^m \in \{0, 1\}, \forall i, m \quad x_i^{m+1} \leq x_i^m, \forall i, m \\
& \mathbf{p}^T \mathbf{x} \leq P_{max} \\
& \frac{1}{2} \mathbf{x}^T \mathbf{Q}_i \mathbf{x} + \left(\mathbf{q}_i^T - \frac{d_i}{2} \mathbf{1}_{NM} \right) \mathbf{x} \leq 0, \forall i,
\end{aligned} \tag{5.21}$$

which can be solved with much lower complexity than exhaustive search.

5.4 Waveform Design with SINR Constraints

The rate optimization algorithm selects users based on the given waveforms and the given set of backoff rates, and maintains the SINR requirements for the selected users. However, the rate optimization algorithm does not consider the fact that the given waveforms are not the optimal ones for the selected users and backoff rates. Therefore, an optimization of the transmission waveform and the power allocation shall be considered to increase the transmission rate and therefore improve the system performance, given the selected users and the adapted backoff factors. Existing works has investigated the waveform design based on the given waveform and the backoff factor in the TR system [58] without considering different backoff factor adaptations and the minimum SINR requirement of the users. In this section, we extend the proposed algorithm for adaptation to different badkoff factors and to maintain the minimum SINR requirement.

Suppose we get a subset $S \subseteq \{1, 2, \dots, N\}$ of the N users from the rate optimization algorithm with the corresponding waveforms $\{\mathbf{g}_i\}_{i \in S}$ and backoff factor

$\{D_i\}_{i \in S}$. From (5.2), the SINR for user $i \in S$ is

$$\text{SINR}_i^{DL} = \frac{p_i \mathbf{g}_i^H \mathbf{R}_i^{(0)} \mathbf{g}_i}{p_i \mathbf{g}_i^H \hat{\mathbf{R}}_i \mathbf{g}_i + \sum_{j \in S, j \neq i} p_j \mathbf{g}_j^H \mathbf{R}_j \mathbf{g}_j + \sigma^2}, \quad (5.22)$$

where $\mathbf{R}_i^{(0)} = G_i \mathbf{H}_i^{(L)H} \mathbf{H}_i^L$. \mathbf{H}_i is a $(2L - 1) \times L$ Toeplitz matrix with each column being the shifted version of normalized CIR \mathbf{h}_i from the AP to the TD. We absorb the channel power into the channel gain factor G_i . $\mathbf{H}_i^{(l)}$ to be the l^{th} row of \mathbf{H}_i and superscript H is Hermitian operator. $\mathbf{R}_j = G_j \tilde{\mathbf{H}}_j^H \tilde{\mathbf{H}}_j$, where $\tilde{\mathbf{H}}_j$ is the upsampled \mathbf{H}_j with backoff factor D_j and the sampling center is located at $\mathbf{H}_j^{(L)}$. Then $\hat{\mathbf{R}}_i = \mathbf{R}_i - \mathbf{R}_i^{(0)}$. The first term and the second term in the denominator represent the ISI and IUI respectively. In this section, we consider the joint design of the waveform $\mathbf{G} = [\mathbf{g}_i], \forall i \in S$ and the power allocation vector $\mathbf{p} = [p_i]^T, \forall i \in S$ to maximize the weighted sum rate of the selected users subject to the SINR constraints, i.e.,

$$\begin{aligned} & \underset{\mathbf{p}, \mathbf{G}}{\text{maximize}} \quad W \sum_{i \in S} \frac{\alpha_i}{D_i} \log(1 + \text{SINR}_i^{DL}) \\ & \text{subject to} \quad \mathbf{1}^T \mathbf{p} \leq P_{max}, \quad p_i \geq 0, \end{aligned} \quad (5.23)$$

$$\mathbf{g}_i^H \mathbf{g}_i = 1, \quad \text{SINR}_i^{DL} \geq \Gamma_i, \forall i \in S,$$

where the last set of constraints ensure that the constraints of the original rate adaptation algorithms are fulfilled with the newly designed waveforms and allocated powers. $\mathbf{1}$ is an all-one vector of size $|S|$, where $|\cdot|$ is the cardinality of the set.

5.4.1 Uplink Downlink Duality

In the optimization problem shown in (5.23), SINR of user i depends on the waveforms of users $j, j \in S, j \neq i$, therefore the waveforms for all users have to be designed together. The simultaneous optimization of all users' waveforms makes the optimal waveform design hard to solve. We use the well-known downlink-uplink duality to untangle the interdependence between users. With the duality, the optimal downlink waveforms can be individually obtained via the virtual uplink setup with fixed power allocation. Moreover, the achievable SINR regions are the same for both the downlink and the virtual uplink case, and therefore the SINR requirement of the downlink can be also applied at the virtual uplink case. The transformed virtual uplink problem can be express as follows.

$$\begin{aligned} & \underset{\mathbf{q}, \mathbf{G}}{\text{maximize}} \quad W \sum_{i \in S} \frac{\alpha_i}{D_i} \log(1 + \text{SINR}_i^{UL}) \\ & \text{subject to} \quad \mathbf{1}^T \mathbf{q} \leq P_{max}, q_i \geq 0, \\ & \quad \quad \quad \mathbf{g}_i^H \mathbf{g}_i = 1, \text{SINR}_i^{UL} \geq \Gamma_i, \forall i \in S, \end{aligned} \tag{5.24}$$

where \mathbf{q} represents the $|S| \times 1$ uplink power allocation in the virtual uplink. $\{\mathbf{g}_i\}_{i \in S}$ is the uplink transmit waveform which is the same as the downlink transmit waveform. The SINR for the uplink case is expressed as

$$\text{SINR}_i^{UL} = \frac{\mathbf{g}_i^H \mathbf{R}_i^{(0)} \mathbf{g}_i q_i}{\mathbf{g}_i^H \hat{\mathbf{R}}_i \mathbf{g}_i q_i + \sum_{j \in S, j \neq i} \mathbf{g}_i^H \mathbf{R}_j \mathbf{g}_i q_j + \sigma^2}, \tag{5.25}$$

and SINR_i^{UL} only depends on the waveform \mathbf{g}_i of user i . SINR_i^{UL} maximizing waveform given the power allocation vector \mathbf{q} is the MMSE waveform \mathbf{u}_i , which is

$$\mathbf{g}_i^{MMSE} = c_i^{MMSE} \left(\sum_{j=1, j \in S} q_j \mathbf{R}_j + \sigma^2 \mathbf{I} \right)^{-1} \mathbf{H}_k^{(1)H}. \quad (5.26)$$

The constant c_i^{MMSE} is to normalize the waveform \mathbf{g}_i^{MMSE} to unit norm.

5.4.2 Power Allocation with SINR Constraint

Given a set of the transmit waveforms, $\{\mathbf{g}_i\}_{i \in S}$, the optimization problem involves solving the power allocation vector \mathbf{q} with a given sum power constraint. The optimization problem is non-convex and therefore it is hard to obtain directly, and we transform the optimizing variables from the power allocation vector \mathbf{q} to the SINR allocation $\{\gamma_i\}_{i \in S}$. The power allocation can be obtains after $\{\gamma_i\}_{i \in S}$ is allocated properly.

The γ_i can be expressed as

$$\gamma_i = \text{SINR}_i^{UL} = \frac{\mathbf{g}_i^H \mathbf{R}_i^{(0)} \mathbf{g}_i q_i}{\mathbf{g}_i^H \hat{\mathbf{R}}_i \mathbf{g}_i q_i + \sum_{j \in S, j \neq i} \mathbf{g}_i^H \mathbf{R}_j \mathbf{g}_i q_j + \sigma_i^2}. \quad (5.27)$$

Denote Λ be a diagonal matrix where $[\Lambda]_{ii} = \gamma_i / \mathbf{g}_i^H \mathbf{R}_i^{(0)} \mathbf{g}_i$ and Φ with

$$[\Phi]_{kj} = \begin{cases} \mathbf{g}_j^H \mathbf{R}_k \mathbf{g}_j, & k \neq j \\ \mathbf{g}_j^H \hat{\mathbf{R}}_k \mathbf{g}_j, & k = j \end{cases} \quad (5.28)$$

With the defined matrices, the power allocation \mathbf{q} can be represented by the SINR γ_i as

$$\mathbf{q} = (\mathbf{I} - \Lambda \Phi^T)^{-1} \Lambda \sigma, \quad (5.29)$$

where σ is a $|S| \times 1$ vector with all elements equal to σ^2 . The \mathbf{q} exists as long as $(\mathbf{I} - \Lambda \Phi^T)$ is invertible. This constraints can be enforces if the spectral radius $\rho(\cdot)$

is smaller than 1.

The weighted sum rate optimization problem is transformed as the following into an SINR allocation problem

$$\begin{aligned} & \underset{\gamma_i, i \in S}{\text{maximize}} \quad \sum_{i \in S} W \frac{\alpha_i}{D_i} \log(1 + \gamma_i) \\ & \text{subject to} \quad (\mathbf{I} - \Lambda \Phi^T)^{-1} \Lambda \sigma \leq P_{max} \end{aligned} \quad (5.30)$$

$$\rho(\Lambda \Phi^T) < 1, \gamma_i > \Gamma_i, \quad \forall i \in S,$$

By the Karush-Kuhn-Tucker (KKT) conditions, the optimum SINR allocation γ_i satisfies

$$\gamma_i = \max \left(\frac{\alpha_i}{D_i \nu^* t_i} - 1, \Gamma_i \right), \quad (5.31)$$

$$(\mathbf{I} - \Lambda \Phi^T)^{-1} \Lambda \sigma = P_{max}, \quad (5.32)$$

$$\rho(\Lambda \Phi^T) < 1, \quad (5.33)$$

where ν^* is KKT multiplier and t_i is

$$t_i = \frac{1}{\gamma_i} \mathbf{1}^T (\mathbf{I} - \Lambda \Phi^T)^{-1} \mathbf{e}_i \mathbf{e}_i^T (\mathbf{I} - \Lambda \Phi^T)^{-1} \Lambda \sigma, \quad (5.34)$$

and \mathbf{e}_i is the i^{th} column of a $|S|$ by $|S|$ identity matrix.

Based on the KKT condition, we can find the optimal SINR allocation via waterfilling and the algorithm is summarized in Algorithm 1. The SINR constraint is enforced in the algorithm at line 5 such that the minimum SINR level is ensured in each iteration of optimization. We iterate the SINR allocation and the MMSE

waveform design until convergence and the specific two-step procedure is given in Algorithm 2.

$$\mathbf{p} = (\mathbf{I} - \Lambda \Phi)^{-1} \Lambda \sigma \quad (5.35)$$

Algorithm 1 Iterative SINR Waterfilling with Minimum SINR Constraints

- 1: Given \mathbf{q} , initialize γ_i with (5.25)
 - 2: **while** \mathbf{q} not converges, and max. iteration not reached
 - 3: $\lambda_{max} = \max_j \alpha_j / D_j t_j, \lambda_{min} = \delta > 0$
 - 4: **while** $|\mathbf{1}^T (\mathbf{I} - \Lambda \Phi^T)^{-1} \Lambda \sigma - P_{max}| > \epsilon$
 - 5: $\lambda = (\lambda_{min} + \lambda_{max}) / 2, \gamma_i = \max \left(\frac{\alpha_i}{D_i \nu^* t_i} - 1, \Gamma_i \right), \forall i \in S$
 - 6: **if** $\rho(\Lambda \Phi^T) < 1$ **then**
 - 7: **if** $\mathbf{1}^T (\mathbf{I} - \Lambda \Phi)^{-1} \Lambda \sigma < P_{max}$ **then**
 - 8: $\lambda_{max} = \lambda$
 - 9: **else**
 - 10: $\lambda_{min} = \lambda$
 - 11: **end if**
 - 12: $\lambda_{min} = \lambda$
 - 13: **end if**
 - 14: **end while**
 - 15: Compute \mathbf{q} with (5.29)
 - 16: **end while**
-

Algorithm 2 Iterative Weighted Sum Rate Optimization with SINR Constraint

- 1: Initialize $q_i = p_i$
 - 2: **while do** \mathbf{q} or $\{\mathbf{u}_j\}_{j \in |S|}$ not converge or max. iteration not reached
 - 3: Calculate $\{\mathbf{u}_j\}_{j \in |S|}$ using (5.26)
 - 4: Calculate \mathbf{q} using Algorithm 1
 - 5: **end while**
 - 6: Obtain γ_i using (5.27)
 - 7: Obtain \mathbf{p} using (5.35)
-

5.5 Simulation Results

We evaluate the proposed backoff rate adaptation algorithm with the following setup. The number of users N is chosen from 4, 6, 8, 10. The path gain G_i is generated by assuming the AP is located at the center of 20m by 20m area while the receivers are randomly distributed within. The pathloss exponent is chosen to be 3.5 and the bandwidth W is 125 MHz. The CIRs \mathbf{h}_i are generated based on the model in [20], and the waveform \mathbf{g}_i are the time-reversed and conjugated CIRs, unless otherwise designed. The power p_i is generated uniformly from 0.1 to 0.3 and the maximum power P_{max} is 1. The signal to noise ratio is 0 dB and the SINR requirement Γ_i is generated uniformly from 0.3 to 0.6. The weight α_i is generated uniformly from [0, 1]. For each of the settings, we perform 5000 channel and location realizations. To get the optimal solution of the original optimization problem defined in (5.3), we do an exhaustive search by assuming all users choose the same backoff factor D^1 . The performance metric is measured by comparing the proposed algorithm

with the result of the exhaustive search in terms of absolute weighted sum rate and the weight sum rate ratio. Finally, we use Gurobi [18] as the MIQCQP solver.

We evaluate the performance of the rate adaptation algorithm by comparing the weighted sum rate against the case when the users have to use fixed D^1 . Fig. 5.4 shows the average weighted sum rate with $M = 2$, $k = 4$ using different D^1 s and the case when users use fixed D^1 . Result shows that the proposed algorithm outperforms in all simulated cases than the fixed D^1 case. The increase of throughput is larger when D^1 is small, i.e. when the IUI and ISI are more severe. Two conclusions can be made according to the result. First, the proposed algorithm effectively adjusts D_i for the users, manages the interference and increases the system weighted sum rate. Secondly, the algorithm is more effective in crowded networks with severe interference because some users can use larger backoff for transmission and reduce the interference to others. This is strongly desirable when massive number of users are present in the network.

In order to show the relative increase in the throughput with the proposed algorithm, we calculate the ratio ρ between the throughput of the MIQCQP algorithm R_{MIQCQP} and the throughput R_{fixed} obtained by fixed D^1 s, i.e. $\rho = R_{MIQCQP}/R_{fixed}$. Fig. 5.5 shows the average ρ with $M = 2$, different D^1 s and $k = \{2, 4\}$. All values of ρ are above 1 in all scenarios we simulate, which shows that the proposed algorithm increases the system throughput. When N is large, the exhaustive search has more flexibility in choosing the optimal set of simultaneously transmitting users, so ρ decreases a little with the increase of N . The second observation is that the ρ increases with k , which results in a higher total throughput

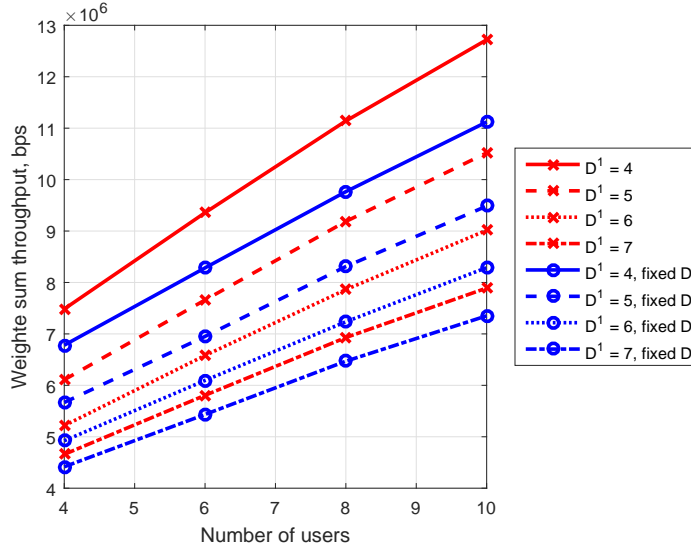


Figure 5.4: Throughput comparison with the proposed algorithm and fixed D^1 , $M = 2$, $k = 4$.

due to the much lowered interference at the cost of reduced individual transmission rates of some users.

To investigate the system fairness with the use of the optimal backoff factor adaptation, we calculate the fairness index $J(\mathbf{x}) = \left(\sum_{i=1}^N x_i \right)^2 / N \sum_{i=1}^N x_i^2$ proposed in [7], where \mathbf{x} denotes the binary decision variables for the users. $J(\mathbf{x})$ has maximum of 1 which is completely fair between users, and minimum of $1/N$ which is the most unfair case when only one user transmits. $J(\mathbf{x})$ captures how evenly the transmission opportunities are distributed among the users. For the proposed adaptation algorithm, x_i^1 is used for J calculation because x_i^1 is 1 when user i is selected, no matter which backoff factor setting is used. We use exhaustive search to find the optimal \mathbf{x} for the case using a fixed D^1 s. Fig. 5.6 shows the averaged $J(\mathbf{x})$ with different N and D^1 with $k = 2$ and $M = 2$. $J(\mathbf{x})$ is larger for the adaptation

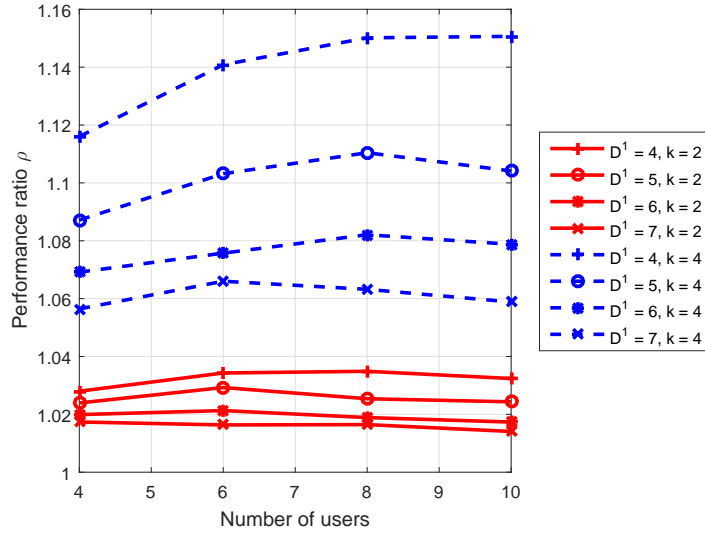


Figure 5.5: Performance, $\rho = R_{MIQQP}/R_{fixed}$, comparison with different k , $M = 2$ algorithm in all cases. With smaller D^1 , the proposed adaptation algorithm shows larger increase in the fairness index, which means the proposed algorithm is more effective when IUI and ISI is more severe.

Lastly, we evaluate the performance of the proposed algorithm with another physical layer waveform to show the versatile applicability of the proposed adaptation algorithm. We use the waveform design algorithm proposed in [57]. The original algorithm is proposed for the uplink system, and we modify it using the downlink-uplink duality for the downlink TRDMA system. Fig. 5.7 shows the results and we observe similar performance as in Fig. 5.5. The ratio ρ is larger than 1 in all scenarios, especially when k is large which reduces the interference greatly using a lower rate setting.

Fig. 5.8 shows the Jain's index for different D^1 with different N at $k = 2, M = 2$. The results shows that the waveform design increases the fairness than that in

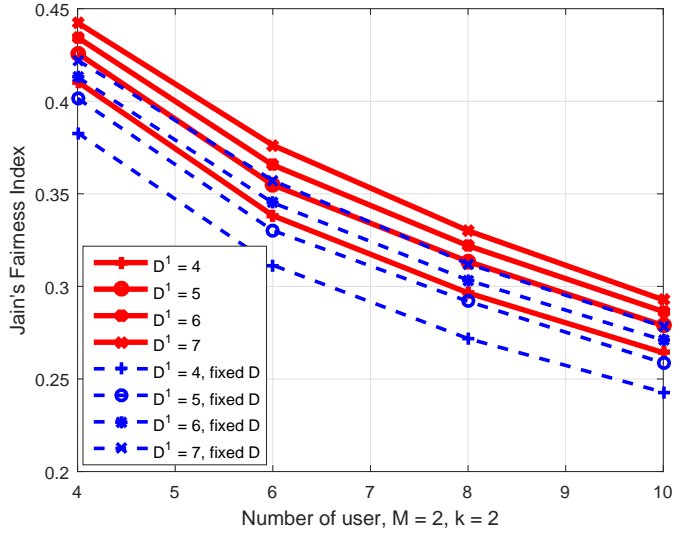


Figure 5.6: Fairness index $J(\mathbf{x})$ comparison between the proposed algorithm and fixed D , $k = 2$, $M = 2$

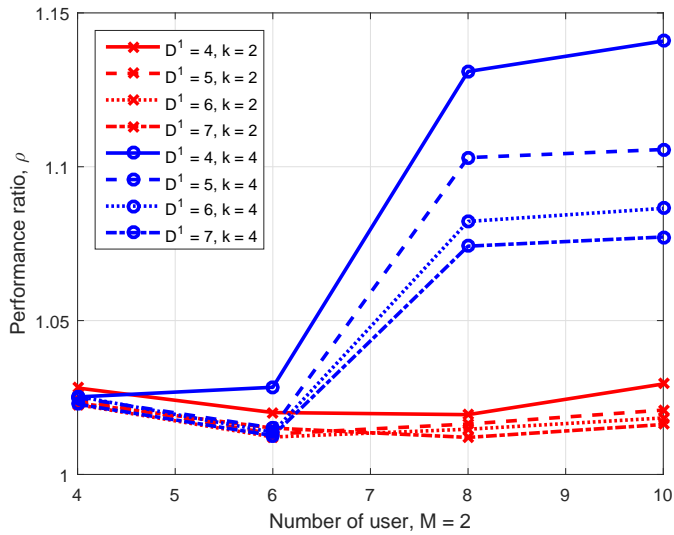


Figure 5.7: Performance comparison with different k with waveform design, $M = 2$

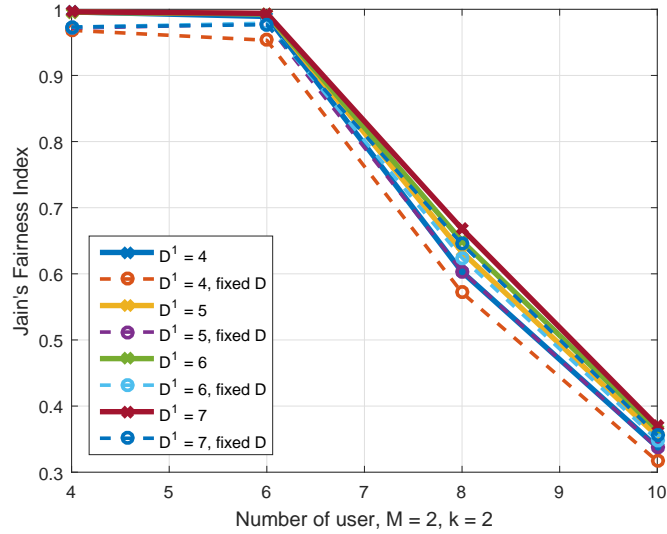


Figure 5.8: Fairness index $J(\mathbf{x})$ comparison between the proposed algorithm and fixed D with waveform design, $k = 2$, $M = 2$

Fig. 5.6, which shows the waveform design alleviate the IUI and ISI. The proposed algorithm further increases the fairness index slightly in all scenarios. The increase in both ρ and Jain's index with waveform design signifies the effectiveness of the backoff rate adaptation algorithm even with different physical layer structures.

We have evaluated the performance of the proposed rate adaptation algorithm in the previous results. We next evaluate the rate adaptation algorithm with waveform design that ensures the users' SINR requirements. The number of users $N = \{4, 6, 8, 10\}$ and $D^1 = \{4, 5, 6, 7\}$. The number of backoff factor set $M = 2$ and the ratio $k = \{2, 4\}$. The performance metric is evaluated using the ratio ρ between the weighted sum rate of the rate adaptation algorithm with waveform design and without waveform design, i.e. $\rho = R_{WD}/R_{MIQCQP}$. Result in Fig. 5.9 shows that the waveform design algorithm increases the system performance in all cases. When

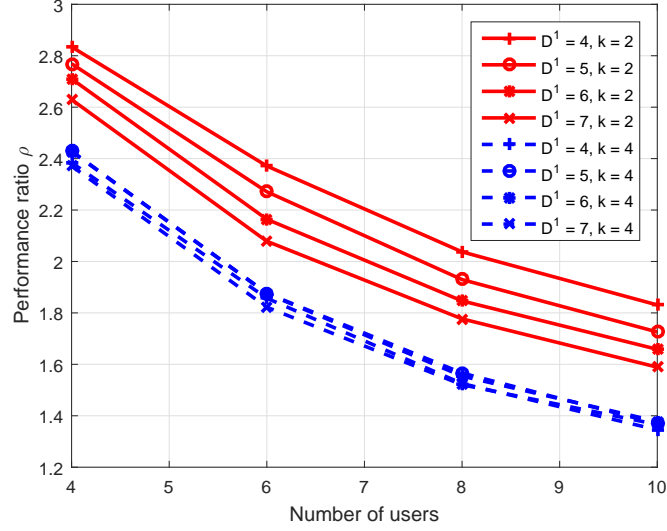


Figure 5.9: Performance comparison of rate adaptation combined with and without waveform design, $M = 2$.

D^1 is small and the interference is large, ρ is much larger because the waveform design reduces the interference and redistributes the transmission power among the selected users in S . When k is larger, the rate adaptation algorithm has already managed the interference effectively by using much larger backoff rate, and therefore the performance increase is smaller when k is larger.

Next, we evaluate the performance of the proposed rate adaptation algorithm and the waveform design as a whole, and compare with the result of exhaustive search where all users use D^1 . The number of users $N = \{4, 6, 8, 10\}$ and $D^1 = \{4, 5, 6, 7\}$. The ratio $k = \{2, 4\}$. Fig. 5.10 shows the result of the ratio $\rho = R_{WD}/R_{fixed}$ between the weighted sum rate of the proposed algorithm and the exhaustive search. Result shows that the performance increases in all cases, and in cases with larger interference, i.e. smaller D^1 , the performance increase is larger.

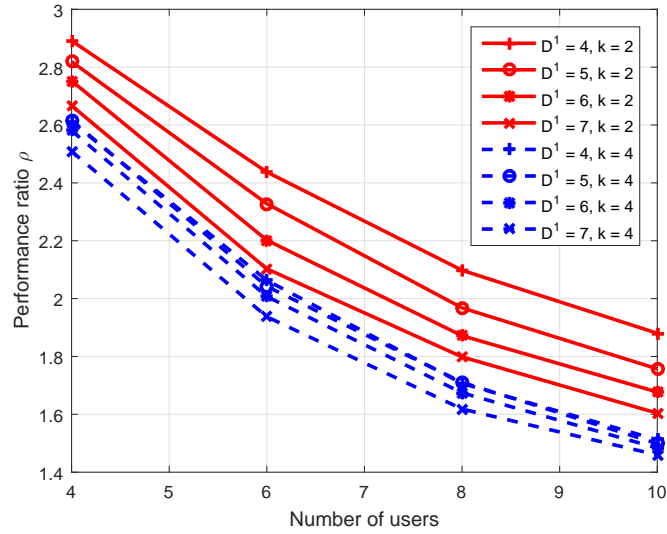


Figure 5.10: Performance comparison between fixed D^1 and rate adaptation with waveform design, $M = 2$.

5.6 Summary

In this chapter, we propose a rate adaptation algorithm to simultaneously determine the optimal subset of transmitting users and the optimal backoff factors for users to maximize the weighted sum throughput of a downlink TRDMA system. The rate maximization problem with minimum SINR constraints is transformed into an MIQCQP problem which can be solved efficiently with an optimization solver. In the second part, we propose a waveform design and power allocation algorithm according to the output of the selected user, the assigned backoff factor and the SINR constraints of the selected users. Results show that the proposed algorithm improves both the system throughput and the fairness between the users, especially in cases when the interference is severe. The performance, efficiency, and the versatile applicability to different physical layer implementations make the

proposed algorithm suitable suitable for the time reversal system.

Chapter 6

Conclusions and Future Work

6.1 Conclusions

In the first part of this dissertation, we demonstrated the spatial focusing of the TR system and proposed a positioning system with 1-inch resolution. Based on the excellent localization precision, we propose a VCTR system for indoor tracking by deploying multiple virtual checkpoints within the target area. In the second part, we focused on the interference management problem for increasing the system performance. First, we proposed a MAC layer scheduler that maximized the system weighted sum rate while satisfying the users' QoS requirement. We then devised a rate adaptation algorithm that manages the interference by optimally selecting the backoff factors for the users in the TR system. More specifically, we addressed the following problems in this dissertation.

In Chapter 2, we proposed a time reversal indoor positioning system by utilizing the unique location-specific characteristic of CIR. We addressed the ill-posed single-AP indoor localization problem by decomposing it into two well-defined subproblems. We solve the first subproblem by building a database that maps the physical geographical location to its corresponding CIR space, which we call the

data collection phase. The second subproblem is to calculate the TRRS between the estimated CIR from the unknown users with those in the database. We built a prototype to evaluate the characteristics of the CIR and the performance of the proposed scheme. Results show that the indoor positioning system prototype is the first-ever system to achieve 1 to 2 cm accuracy in both line-of-sight and non-line-of-sight cases using only one pair of transmitter and receiver both equipped with a single antenna.

In Chapter 3, a novel indoor tracking system based on the virtual checkpoint is proposed. With the experiment results shown in Chapter 2, we constructed virtual checkpoints where the CIR information within the checkpoints is collected. The location of the unknown user can be identified when the user passes through the virtual checkpoints. We built a CIR collection machine prototype for automated large-scale CIR information collection with a user-friendly GUI. By collecting the statistics of the TRRS between the unknown user and the CIRs in the database, we found the CDF of the TRRS of the cases when the unknown user passes the virtual checkpoint or not. The clear different in CDF indicates that by selecting a proper threshold, the proposed tracking system can detect the user passing through the virtual checkpoint with very low false alarm.

In Chapter 4, we proposed a novel scheduler for the general 5G downlink system. The scheduler maximizes the system weighted throughput and satisfies the SINR constraints of the users. The objective and constraints are transformed into an MIQCQP problem. The proposed scheduler has a linear complexity, as compared with the exponential complexity of the exhaustive search with only slight

performance degradation. We also investigated the impact of imperfect channel information on the proposed scheduler. We analyzed the Golay sequence based channel estimation scheme of the TR system and reveal the same channel estimation error distribution as the massive MIMO system. Experiment results show that the proposed scheduler is versatile to different physical layer structures and is robust the channel estimation error. The versatility, robustness, and low complexity make the proposed scheduler suitable for systems with a massive number of users and strict scheduling deadlines.

Lastly, in Chapter 5, we proposed a rate adaptation algorithm for a downlink TRDMA system. The algorithm maximizes the system weighted sum throughput by simultaneously determining the optimal subset of the transmitting users and the optimal backoff factors for the users. The rate maximization and the minimum SINR constraints of the users are transformed into an MIQCQP problem, which can be solved efficiently. We also proposed a waveform design and power allocation algorithm based on the selected users, the selected backoff factors, and the SINR constraints. Results show that the proposed algorithm improves the system throughput and the fairness between users, especially in cases where the interference is severe. The proposed algorithm is suitable for TR system deployment based on the performance, efficiency and the versatile applicability to different physical layer implementations.

6.2 Future Work

To fully develop the TR system and to meet the versatile applications, there are several open problems and challenges that need to be explored and investigated. The exploration of these issues not only leads to fruitful research results but also makes the 5G communication system come true with great IoT applications. In this dissertation, the TR technology for 5G and IoT application can be further explored in the following aspects.

First, the RF component consistency across different devices needs to be studied. The spatial temporal focusing effect of the TR system relies on the precise CIR information collected from the RF component. Any inconsistencies between the RF components, such as the receiving beam pattern, oscillator frequency mismatch, RF gain difference, etc. can significantly reduce the TR system performance. Therefore, further exploration of the quantification and the evaluation of the RF inconsistency effect on the TR performance is desirable. These researches lead to solutions to mitigate the decrease in performance and play an important role for a fruitful system design.

Moreover, the CIR information is affected by the objects in the environment. An environment change such as a chair removed or human activity may change the CIR information significantly. However, there is no precise model about how the CIR is affected by a specific object change in the surrounding environment. The CIR model is important to the VCTR system deployment for that the CIR change significantly decreases the performance and increases the need to recollect

the database. The VCTR system can reduce the frequency of recollecting database if the CIR can be modeled by some parameters. A deep investigation about CIR modeling is very helpful for actual implementation of the VCTR system and the TR system performance in general.

The proposed scheduler assumes perfect synchronization among different users in a downlink scenario. However, the precise synchronization algorithm for uplink traffic is not yet explored. The synchronization of the users affects the CIR information quality observed by the base station. A little shift in time significantly decreases the spatial temporal focusing effect of the TR system and increases the interference between users because of the low-quality CIR information. The synchronization between users with heterogeneous bandwidth also poses a challenge for the TR system design, because the granularity in time is different for different users. Some users may synchronize to a wrong time instant and reduce the system performance.

Lastly, the operation of TR system needs a large bandwidth and it is very likely that the TR system shares the frequency band with other systems. The existence of another system in the same band polluted the CIR information and degrades the TR system performance. Quantification of the performance degradation is needed for the TR system deployment. On the other hand, noise suppression algorithm and coexistence strategy are very much desirable in these cases to guarantee the TR system performance.

Bibliography

- [1] Cisco visual networking index: Global mobile data traffic forecast update, 2015v2020. Technical report, Cisco, 2016.
- [2] P. Bahl and V.N. Padmanabhan. RADAR: an in-building RF-based user location and tracking system. In *IEEE Int. Cong. Computer Communications*, volume 2, pages 775–784 vol.2, 2000.
- [3] C. Chen, Y. Chen, H. Q. Lai, Y. Han, and K. J. R. Liu. High accuracy indoor localization: A WiFi-based approach. In *IEEE Int. Conf. Acoustics, Speech and Signal Processing*, pages 6245–6249, March 2016.
- [4] Yan Chen, Feng Han, Yu-Han Yang, Hang Ma, Yi Han, Chunxiao Jiang, Hung-Quoc Lai, D. Claffey, Z. Safar, and K.J.R Liu. Time-reversal wireless paradigm for green internet of things: An overview. *IEEE Internet Things J.*, 1(1):81–98, Feb 2014.
- [5] Yan Chen, Yu-Han Yang, Feng Han, and K.J.R Liu. Time-reversal wideband communications. *IEEE Signal Process. Lett.*, 20(12):1219–1222, Dec 2013.
- [6] Yin Chen, D. Lymberopoulos, Jie Liu, and B. Priyantha. Indoor localization using FM signals. *IEEE Trans. Mobile Comput.*, 12(8):1502–1517, Aug 2013.
- [7] Dah-Ming Chiu and Raj Jain. Analysis of the increase and decrease algorithms for congestion avoidance in computer networks. *Comput. Netw. ISDN Syst.*, 17(1):1–14, Jun 1989.
- [8] H. Dahrouj and W. Yu. Coordinated beamforming for the multicell multi-antenna wireless system. *IEEE Trans. Commun.*, 9(5):1748–1759, May 2010.
- [9] J. De Rosny, G. Lerosey, and M. Fink. Theory of electromagnetic time-reversal mirrors. *IEEE Trans. Antennas Propag.*, 58(10):3139–3149, Oct 2010.
- [10] Arnaud Derode, Philippe Roux, and Mathias Fink. Robust acoustic time reversal with high-order multiple scattering. *Phys. Rev. Lett.*, 75:4206–4209, Dec 1995.
- [11] S. Dierks and Niklas Juenger. Scheduling for massive mimo with few excess antennas. In *20th Int. ITG Workshop Smart Antennas*, pages 1–5, March 2016.
- [12] G.F. Edelmann, T. Akal, W.S. Hodgkiss, Seongil Kim, W.A. Kuperman, and Hee Chun Song. An initial demonstration of underwater acoustic communication using time reversal. *IEEE J. Ocean. Eng.*, 27(3):602–609, Jul 2002.
- [13] Chen Feng, W.S.A. Au, S. Valaee, and Zhenhui Tan. Received-signal-strength-based indoor positioning using compressive sensing. *IEEE Trans. Mobile Comput.*, 11(12):1983–1993, Dec 2012.

- [14] M. Fink. Time reversal of ultrasonic fields. I. basic principles. *IEEE Trans. Ultrason., Ferroelect., Freq. Control*, 39(5):555–566, Sept 1992.
- [15] M. Fink, C. Prada, F. Wu, and D. Cassereau. Self focusing in inhomogeneous media with time reversal acoustic mirrors. In *Proc. IEEE Ultrasonics Symposium*, pages 681–686 vol.2, Oct 1989.
- [16] R.J. Fontana and S.J. Gunderson. Ultra-wideband precision asset location system. In *IEEE Conf. Ultra Wideband Systems and Technologies*, pages 147–150, May 2002.
- [17] M. Golay. Complementary series. *IRE Trans. Inf. Theory*, 7(2):82–87, Apr 1961.
- [18] Inc. Gurobi Optimization. Gurobi optimizer reference manual, 2015.
- [19] Feng Han and K.J.R Liu. A multiuser TRDMA uplink system with 2D parallel interference cancellation. *IEEE Trans. Commun.*, 62(3):1011–1022, March 2014.
- [20] Feng Han, Yu-Han Yang, Beibei Wang, Yongle Wu, and K.J.R Liu. Time-reversal division multiple access over multi-path channels. *IEEE Trans. Commun.*, 60(7):1953–1965, Jul 2012.
- [21] Benjamin E. Henty and Daniel D. Stancil. Multipath-enabled super-resolution for rf and microwave communication using phase-conjugate arrays. *Phys. Rev. Lett.*, 93:243904, Dec 2004.
- [22] Roger A. Horn and Charles R. Johnson, editors. *Matrix Analysis*. Cambridge University Press, New York, NY, USA, 1986.
- [23] Jianwei Huang, V.G. Subramanian, R. Agrawal, and R.A. Berry. Downlink scheduling and resource allocation for OFDM systems. *IEEE Trans. Wireless Commun.*, 8(1):288–296, Jan 2009.
- [24] Y. Huang, C. W. Tan, and B. D. Rao. Joint beamforming and power control in coordinated multicell: Max-min duality, effective network and large system transition. *IEEE Trans. Wireless Commun.*, 12(6):2730–2742, Jun 2013.
- [25] Yunye Jin, Wee-Seng Soh, and Wai-Choong Wong. Indoor localization with channel impulse response based fingerprint and nonparametric regression. *IEEE Trans. Wireless Commun.*, 9(3):1120–1127, March 2010.
- [26] Jahyoung Koo and Hojung Cha. Localizing WiFi access points using signal strength. *IEEE Commun. Lett.*, 15(2):187–189, February 2011.
- [27] A. Kushki, K.N. Plataniotis, and A.N. Venetsanopoulos. Kernel-based positioning in wireless local area networks. *IEEE Trans. Mobile Comput.*, 6(6):689–705, June 2007.

- [28] R. Kwan, C. Leung, and Jie Zhang. Proportional fair multiuser scheduling in LTE. *IEEE Signal Process. Lett.*, 16(6):461–464, Jun 2009.
- [29] E. Larsson, O. Edfors, F. Tufvesson, and T. Marzetta. Massive MIMO for next generation wireless systems. *IEEE Commun. Mag.*, 52(2):186–195, Feb 2014.
- [30] H. Lee, I. Sohn, D. Kim, and K. B. Lee. Generalized MMSE beamforming for downlink MIMO systems. In *IEEE Int. Conf. Communications*, pages 1–6, June 2011.
- [31] G. Lerosey, J. De Rosny, A. Tourin, A. Derode, and M. Fink. Time reversal of wideband microwaves. *Appl. Phys. Lett.*, 88(15):154101–154101–3, Apr 2006.
- [32] G. Lerosey, J. de Rosny, A. Tourin, A. Derode, G. Montaldo, and M. Fink. Time reversal of electromagnetic waves. *Phys. Rev. Lett.*, 92:193904, May 2004.
- [33] G Lerosey, J De Rosny, A Tourin, A Derode, G Montaldo, and M Fink. Time reversal of electromagnetic waves and telecommunication. *Radio Sci.*, 40(6), 2005.
- [34] Hui Liu, H. Darabi, P. Banerjee, and Jing Liu. Survey of wireless indoor positioning techniques and systems. *IEEE Trans. Syst., Man, Cybern., Part C: Applications and Reviews*, 37(6):1067–1080, Nov 2007.
- [35] Q. Liu and C. W. Chen. Joint transceiver beamforming design and power allocation for multiuser mimo systems. In *IEEE Int. Conf. Communications*, pages 3867–3871, June 2012.
- [36] H. Ma, Y. Han, Y. Chen, Z. Safar, F. Han, and K.J.R. Liu. Handshaking protocol for time-reversal system. US Patent, 9313020, April 12, 2016.
- [37] R. Muharar and J. Evans. Downlink beamforming with transmit-side channel correlation: A large system analysis. In *IEEE Int. Conf. Communications*, pages 1–5, June 2011.
- [38] I.H. Naqvi, G. El Zein, G. Lerosey, J. de Rosny, P. Besnier, A. Tourin, and M. Fink. Experimental validation of time reversal ultra wide-band communication system for high data rates. *IET Microwaves, Antennas Propag.*, 4(5):643–650, May 2010.
- [39] D.W.K. Ng and R. Schober. Energy-efficient resource allocation in OFDMA systems with large numbers of base station antennas. In *Int. Conf. Communications*, pages 5916–5920, Jun 2012.
- [40] H. Q. Ngo, E. G. Larsson, and T. L. Marzetta. Energy and spectral efficiency of very large multiuser MIMO systems. *IEEE Trans. Commun.*, 61(4):1436–1449, Apr 2013.

- [41] H. Q. Ngo, M. Matthaiou, and E. G. Larsson. Massive mimo with optimal power and training duration allocation. *IEEE Wireless Commun. Lett.*, 3(6):605–608, Dec 2014.
- [42] Hien Quoc Ngo, E.G. Larsson, and T.L. Marzetta. Massive MU-MIMO downlink TDD systems with linear precoding and downlink pilots. In *Annu. Allerton Conf. on Communication, Control, and Computing*, pages 293–298, Oct 2013.
- [43] Dragoş Niculescu and Badri Nath. VOR base stations for indoor 802.11 positioning. In *Procc 10th Annu. Int. Conf. Mobile Computing and Networking, MobiCom '04*, pages 58–69, New York, NY, USA, 2004. ACM.
- [44] Neal Patwari and Sneha K. Kasera. Robust location distinction using temporal link signatures. In *Proc. 13th Annu. ACM Int. Conf. Mobile Computing and Networking, MobiCom '07*, pages 111–122, New York, NY, USA, 2007. ACM.
- [45] C. A. Pitz, E. L. O. Batista, and R. Seara. On the joint beamforming and power control in cellular systems: Algorithm and stochastic model. *IEEE Trans. Wireless Commun.*, 13(12):6943–6954, Dec 2014.
- [46] A. Pokhariyal, K.I. Pedersen, G. Monghal, I.Z. Kovacs, C. Rosa, T.E. Kolding, and P.E. Mogensen. HARQ aware frequency domain packet scheduler with different degrees of fairness for the UTRAN long term evolution. In *Vehicular Technology Conf.*, pages 2761–2765, Apr 2007.
- [47] R.C. Qiu, Chenming Zhou, Nan Guo, and J.Q. Zhang. Time reversal with MISO for ultrawideband communications: Experimental results. *IEEE Antennas Wireless Propag. Lett.*, 5(1):269–273, Dec 2006.
- [48] Guolin Sun, Jie Chen, Wei Guo, and K.J.R. Liu. Signal processing techniques in network-aided positioning: a survey of state-of-the-art positioning designs. *IEEE Signal Process. Mag.*, 22(4):12–23, July 2005.
- [49] David Tse and Pramod Viswanath. *Fundamentals of wireless communication*. Cambridge university press, 2005.
- [50] Beibei Wang, Yongle Wu, Feng Han, Yu-Han Yang, and K.J.R Liu. Green wireless communications: A time-reversal paradigm. *IEEE J. Sel. Areas Commun.*, 29(8):1698–1710, September 2011.
- [51] X. Wang, P. Zhu, F. C. Zheng, C. Meng, and X. You. Energy-efficient resource allocation in multi-cell OFDMA systems with imperfect CSI. In *Vehicular Tech. Conf.*, pages 1–5, Sept 2015.
- [52] C. Wengertter, J. Ohlhorst, and A.G.E. von Elbwart. Fairness and throughput analysis for generalized proportional fair frequency scheduling in OFDMA. In *Vehicular Technology Conf.*, volume 3, pages 1903–1907, May 2005.

- [53] L.A. Wolsey. *Integer Programming*. Wiley Series in Discrete Mathematics and Optimization. Wiley, 1998.
- [54] Kaishun Wu, Jiang Xiao, Youwen Yi, Dihu Chen, Xiaonan Luo, and L.M. Ni. CSI-based indoor localization. *IEEE Trans. Parallel Distrib. Syst.*, 24(7):1300–1309, July 2013.
- [55] Zhung-Han Wu, Yi Han, Yan Chen, and K.J.R Liu. A time-reversal paradigm for indoor positioning system. *IEEE Veh. Technol. Mag.*, 64(4):1331–1339, Apr 2015.
- [56] Jie Xiong and Kyle Jamieson. ArrayTrack: A fine-grained indoor location system. In *Proc. 10th USENIX Symp. Networked Systems Design and Implementation*, pages 71–84, Lombard, IL, 2013. USENIX.
- [57] Q. Xu, Y. Chen, and K. Liu. Combating strong-weak focusing effect in time-reversal uplinks. *IEEE Trans. Wireless Commun.*, 15(1):568 – 580, Jan 2015.
- [58] Yu-Han Yang, Beibei Wang, W.S. Lin, and K.J.R Liu. Near-optimal waveform design for sum rate optimization in time-reversal multiuser downlink systems. *IEEE Trans. Wireless Commun.*, 12(1):346–357, January 2013.
- [59] Haifan Yin, D. Gesbert, and L. Cottatellucci. Dealing with interference in distributed large-scale MIMO systems: A statistical approach. *IEEE J. Sel. Topics Signal Process.*, 8(5):942–953, Oct 2014.
- [60] M.A. Youssef, A. Agrawala, and A. Udaya Shankar. WLAN location determination via clustering and probability distributions. In *Proc. 1st IEEE Int. Conf. Pervasive Computing and Communications*, pages 143–150, March 2003.
- [61] Moustafa Youssef and Ashok Agrawala. The Horus WLAN location determination system. In *Proc. 3rd Int. Conf. Mobile Systems, Applications, and Services, MobiSys '05*, pages 205–218, New York, NY, USA, 2005. ACM.
- [62] Moustafa Youssef, Adel Youssef, Chuck Rieger, Udaya Shankar, and Ashok Agrawala. PinPoint: An asynchronous time-based location determination system. In *Proc. 4th Int. Conf. Mobile Systems, Applications and Services, MobiSys '06*, pages 165–176, New York, NY, USA, 2006. ACM.
- [63] Boris Ia Zeldovich, Nikolai F Pilipetskii, and Vladimir V Shkunov. Principles of phase conjugation. In *Berlin and New York, Springer-Verlag (Springer Series in Optical Sciences. Volume 42), 1985, 262 p.*, volume 42, 1985.
- [64] Junxing Zhang, Mohammad H. Firooz, Neal Patwari, and Sneha K. Kasera. Advancing wireless link signatures for location distinction. In *Proc. 14th ACM Int. Conf. Mobile Computing and Networking, MobiCom '08*, pages 26–37, New York, NY, USA, 2008. ACM.

- [65] Q. Zhang, S. Jin, M. McKay, D. Morales-Jimenez, and H. Zhu. Power allocation schemes for multicell massive MIMO systems. *IEEE Trans. Wireless Commun.*, 14(11):5941–5955, Nov 2015.
- [66] Yilin Zhao. Standardization of mobile phone positioning for 3G systems. *IEEE Commun. Mag.*, 40(7):108–116, Jul 2002.